

# **Immunogenic Signaling in Human Lung and Mouse Oral Cancer Cells After X-ray and Proton Irradiation**

**Protocol Development and Optimization**

**Fevzi Sankaya**

Thesis for the Degree of  
Master of Science



**UNIVERSITETET  
I OSLO**

**Department of Physics  
Faculty of Mathematics and Natural Sciences**

**University of Oslo**

**May 2022**



# Acknowledgments

First and foremost, I want to thank my supervisor Nina Frederike Jeppesen Edin for her support, guidance and patience. Thank you for always having your door open and being so joyous. I learned a lot from you, and for this I am eternally grateful.

I would also like to thank Julia Marzioch for helping me with the calreticulin assay and showing me proper laboratory etiquette. Also thank you for seeding and preparing the cells for everyone. I want to thank Olga Zlygosteva for showing me how to perform a clonogenic assay and Joe Alexander Sandvik for helping with cell orders and assistance at the cell lab. Thanks to my fellow master students for creating a pleasant work environment and special thanks to Frida Larsen for providing me with MOC2 clonogenic assay data.

Lastly, I want to thank my mother Perihan Tekin and my older brother Ridvan Akinci for taking care of me and showing me love and support.

Oslo, May 2022

Fevzi Sankaya

# Abstract

In recent years knowledge of immunology has grown and the immune system's role in cancer has been scrutinized. Accumulating evidence suggests that radiotherapy (RT) has an effect on immunogenicity of tumors by triggering immunogenic cell death (ICD) which activates danger associated molecular patterns (DAMPs). One of these DAMPs is the translocation of a protein called calreticulin (CRT) from the endoplasmic reticulum (ER) to the cell membrane. CRT exposed to the cell surface acts as an "eat me" signal, promoting anti-tumor activity of the immune system. Many studies have shown that the level of membrane bound calreticulin is a good indicator of immunogenicity. Proton irradiation has the advantage over X-ray of a more localized energy deposition in the so-called Bragg peak, which makes it possible to avoid irradiation of risk organs. It has been hypothesized that protons are also more efficient in inducing ICD. In this thesis we have studied two types of mouse oral squamous carcinoma MOC1 and MOC2, which had not been used by the group before. The radiosensitivity of MOC1 and MOC2 in response to X-rays was first measured by clonogenic assay. MOC1 was more radiosensitive than MOC2, with  $\alpha/\beta$ - values  $6.4 \pm 0.7$  and  $3.4 \pm 0.4$ , respectively. The CRT membrane levels were then measured in response to X-ray and proton irradiation with CRT assay and flow cytometry. In addition to MOC1 and MOC2 cells, human lung A549 cancer cells, which had previously been seen to have a dose dependent increase in CRT levels after X-ray irradiation, were included for comparison. The types of ionizing radiation used were 220 kV X-rays ( $LET \sim 1.1 \text{ keV}/\mu\text{m}$ ) and 15 MeV protons in two positions along the Bragg peak, position 1 (P1,  $LET \sim 10 \text{ KeV}/\mu\text{m}$ ) and position 5 (P5,  $LET \sim 40 \text{ KeV}/\mu\text{m}$ ). The samples were irradiated with doses of 4 Gy and 8 Gy for all irradiation types. MOC1 cells had relatively high baseline levels of CRT expression but saw no change with dose or irradiation type. A549 cells had the lowest levels of CRT expression but had the greatest relative change with dose and LET with a ratio between 8 Gy irradiated and control cells of  $1.60 \pm 0.03$  for X-rays,  $6.96 \pm 0.63$  for P1 ( $P_{X,P1} < 0.05$ ) and  $3.57 \pm 0.21$  for P5 protons ( $P_{X,P5} < 0.05$ ). MOC2 cells had the highest levels of CRT expression, and these levels were enhanced especially by 8 Gy irradiation,  $1.81 \pm 0.09$  for X-rays,  $1.19 \pm 0.08$  ( $P_{X,P1} > 0.05$ ) P1 and  $2.21 \pm 0.15$  for P5 protons ( $P_{X,P5} < 0.05$ ).

# Sammendrag

De senere årene har kunnskapen om immunologi vokst og immunforsvarets rolle i kreft blitt gransket. Det har blitt vist at strålingsterapi har en effekt på tumorimmunogenisitet ved å indusere immunogen celledød (ICD) som aktiverer skade-assosierte immunsignaler. Et av disse immunsignalene er translokasjon av proteinet kalretikulin (CRT) fra endoplasmatisk retikulum (ER) til cellemembranen. CRT på celleoverflaten oppfører seg som et «spis meg»-signal og promoterer antitumor aktivitet av immunforsvaret. Mange studier har vist at CRT nivået på cellemembranen er en god indikator på immunogenisitet. Protonstråling har en fordel over røntgenstråling ved at det har bedre lokalisering av energideposisjon i en Bragg-topp, som gjør det mulig å unngå bestråling av risikoorganer. En hypotese er at protonstråling er mer effektiv på å indusere immunogen celledød (ICD). I denne oppgaven har vi studert to typer musekreftceller fra oral platepiteelkarsinom MOC1 og MOC2, som vår gruppe ikke hadde brukt før. Strålingssensitiviteten av MOC1 og MOC2 ble målt med røntgenstråling og klonogen analyse. MOC1 var mer strålingssensitiv enn MOC2 med  $\alpha/\beta$ -verdier henholdsvis  $6.4 \pm 0.7 \text{ Gy}$  og  $3.4 \pm 0.4 \text{ Gy}$ . CRT nivåene på cellemembranen ble målt etter røntgen- og protonbestråling gjennom et CRT-antistoff og flowcytometri. I tillegg til MOC1 og MOC2 inkluderte vi humane lungekreftceller A549 som har tidligere vist en doseavhengig økning av CRT nivåer i cellemembranen for sammenligning. Den ioniserende strålingen som ble brukt var 220 kV røntgen- (LET  $\sim 1.1 \text{ keV}/\mu\text{m}$ ) og 15 MeV protonstråling i to posisjoner på Bragg toppen, posisjon 1 (P1, LET  $\sim 10 \text{ KeV}/\mu\text{m}$ ) og posisjon 5 (P5, LET  $\sim 40 \text{ KeV}/\mu\text{m}$ ). Prøvene ble bestrålt med doser på 4 Gy og 8 Gy for alle strålingstyper. MOC1-celler hadde et høyt basisnivå for CRT-uttrykk, men så ingen endring etter bestråling. A549-celler hadde de laveste nivåene for CRT-uttrykk før bestråling, men hadde også den største relative endringen med dose og LET med et forhold mellom 8 Gy bestrålte og kontrollceller på  $1.60 \pm 0.03$  for røntgen-,  $6.96 \pm 0.63$  for P1 ( $P_{X,P1} < 0.05$ ) og  $3.57 \pm 0.21$  for P5 protonstråling ( $P_{X,P5} < 0.05$ ). MOC2-cellene hadde de høyeste CRT-uttryknivåene og disse nivåene økte spesielt med 8 Gy bestråling med forholdene  $1.81 \pm 0.09$  for røntgen-,  $1.19 \pm 0.08$  for P1 ( $P_{X,P1} > 0.05$ ) og  $2.21 \pm 0.15$  for P5 for protonbestråling ( $P_{X,P5} < 0.05$ ).

# Table of contents

<b>1 INTRODUCTION .....</b>	<b>1</b>
<b>2 THEORY AND BACKGROUND .....</b>	<b>3</b>
2.1 RADIATION PHYSICS .....	3
2.1.1 <i>Classification of Radiation</i> .....	3
2.1.2 <i>Charged Particle Interactions</i> .....	5
2.1.3 <i>Photon Interactions with Matter</i> .....	9
2.1.4 <i>Methods of Producing Ionizing Radiation</i> .....	15
2.2 CELL BIOLOGY .....	21
2.2.1 <i>Important Structures in Eukaryotic Cells</i> .....	21
2.2.2 <i>The Cell Cycle</i> .....	24
2.2.3 <i>Mechanisms of Cell Death</i> .....	26
2.3 RADIOBIOLOGY .....	29
2.3.1 <i>DNA Damage and Repair Mechanisms</i> .....	29
2.3.2 <i>Linear Energy Transfer (LET) and Relative Biological Effectiveness (RBE)</i> .....	32
2.3.3 <i>Cell Survival Curves</i> .....	35
2.4 IMMUNOLOGY .....	36
2.4.1 <i>Radiation Induced Abscopal effect and Immunogenic Cell Death</i> .....	37
2.4.2 <i>Calreticulin</i> .....	38
2.5 DOSIMETRY .....	38
2.5.1 <i>Ionization Chambers</i> .....	38
2.6 FLOW CYTOMETRY .....	39
<b>3 MATERIALS AND METHODS .....</b>	<b>43</b>
3.1 TUMOR-CELL LINES AND PRACTICAL CELL CULTURING TECHNIQUES .....	43
3.1.1 <i>Cell Lines</i> .....	43
3.1.2 <i>Cell Cultivation: Culture Growth Conditions, Media and Dissociation of Cells</i> .....	43
3.1.3 <i>Cell Cultivation: Seeding, Sterility and Incubation</i> .....	45
3.2 X-RAY IRRADIATION .....	47
3.2.1 <i>Preparation</i> .....	47
3.2.2 <i>Irradiation</i> .....	48
3.3 PROTON IRRADIATION .....	50
3.3.1 <i>Preparation</i> .....	50
3.3.2 <i>Proton Dosimetry</i> .....	52
3.3.3 <i>Proton Irradiation</i> .....	53
3.4 SURVIVAL CURVES .....	55
3.4.1 <i>Colony Formation Assay</i> .....	55

3.4.2 Calculation of Cell Survival.....	58
3.5 CALRETICULIN PROTOCOL DEVELOPMENT.....	61
3.5.1 Adjustments for a New Protocol Assay.....	61
3.6 CALRETICULIN (CRT) ASSAY .....	62
3.7 FLOW CYTOMETRY ANALYSIS .....	63
3.7.1 Flow Cytometry channels.....	64
3.7.2 Flow cytometry CFlow Gating.....	65
3.7.3 CFlow Data Statistical Significance and Student's T-test.....	69
<b>4 RESULTS .....</b>	<b>70</b>
4.1 COLONY SURVIVAL EXPERIMENT RESULTS.....	72
4.2 MEMBRANE BOUND CALRETICULIN AFTER CALRETICULIN ASSAY.....	75
4.2.1 X-ray Irradiation Results .....	76
4.2.2 Proton Irradiation Results.....	78
<b>5 DISCUSSION AND ANALYSIS .....</b>	<b>82</b>
5.1 MOC1 AND MOC2 SURVIVAL .....	82
5.2 CALRETICULIN EXPRESSION ON CELL MEMBRANE.....	83
5.2.1 Differences in Cell Lines .....	84
5.2.2 Comparing Our Results .....	86
5.3 Protocol Development, Future Perspectives and Suggestions .....	89
<b>6 CONCLUSION .....</b>	<b>91</b>
<b>REFERENCES.....</b>	<b>92</b>
<b>APPENDIX 1.....</b>	<b>97</b>
<b>APPENDIX 2.....</b>	<b>103</b>
<b>APPENDIX 3.....</b>	<b>105</b>
<b>APPENDIX 4.....</b>	<b>108</b>
<b>APPENDIX 5.....</b>	<b>111</b>

# Abbreviations

ADC	Analog to digital converter
APC	Antigen presenting cells
APE1	Apurinic endonuclease
ATCC	American Type Culture Collection
ATP	Adenosine triphosphate
BER	Base excision repair
BSA	Bovine serum albumin
CRT	Calreticulin
CD4	Cluster of differentiation 4
CD8	Cluster of differentiation 8
CDK	Cyclin-dependant kinase
CFA	Colony formation assay
CFU	Colony forming unit
CKI	Cyclin-dependant kinase inhibitor
CPE	Charged particle equilibrium
CS	Compton scattering
CTLA-4	Cytotoxic associated protein 4, CD152
CTL	Cytotoxic T lymphocytes
DAMP	Danger associated molecular pattern
DC	Dendritic cells
DLP	Dichroic long pass filter
DMEM	Dulbecco's Modified Eagle Medium
DNA	Deoxyribonucleic acid
DSB	Double strand break
EDTA	Ethylenediaminetetraacetic acid
ER	Endoplasmic reticulum
F-12	Ham's F-12
FBS	Fetal bovine serum
FSC	Forward scatter
HEPA	High efficiency particulate air



HNC	Head and neck
HMGB1	High-mobility group box 1
HPV	Human papilloma virus
HRR	Homologous recombination repair
IC	Ionization chamber
ICBT	Immune checkpoint blockade
ICD	Immunogenic cell death
IMDM	Iscovo's Modified Dulbecco's Media
IT	Immunotherapy
KERMA	Kinetic energy released per unit mass
LAF	Laminar air flow
LD	Lethal damage
LET	Linear energy transfer
LQ	Linear quadratic
MC	Monitor chamber
MDM2	Mouse double minute 2 homolog
MOC	Mouse oral squamous cell carcinoma
mRNA	Messenger ribonucleic acid
MU	Monitor units
NER	Nucleotide excision repair
NHEJ	Non-homologous end joining
OCL	Oslo Cyclotron Laboratory
PA	Primary antibody
PBS	Phosphate-buffered saline
PDD	Percent depth dose
PE	Photoelectric effect
PI	Propidium iodide
PLD	Potentially lethal damage
PMMA	Poly (methyl methacrylate)
PMT	Photomultiplier tube
PP	Pair production

RBE	Relative biological effectiveness
RNA	Ribonucleic acid
RS	Rayleigh scattering
ROS	Reactive oxygen species
RT	Radiotherapy
SA	Secondary antibody
SEM	Standard error of mean
SIP	Sample injection port
SLD	Sublethal damage
SSB	Single strand break
SSC	Side scatter
tRNA	Transport ribonucleic acid
UiO	University of Oslo
UV	Ultraviolet

# 1 Introduction

Cancer is one of the leading causes of death in countries of all income levels. The rates of many cancer types are being brought under control in western countries through decreasing prevalence in risk factors, early detection and improved treatment. On the other hand, lung and breast cancers are examples of cancer types on the rise, especially in low-middle income economies due to an increase in risk factors such as smoking, physical inactivity and changing reproductive patterns (Torre, 2016). Improving on the current methods of cancer treatment is an important step in reducing the burden of cancer on society and minimizing the impact on cancer patients' quality of life post treatment.

Radiotherapy (RT) is the use of ionizing radiation for palliative or curative treatment of cancer. As one of the most common cancer treatment modalities, RT has been used for local tumor control and treatment since the discovery of X-rays over a century ago. In recent years, occurrences of immune system-mediated tumor remission outside the radiation field, known as abscopal effect has been observed. This is a rare phenomenon and even rarer is the protective immunity caused by abscopal effect. Accumulating evidence suggests that radiation can induce immunogenic cell death (ICD) which triggers the release of danger associated molecules patterns (DAMPs), increasing tumor immunogenicity. Some of these DAMPs are the release of adenosine triphosphate (ATP), high mobility group box 1 (HMGB1) protein and translocation of calreticulin (CRT) to the cell surface (Ko et al., 2018).

In the past few decades there has also been remarkable advances in immunology and cancer immunotherapy (IT), such as immune checkpoints blockade therapy (ICBT). Clinical response has been achieved for several types of solid cancer including melanoma, lung and bladder cancer (van den Bulk, 2018). The efficacy of IT alone is widely dependent on cancer types and the immunocompetence of patients. Studies have shown that in some cases immunotherapy or radiotherapy administered alone has low efficiency in tumor control, but combined therapies have shown potent anti-tumor immunity (Ashrafizadeh, 2020).

Protons have an advantage over X-rays in terms of local dose deposition, as most of the dose deposition occurs in and around the so-called Bragg peak. Protons have significantly higher linear energy transfer (LET) than X-rays in the Bragg peak, meaning denser ionizations and more complicated damage. Our hypothesis is that protons are also more efficient at inducing ICD.

The majority of head and neck cancer (HNC) patients has HPV-negative carcinomas and cure rates for these patients have remained rather low at around 50 %. HNC is a strong candidate for proton therapy due to the many and close risk organs in the area to improve tumor control and reduce side effects (Blanchard, 2018). It is therefore highly relevant to explore whether HNC patients could benefit further from a combination of proton irradiation and immunotherapy. Our research group has started to investigate this in a syngeneic mouse model using two mouse oral squamous carcinoma cell lines, MOC1 and MOC2. The radiation dose response of these to cell lines have not previously been investigated in vitro.

The main objective of this thesis was to establish survival curves of these two cell lines in response to X-ray irradiation and to investigate the immunogenic signaling in form of calreticulin (CRT) translocation to the cell membrane after X-ray and proton irradiation. Our group has previously found a strong dose response in CRT membrane levels after X-rays for the human lung cancer cell line A549. These cells were therefore included and their CRT response to protons was investigated for comparison. Cells were irradiated with doses of 4 Gy and 8 Gy X-rays ( $\text{LET} \sim 1.1 \text{ KeV}/\mu\text{m}$ ) and protons in two isodose/dose-rate positions along the Bragg peak, position 1 (P1) ( $\text{LET} \sim 10 \text{ KeV}/\mu\text{m}$ ) the front of the Bragg peak and position 5 (P5) ( $\text{LET} \sim 40 \text{ KeV}/\mu\text{m}$ ) at the distal end of the Bragg peak. This way any differences in CRT expression would be a result of the difference in LET. Roughly 48 hours later, the CRT assay was performed and the calreticulin levels were measured using flow cytometry. In addition, clonogenic assays with MOC1 cells (and MOC2 cells by another master student) were performed to determine the radiosensitivity for these cells to compare with the CRT expression after irradiation.

## 2 Theory and background

### 2.1 Radiation Physics

This section is widely based on the books “Introduction to Radiological Physics and Dosimetry” (Attix, 1986) and “Radiation Physics for Physicists” (Podgoršak, 2016).

The study and use of ionizing radiation started with the discovery of X-rays by Wilhelm Röntgen in 1895, the discovery of natural radioactivity by Henri Becquerel in 1896 and of radium by Pierre Curie and Marie Curie-Sklodowska in 1898 (Podgoršak, 2016). The application of these discoveries in fields such as medicine for diagnostics, cancer treatment, industry and energy production quickly became apparent and has led to many other important discoveries. How ionizing radiation interacts with matter and biological systems varies based on the radiation type and energy. Therefore, it is important to classify radiation.

#### 2.1.1 Classification of Radiation

Radiation exists in different forms. As mentioned, our interests lie in ionizing radiation and the effects it has on biological matter such as cells. Ionizing radiation is radiation with sufficient energy to ionize. In other words, eject electrons from an atom or molecule, leaving it as a charged particle, an ion. Non-ionizing radiation lacks the quantum energy required to ionize matter. We see from Figure 1 how radiation is classified and examples of different types of ionizing radiation. We also notice the different modes of ionization, namely directly and indirectly ionizing radiation.

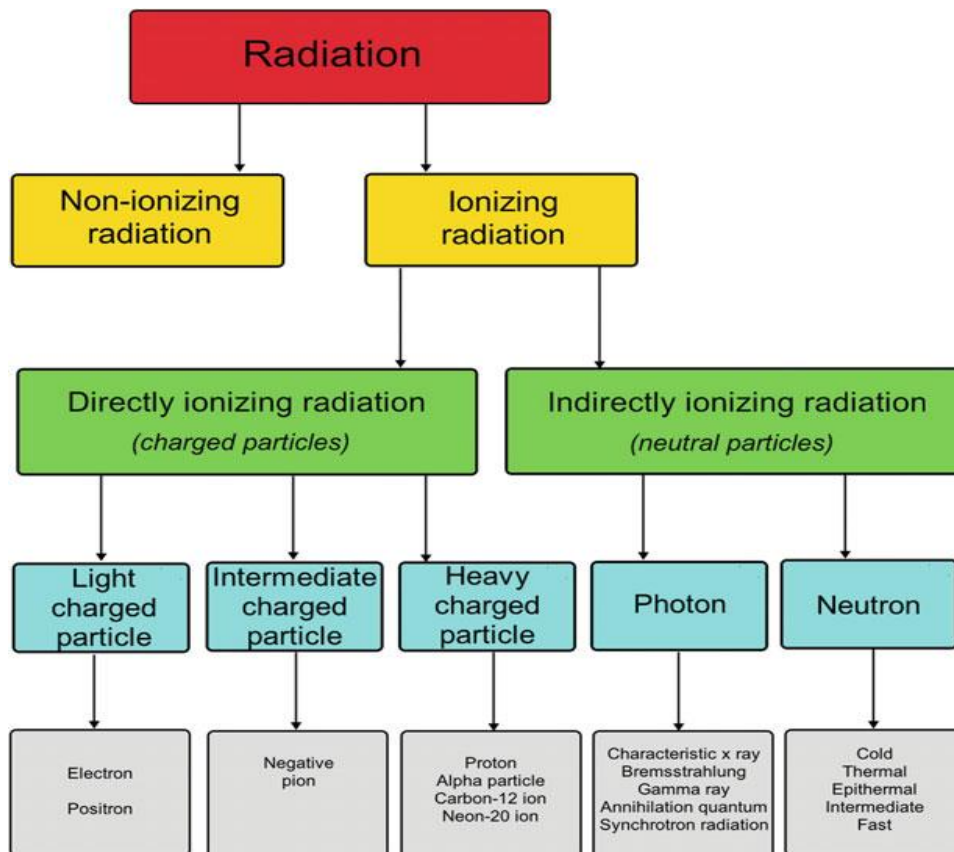


Figure 1: Classification of radiation (Podgoršak, 2016).

### Directly Ionizing Radiation

As Figure 1 indicates, charged particles such as beta particles ( $e^-$ ,  $e^+$ ), protons ( $H^+$ ) and alpha particles  $\alpha^{2+}$  ( $He^{2+}$ ) are directly ionizing. The property known as electrical charge allows these particles to interact frequently and strongly with other charged particles such as atomic electrons through the Coulomb interaction. In other words, the repulsive or attractive force caused by the particles' similar or different charge, respectively. These types of interactions can result in ionization of several atoms or molecules along the charged particle track. Consequently, this also means that charged particles are more easily stopped due to the number of interactions resulting in a rapid loss of kinetic energy as the particles traverse through matter (Attix, 1986).

### Indirectly Ionizing Radiation

On the other hand, we have neutral particles such as neutrons and photons which are indirectly ionizing. Meaning, they interact with some other particle which then leads to the liberation of directly ionizing radiation, resulting in further ionization as described for the charged particles. For example, neutrons can be absorbed by an atomic nucleus transmuting it

into a radioactive isotope. This implies that the transmuted nucleus can emit ionizing nuclear radiation such as  $\alpha$ ,  $\beta$  or  $\gamma$ -radiation. Energetic photons are also considered as neutral particles and ionize indirectly in various ways such as photoelectric effect (PE), Compton scattering (CS) and pair production (PP). These particles interact less frequently due to a lack of electrical charge and are therefore harder to stop or mediate (Attix, 1986).

### 2.1.2 Charged Particle Interactions

Charged particles interact with the Coulomb fields of orbital electrons and atomic nuclei in the matter they traverse through (Attix, 1986). This results in a transfer of energy through collisions with the surroundings atoms along their path. These collisions are characterized based on the ratio between the classical impact parameter  $b$  and the atomic radius  $a$ , Figure 2 illustrates these parameters.

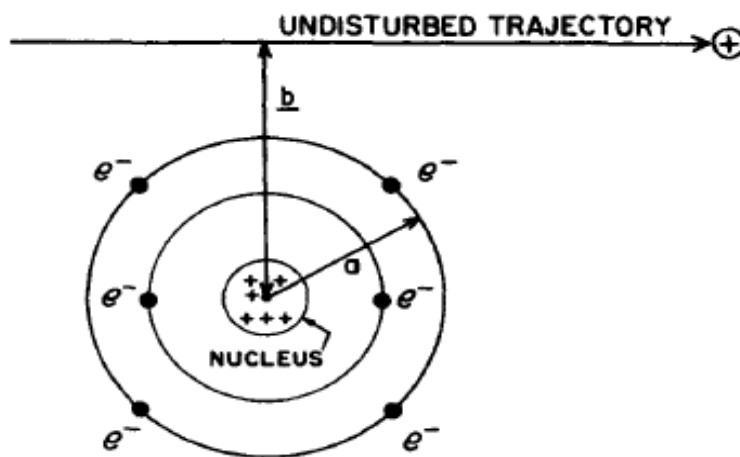


Figure 2: Illustration of the classical impact parameter,  $b$  is the shortest distance between the charged particle trajectory and the atomic nucleus. The parameter  $a$  is the atomic radius (Attix, 1986).

#### Soft collisions $b \gg a$

When a charged particle undergoes a distant collision, it interacts with the atom as a whole. This may leave the atom in an excited state, sometimes even resulting in ionization through valence electron ejection (Attix, 1986).

It is more probable that atoms along a charged particle's trajectory are distant, meaning that soft collisions happen often. The energy transferred in this way are small but numerous. These types of collisions account for roughly half of the energy transferred to the absorbing medium (Attix, 1986).

### **Hard Collisions $b \sim a$**

When charged particles are at distances roughly equal to the atomic radii, hard or “knock-on” collisions occur. This means that the charged particle interacts directly with a single atomic electron. This results in the secondary electrons being ejected and given a significant amount of kinetic energy. Electrons released in this way are called  $\delta$  (delta)-rays and have sufficient energy to ionize other atoms and molecules a significant distance away. The tracks made by these electrons are called “spurs” and can be unpredictable (Attix, 1986).  $\delta$ -rays occur when the primary beam consists of energetic charged particles such as electrons or alpha particles.

It is worth mentioning that if an inner electron is ejected it may result in the emission of Auger-electrons or characteristic X-rays, due to the processes explained below in section 2.1.3 about the photoelectric effect. This results in further emission of ionizing radiation in the form of electrons or photons.

### **Coulomb interactions with external nuclear field $b \ll a$**

When the impact parameter is much smaller than the atomic radius, we have a different type of interaction. The charged particle interacts directly with the atomic nuclei via the Coulomb force. This type of interaction is most relevant for electrons and can either result in elastic or inelastic scattering. Elastic scattering occurs in all but 2-3% of these close interactions and results in a small loss of energy to uphold conservation of momentum (Attix 1986). Although the elastic scattering does not yield in transfer of energy to the medium it is important in understanding the electron tracks, which can be difficult to predict.

The remaining 2-3 % of interactions are inelastic scatterings where the electrons are close enough to the nucleus to be deflected or decelerated. During the deflection process the electron loses energy in the form of “bremsstrahlung”, also known as braking radiation or continuous X-rays (Attix, 1986).

### **Nuclear Interactions by heavy charged particles $b \ll a$**

If a charged particle with much greater mass than an electron has sufficient kinetic energy (around 100 MeV) and the impact parameter is less than the atomic radius, an inelastic interaction with the atomic nucleus can occur. Nucleons, i.e., protons or neutrons in the nucleus are hit and ejected out of the nucleus in an intranuclear cascade process. This leaves the nucleus in an excited state which decays by particle evaporation, meaning emission of low energy nucleons or  $\gamma$ -rays. Nuclear interactions are usually ignored in radiological and



dosimetry contexts as the effect they have are negligible to the other interactions such as the production of bremsstrahlung (Attix,1986).

### Stopping power

Stopping power describes the mean energy loss of a charged particle per unit distance traveled in matter. The methods of energy loss are described above in the “charged particle interactions” section and involves energy loss due to ionization of matter through collisions ( $S_c$ , collision loss) or emission of photons ( $S_r$ , radiative loss). As mentioned, radiative loss is mainly relevant for electrons (Linz, 2012).

The Bethe-Bloch formula Eq. (1) describes stopping power  $S$  from collision loss ( $S_c$ ), assuming charged particles such as protons, alpha-particles or atomic ions.

$$S(E) = -\left\langle \frac{dT}{dx} \right\rangle = \frac{4\pi}{m_e c^2} \cdot \frac{n z^2}{\beta^2} \cdot \left( \frac{e^2}{4\pi\epsilon_0} \right)^2 \cdot \left[ \ln \left( \frac{2m_e c^2 \beta^2}{I \cdot (1-\beta^2)} \right) - \beta^2 \right] \quad \text{Eq. (1)}$$

For low particle velocities  $v \ll c$  the formula simplifies to Eq. (2)

$$S(E) = -\left\langle \frac{dT}{dx} \right\rangle = \frac{4\pi n z^2}{m_e v^2} \cdot \left( \frac{e^2}{4\pi\epsilon_0} \right)^2 \cdot \left[ \ln \left( \frac{2m_e v^2}{I} \right) \right], \quad \text{Eq. (2)}$$

where the stopping power  $S(E)$  is equal to the loss of particle kinetic energy  $T$  per unit distance  $x$  traveled in matter.  $n$  is the electron number density of the matter.  $m_e$  and  $e$  are constants for the electron rest mass and charge respectively while  $z$  is the particle charge (in multiples of  $e$ , the elementary charge).  $\epsilon_0$  is the constant for vacuum permittivity and  $I$  is the mean excitation potential.

We notice that the variable that changes for a certain particle is the velocity. The stopping power or energy loss of the particle decreases with particle velocity squared  $1/v^2$ . This implies that slow particles are easier to stop while fast particles penetrate deeper into matter. As charged particles lose their speed in matter however, the stopping power increases, slowing the particle further which again results in higher stopping power and so on until the particle is stopped completely. For relativistic cases  $\beta = \frac{v}{c} \approx 1$  we must consider that the

energy loss also increases logarithmically.

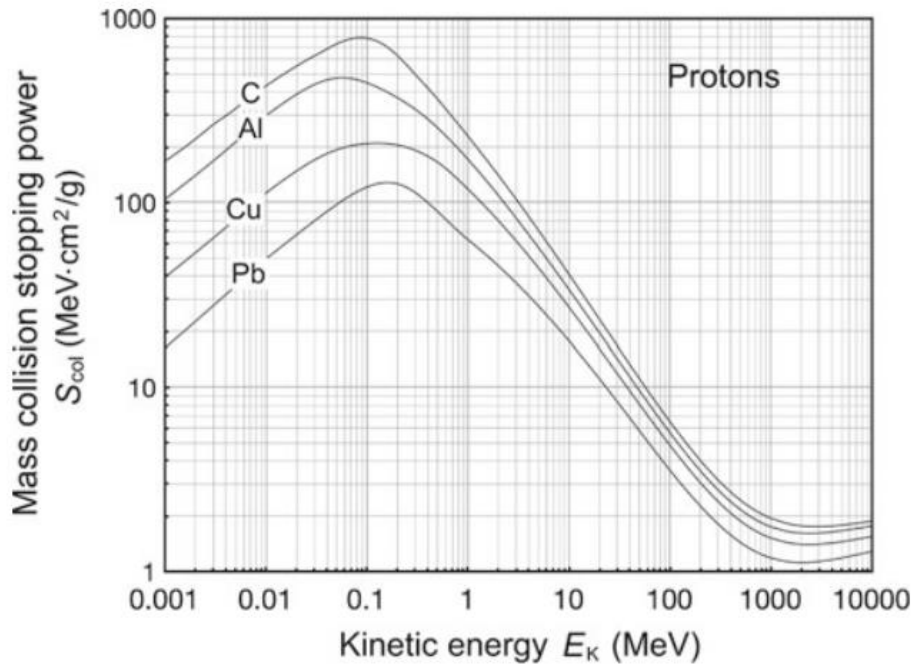


Figure 3 illustrates the mass stopping power for different materials, i.e. the stopping power divided by the matter density for a proton beam as a function of kinetic energy (Linz, 2012; Attix 1986).

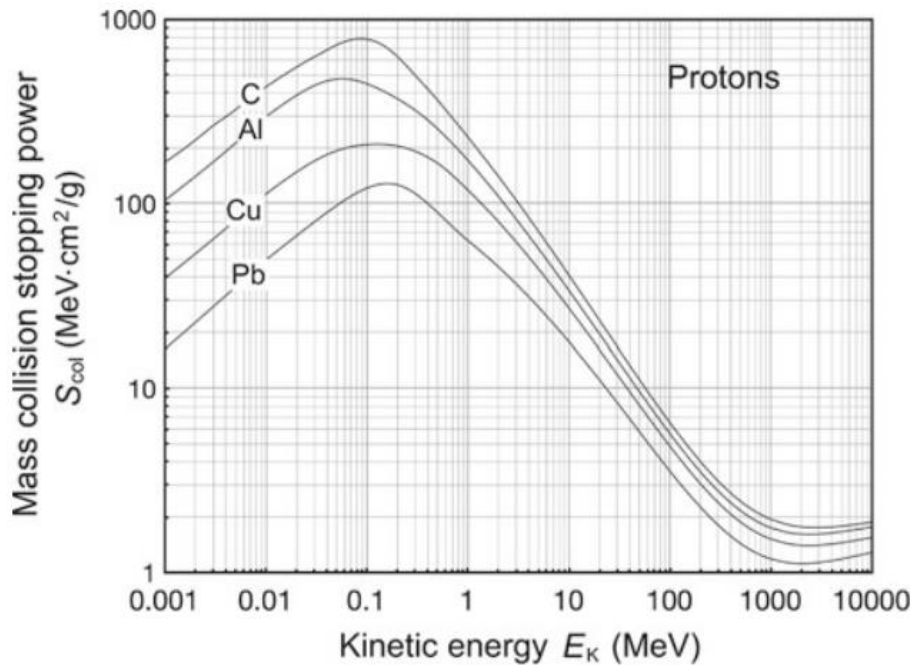


Figure 3: Mass collision stopping power of carbon (C), aluminum (Al), copper (Cu) and lead (Pb) as a function of particle kinetic energy (Podgoršak, 2016).

Protons and heavier charged particles follow a Bragg curve which can be seen in Figure 4. We also notice the Bragg peak which is the depth where we have the maximum energy deposition (dose) due to an abrupt increase in stopping power caused by the eventual loss in kinetic energy.

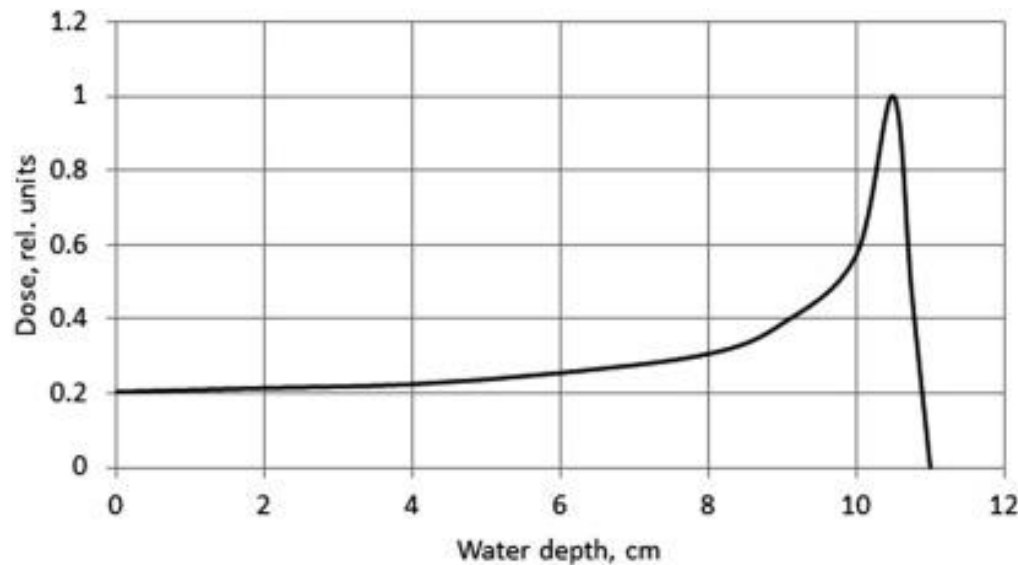


Figure 4: Dose depth curve (Bragg curve) along the range of 121 MeV protons in water (Obodovski, 2019).

Stopping power is related to another quantity called linear energy transfer (LET). We will cover more about the effects this has on cells in the radiobiology section.

### 2.1.3 Photon Interactions with Matter

Photons such as X-rays and  $\gamma$ -rays can indirectly ionize by interacting with matter mainly in three ways. These interactions are the photoelectric effect (PE), Compton scattering (CS) and pair production (PP). The cross section, or the probability for which of these interactions are more likely to occur, depend largely on the quantum energy of the photons  $E = h\nu$  and the atomic number  $Z$  of the matter the photon interacts with (Attix, 1986).

#### Photoelectric Effect (PE)

Photoelectric effect occurs when photons with sufficient quantum energy are fully absorbed by atomic electrons, resulting in electrons being ejected. Figure 5 illustrates the photoelectric effect. To be absorbed the energy of the incident photons must be higher than the binding

energy of the electrons. Any excess energy is given to the electrons as kinetic energy. This relationship is usually written as Eq. (3)

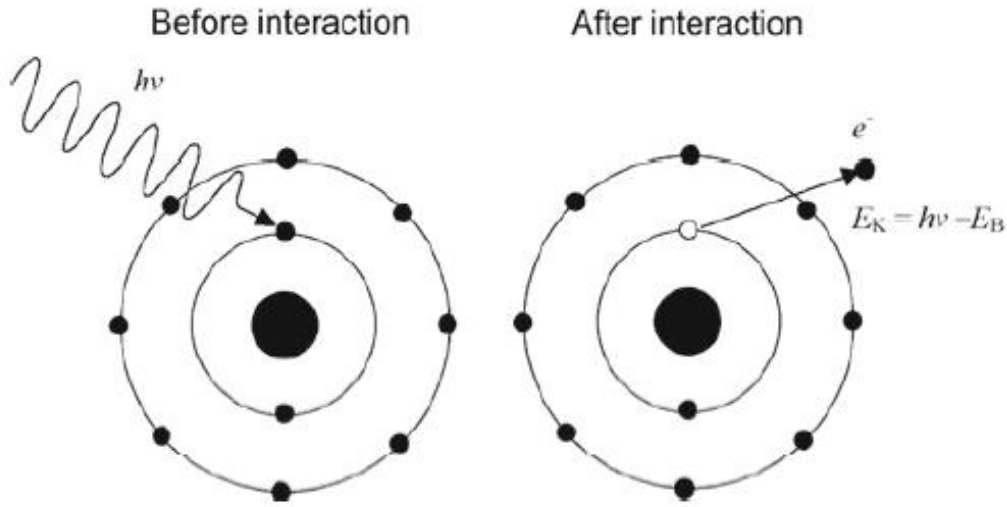


Figure 5: Diagram of the Photoelectric effect. A photon with energy  $E = h\nu$  is completely absorbed by an orbital electron, ejecting the electron with energy  $E_k$  (Podgoršak, 2016).

$$E_k = h\nu - E_B, \quad \text{Eq. (3)}$$

where  $E_k$  is the kinetic energy of the ejected electron,  $h\nu$  is the photon energy given as the product between Planck's constant  $h$  and the photon frequency  $\nu$ . The last term,  $E_B$  is the work function, the minimum amount of energy required to release the bound electron and varies based on the target atom and which energy level the electron is ejected from. The released electron travels further and can directly ionize along its track, an electron vacancy is also left in the atom in one of the energy levels. This vacancy can be filled by an electron from a higher, more energetic level and a photon is emitted in the process. The emitted photon is characteristic, meaning the photon energy depends on the energy difference between the characteristic energy levels in the atom (Attix, 1986).

Alternatively, any excess in energy can be transferred to an electron which is subsequently ejected from the atom. This is called the Auger effect and the electrons released in this manner are called Auger electrons. The Auger electron yield is unity for light elements and decreases with increasing transition energy. Meaning, the probability of Auger electrons

decreases with increasing atomic number  $Z$  as opposed to characteristic X-rays (Hofmann, 2013).

The cross section for PE  $\tau$  is highly dependent on the energy  $E = h\nu$  of the photon and the atomic number  $Z$  of the matter

$$\tau \propto \frac{Z^4}{(h\nu)^3}.$$

In other words, it is more likely for photons to interact via the PE if the photon has relatively low energy and the material is made of atoms with many protons (Attix, 1986).

### **Compton Scattering (CS)**

Compton scattering occurs when a photon gets absorbed and re-emitted by a presumably stationary and loosely bound or “free” electron. This results in a loss of energy for the incident photon. The lost energy is given to the electron as kinetic energy. The electron is scattered at an angle  $\theta$  and the outgoing photon an angle  $\phi$ . Energy and momentum are conserved, these facts can be used to derive the Compton’s equation Eq. (4).

$$\Delta\lambda = \lambda - \lambda' = \frac{h}{m_e c} (1 - \cos \theta) \quad \text{Eq. (4)}$$

Here  $\lambda'$  is the incident photon wavelength,  $\lambda$  is the outgoing photon wavelength,  $h$  is Planck’s constant,  $m_e$  is the electron mass,  $c$  is the speed of light. The atomic cross section for CS  $\sigma_A$  is less dependent on the photon energy and atomic number than the other interactions,

$$\sigma_A \propto Z.$$

The Compton interaction dominates for photon energies between 30 KeV and 30 MeV for materials with low  $Z$ . This makes it more relevant for photon interactions with soft tissue for a wide photon energy interval (Attix, 1986).

### **Pair Production (PP)**

Photons with an energy of  $E = h\nu = 1.022 \text{ MeV}$  or higher can undergo a third interaction where the photon splits into an electron-positron pair in the vicinity of an atomic nucleus. The energy requirement for this interaction to occur is the rest mass of two electrons, which is apparent when using the energy-mass equivalence, Eq. (5).

$$E_{2e} = 2m_e c^2 = 2 \cdot 0.511 \text{ MeV} = 1.022 \text{ MeV} \quad \text{Eq. (5)}$$

If the photon has more than the minimum required energy, it will be divided equally between the particle-antiparticle pair as kinetic energy. The electron and the positron are charged particles, meaning they directly ionize further along their tracks. The cross section  $\kappa$  for pair

production is proportional to the atomic number of the nuclei

$$\kappa \propto Z^2 .$$

This means that pair production is more likely to occur when the nuclei of atoms have more protons.

Another similar interaction is “triplet production” which occurs when a photon interacts with the electromagnetic field of an atomic electron, as opposed to the atomic nucleus. For this to happen the photon must have an energy equivalent to the rest mass of four electron masses  $E = 4m_e c^2 = 2.044 \text{ MeV}$  because of momentum conservation. The photon interacts with an electron to create a triplet which includes the primary electron which the photon interacts with and an electron-positron pair (Attix, 1986).

### **Other Photon Interactions**

Although we have looked at the three main ways of photon interact with matter, there are also two other interactions worth mentioning in a radiological context. One example is photonuclear interactions. As mentioned, radioactive nuclei can emit high energy  $\gamma$ -photons to achieve stability. The opposite is also true, the atomic nucleus can absorb an energetic photon and end up in an excited state. Consequently, the unstable nucleus can decay by emission of particles such as a beta-particle (electron or positron), neutrons, protons or alpha particles which can lead to ionization of atoms and molecules. Like pair production the energy conditions for photonuclear reactions to occur is in the order of a few MeV-s due to the energy levels of the nucleons in an atomic nucleus.

Lastly there is Rayleigh scattering, also known as coherent scattering. This interaction is the least relevant as the photon does not lose energy or contribute to a dose, there is only a small change in angle (Attix,1986).

### **Photon Mass Attenuation Coefficient**

Analogous to the stopping power for charged particles, photons are attenuated as they traverse through matter. Assuming a simple narrow beam geometry the photons interacting with a material will be attenuated (scattered or absorbed) exponentially with depth, meaning that the intensity  $I$  of the beam decreases from an initial intensity of  $I_0$  as shown in Eq. (6) (Attix, 1986).  $x$  is the depth in matter and  $\mu$  is the attenuation coefficient which depends on the energy of the photons and the properties of the matter such as the number of protons  $Z$ .

$$I = I_0 e^{-\mu x} \quad \text{Eq. (6)}$$

It is common to normalize the attenuation coefficient by the mass to get the mass attenuation coefficient. Neglecting photonuclear effects, the total mass attenuation is given as equation Eq. (7). We see that the mass attenuation coefficient  $\frac{\mu}{\rho}$  is the sum of contributions from the photoelectric effect (PE)  $\frac{\tau}{\rho}$ , Compton scattering (CS)  $\frac{\sigma}{\rho}$ , pair production (PP)  $\frac{\kappa}{\rho}$  and Rayleigh scattering (RS)  $\frac{\sigma_R}{\rho}$ . Typical units for photon mass attenuation coefficients are  $cm^2/g$  or  $m^2/kg$

$$\frac{\mu}{\rho} = \frac{\tau}{\rho} + \frac{\sigma}{\rho} + \frac{\kappa}{\rho} + \frac{\sigma_R}{\rho} \quad \text{Eq. (7)}$$

### Mass Energy-Transfer and Mass Absorption Coefficients

The mass energy-transfer coefficient is the product between mass attenuation coefficient and the fraction of energy transferred to charged particles by an incident photon. Similarly to Eq. (7) the total mass energy-transfer coefficient  $\frac{\mu_{tr}}{\rho}$  is sum of contributions from three main photon interactions PE  $\frac{\tau_{tr}}{\rho}$ , CS  $\frac{\sigma_{tr}}{\rho}$  and PP  $\frac{\kappa_{tr}}{\rho}$  as seen in Eq. (8). The Rayleigh scattering does not contribute as there is no energy transfer from photons to charged particles through elastic scattering (Attix, 1986).

$$\frac{\mu_{tr}}{\rho} = \frac{\tau_{tr}}{\rho} + \frac{\sigma_{tr}}{\rho} + \frac{\kappa_{tr}}{\rho} \quad \text{Eq. (8)}$$

The mass absorption coefficient is given as Eq. (9)

$$\frac{\mu_{en}}{\rho} = \frac{\mu_{tr}}{\rho} (1 - g), \quad \text{Eq. (9)}$$

where  $g$  is the average fraction of secondary-electron energy lost in radiative interactions such as bremsstrahlung or positron in flight-annihilation (Attix, 1986).

These coefficients, both the mass energy-transfer and mass absorption coefficients depend on the probability of each of the interactions (PE, CS and PP) occurring. We already discussed how these probabilities (cross sections) vary for each interaction. The energy of the incident photons and the material composition (atomic number  $Z$ ) are the two most important factors in which interactions dominates in photon attenuation. This is also illustrated in Figure 6.

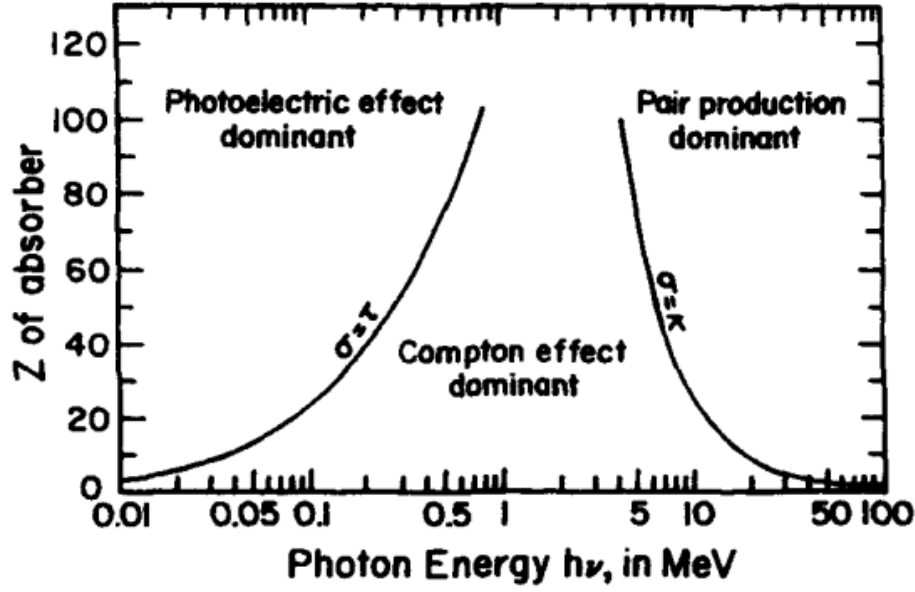


Figure 6: The importance of the three major types of photon interactions. The curves show the energy and Z values for the interaction importance (left curve PE and CS, right curve PP and CS) to be equal (Attix, 1986).

### Kerma and Absorbed Dose

kerma  $K$  is the quantity that measures the energy released by indirectly ionizing radiation in the form of liberated charged particles. Kerma is an acronym for “kinetic energy released per unit mass”, often measured in  $Gy = \frac{J}{kg}$ . In the previous section we introduced photon mass attenuation and energy-transfer coefficients, the latter being related to how much energy is given to a secondary charged particle from an incident photon.

$$K = \left( \frac{d\epsilon_{tr}}{dm} \right) \quad \text{Eq. (10)}$$

The kerma at a point of interest  $P$  in a finite volume  $V$  as we see from Eq. (10) is the energy transferred to charged particles per mass by indirectly ionizing radiation. In other words, how much energy is given to charged particles (electrons and positrons) per mass as a result of a photon or neutron interactions. One tends to separate kerma into two components known as collision kerma  $K_c$  and radiative kerma  $K_r$  as seen in Eq. (11), for the two types of electronic interactions with matter.

$$K = K_c + K_r \quad \text{Eq. (11)}$$

Collision kerma  $K_c$  is the energy lost due to Coulomb-force interactions with atomic electrons in the absorbing material. This leads to local dissipation of energy through ionization and excitations near the electron track. These are the same interactions that were described in



section 2.1.2 about charged particle interactions with impact parameter values  $b \gg a$  and  $b \sim a$ , representing soft and hard collisions, respectively.

Likewise radiative kerma  $K_r$  represent the case for  $b \ll a$  where electrons decelerate near atomic nuclei and emit bremsstrahlung X-rays. The photons created by these electrons are penetrating and can easily escape the volume of interest, ionizing indirectly further away from where they originated. (Attix,1986)

This leads us to the quantity we are most interested in, the absorbed dose  $D$ , Eq. (12).

Absorbed dose is a measure of how much ionizing energy  $\epsilon$  is imparted in matter per unit mass  $m$  for a finite volume  $V$ . If we assume charged particle equilibrium (CPE), the collision kerma is equal to the absorbed dose. In other words, if the number of charged particles entering and leaving a volume of interest is the same, the dose deposited to that volume is equal to the energy lost by particles through collision interactions (ionizations).

$$D = K_c = K(1 - g) = \left(\frac{d\epsilon_{en}}{dm}\right) \quad \text{Eq. (12)}$$

For relatively low photon energies the Kerma is approximately equal to the absorbed dose. High photon energies increase the possibility of energetic electrons and bremsstrahlung that can escape the region of interest before depositing energy meaning less local dose (Attix, 1986). This explains the percent depth dose (PDD) curves for photons in water as seen in Figure 7. We see that near the surface of the water there is a build-up region and the dose percentage is low (Kerma  $\neq$  Dose). As we liberate more charged particles CPE will be achieved at some depth, meaning the energy released will be equal to the energy absorbed by the medium. Then we must consider that the photons are attenuated exponentially explaining the decrease in dose with depth.

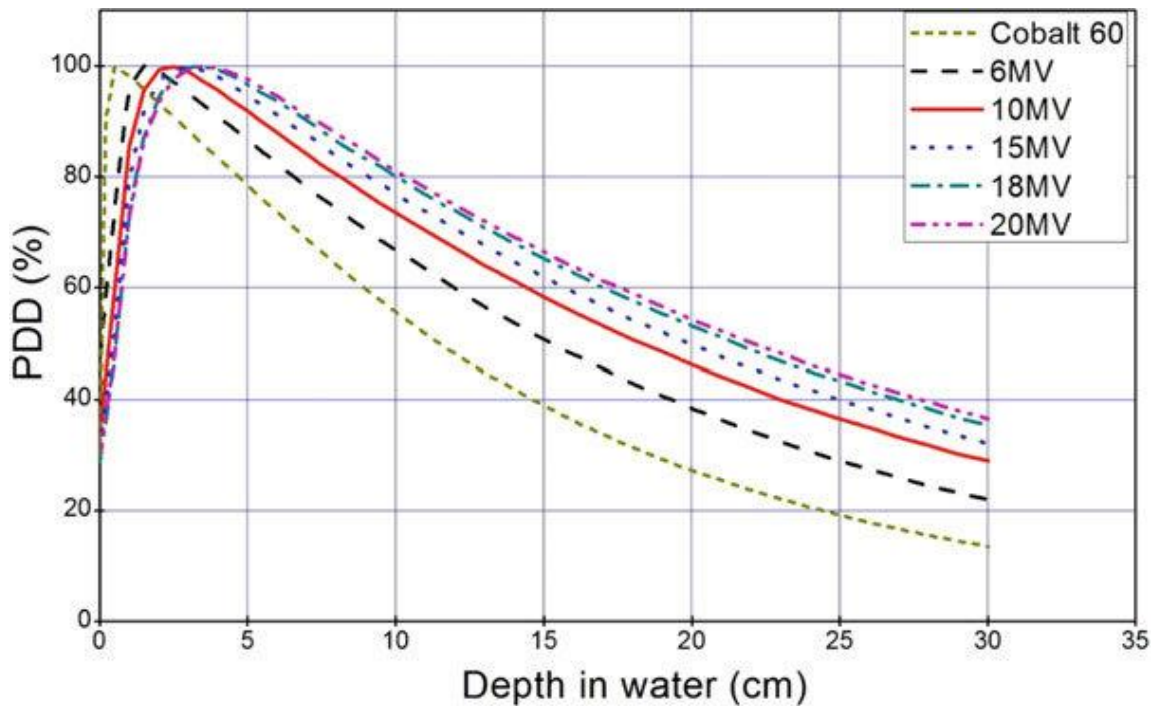


Figure 7: Percent depth dose (PDD) curves for photons with different energies in water (Hussain, 2017).

#### 2.1.4 Methods of Producing Ionizing Radiation

There are several ways of producing ionizing radiation. In our experiments we will use two methods, we will look at the X-ray tube to generate X-rays and cyclotron for accelerated protons.

##### The X-ray Tube

The X-ray tube is a vacuum tube that is used to produce X-rays. The tube consists of a high voltage difference between an anode and a cathode that accelerates electrons. The cathode is where the electrons are thermionically emitted. This is done by running a current through a tungsten filament to heat up and thermionically emit electrons. The anode is where the electrons are collected and hit a target, also usually made from tungsten. This is where the X-rays are produced (Podgoršak, 2016). See Figure 9 **Error! Reference source not found.** for a diagram of a Coolidge hot cathode X-ray tube. X-rays are the result of two phenomena,

characteristic X-rays (fluorescence) and continuous X-rays known as bremsstrahlung, see Figure.8.

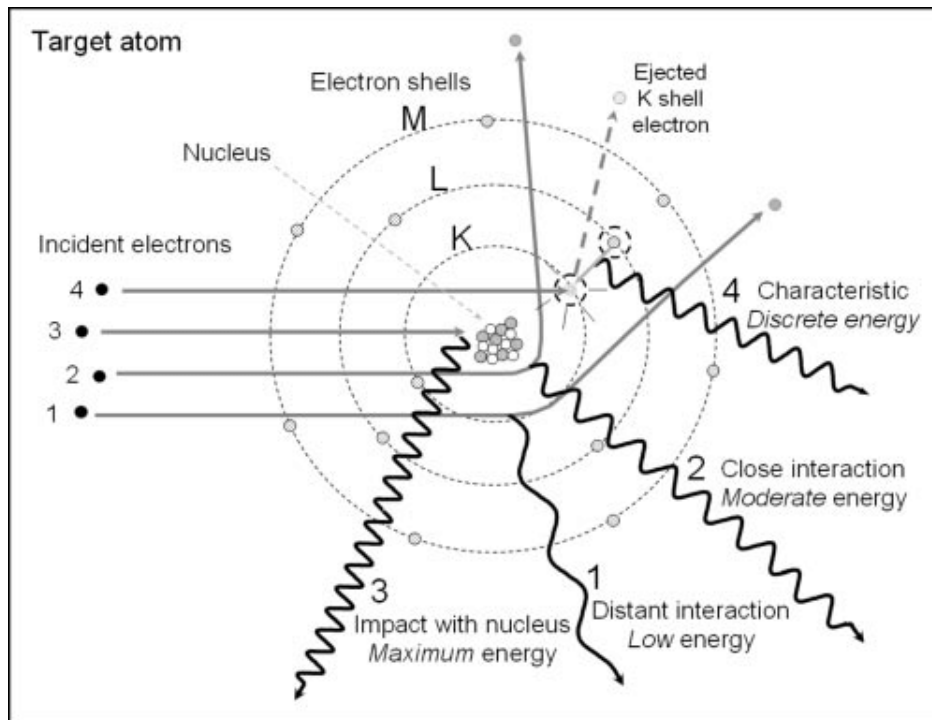


Figure.8: X-ray production by energy conversion, events 1,2 and 3 show X-rays produced by bremsstrahlung due to the electron's deceleration caused by proximity to the atomic nucleus along the electron paths. The closer the electrons get to the nucleus the stronger the deceleration yielding higher energy X-rays. Event 4 shows emission of characteristic X-rays due to direct collision with a secondary electron K-shell electron. The vacancy is filled by a higher energy L-shell electron resulting in the emission of a photon corresponding to the energy difference between the L and K-shell in the atom. (Seibert, 2004).

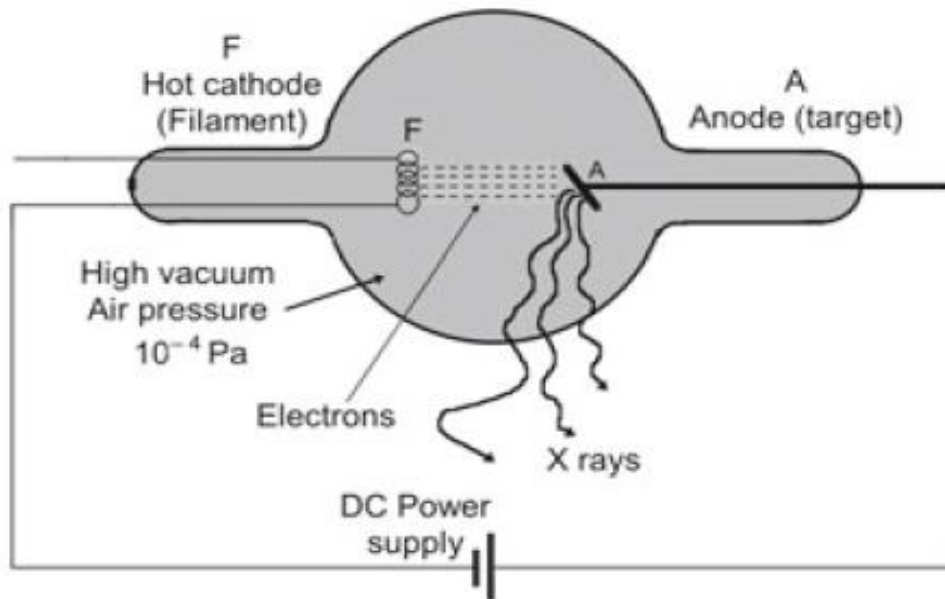


Figure 9 Schematic diagram of a Coolidge hot cathode X-ray tube (Podgoršak, 2016).

Accelerated electrons in the X-ray tube can undergo hard collisions where they eject atomic electrons in the target material, this results in characteristic X-ray emission or Auger electrons. Similarly to the photoelectric effect, this is the result of an emission of photons or electrons due to a vacancy in an electron shell that is filled by an atomic electron from a higher more energetic state. The energy difference between energy states determines the energies of the emitted characteristic X-rays or Auger electrons. We mentioned that the probability of Auger electrons decreases with atomic number  $Z$  as opposed to characteristic photons. However, which electron shell the vacancy is left in has bigger impact for the Auger/fluorescence yield. For example, tungsten with  $Z = 74$  there is a  $\sim 90\%$  chance of yielding characteristic photons when K-shell electrons are ejected. For L-shell electrons the fluorescence yield is closer to  $\sim 30\%$  (Podgoršak, 2016). The energies for characteristic photons are distinct and are seen as high peaks in the X-ray energy spectrum, see Figure 10.

Alternatively, the accelerated electrons can be decelerated or deflected by the target atomic nucleus. As mentioned, in section 2.1.2, this change in of velocity in a charged particle is accompanied by emission of bremsstrahlung resulting in continuous X-rays (Seibert, 2004).

Because of these two phenomena the X-ray energy spectrum is a continuous curve with abrupt, sharp peaks at energies that correspond to the characteristic X-rays as seen in Figure 10.

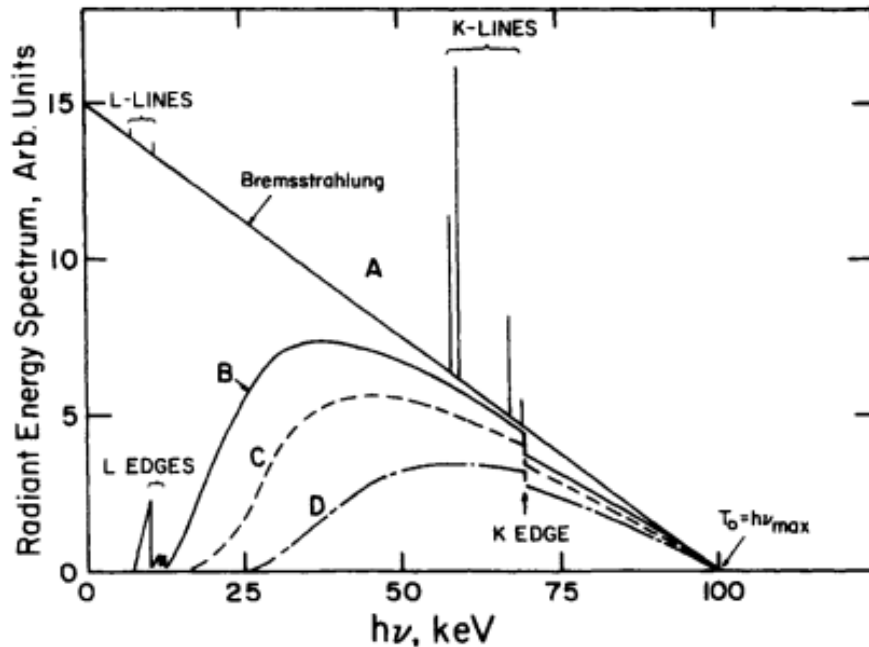


Figure 10: X-ray spectrum for 100 keV electrons on a thick tungsten target. Curve A: unfiltered. Curve B: 0.01 mm tungsten filter in escaping the target. Curve C: same as B with Additional 2 mm aluminum filter. Curve D: 0.15 mm copper, 3.9 mm aluminum in addition to inherent target filter (curve A filter) (Attix, 1986).

It is common practice when working with X-rays to denote the energy of the radiation as kV or MV instead of keV and MeV. If a voltage of 100 kV is used to accelerate the electrons only a few of them will result in the emission of 100 KeV X-rays as seen in Figure 10.

## The Cyclotron

A Cyclotron is a particle accelerator that uses electromagnetic principles to accelerate charged particles up to high energies. The machine is comprised of two main structures: the dees and the magnetic coils, see Figure 11. Most of the principles behind how a cyclotron works can be explained by classical or Newtonian mechanics. This subsection is widely based on a simplified Newtonian interpretation of the explanation found in the book “The Physics of Particle Accelerators: An Introduction” (Wille, 2001) Figure 11

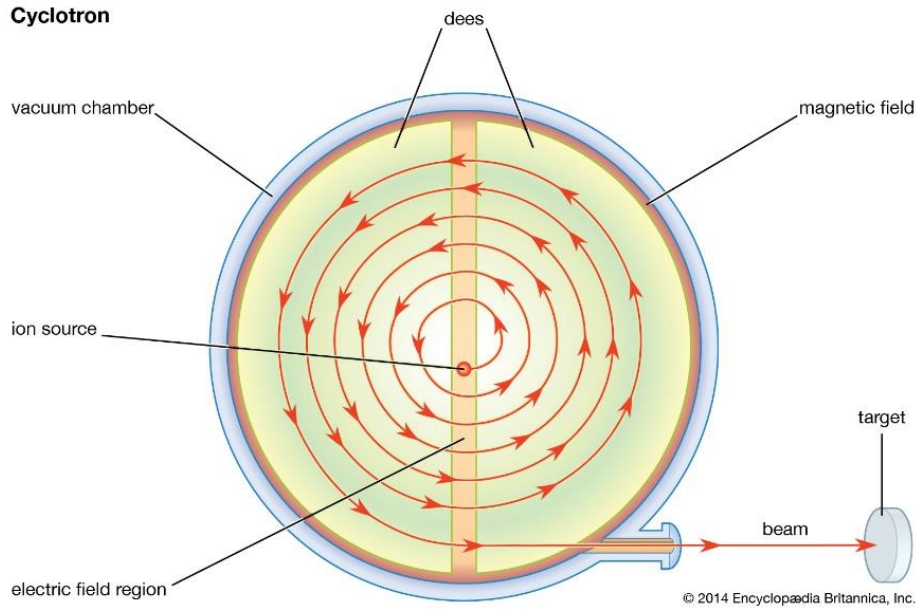


Figure 11: Diagram showing the principles of a cyclotron (Encyclopædia Britannica, 2018).

The dees are two hollow D-shaped metal electrodes with an alternating voltage across each other. These dees are placed close to each other with a gap creating an electric field between them. The electric field  $E = \frac{V}{d}$  accelerates the particles with a force  $F_e = qE = \frac{qV}{d}$ , where the strength of the force  $F_e$  is the product between the particle charge  $q$  and the electric field  $e$ . Newton's second law  $\Sigma F = ma$  tells us that the sum of all forces  $\Sigma F$  on an object is equal to the product between the mass  $m$  and the acceleration  $a$  of the object. If  $F_e$  is the only force that acts on a charged particle we an acceleration, Eq. (13).

$$a = \frac{qV}{md} \quad \text{Eq. (13)}$$

We see that the particle's acceleration  $a$  depends on the charge  $q$  and mass  $m$  of the particle, the potential difference between the dees (voltage)  $V$  and the distance between the dees  $d$ . The magnitude of this force and the corresponding acceleration is unimportant as the particles can be accelerated as many times as needed reach a desired kinetic energy. This does however give an idea of the variables and forces involved.

The magnetic coils create magnetic fields along the height of the dees. The magnetic field causes a Lorentz force perpendicular to the velocity and the magnetic field. This causes the particle to move in a circular motion where the magnetic force  $F_m$  given as Eq. (14) acts as a

centripetal force. The magnitude of this force depends on the charge  $q$  the velocity  $v$  and the magnetic flux density  $B$ .

$$F_m = qvB \quad \text{Eq. (14)}$$

Newton's second law for uniform circular motion  $\Sigma F = ma_c = m \frac{v^2}{r}$  describes motion when the acceleration is centripetal  $a = a_c = \frac{v^2}{r}$ . Here the acceleration is the velocity squared  $v^2$  divided by the radius of the circular path. Assuming  $F_m$  as the only centripetal force and the definition of angular velocity  $\omega = \frac{2\pi r}{T} = \frac{v}{r}$  we can derive the relation seen in Eq. (15).

$$\omega = \frac{qB}{m} \quad \text{Eq. (15)}$$

This relation tells us that in a cyclotron charged particles are isochronous. In other words, the angular velocity  $\omega$  is a constant because  $\frac{qB}{m}$  is a constant in a fixed, homogenous magnetic field  $B$ . Therefore, the polarity of the dees and thereby the electric field can be switched with a constant frequency (Encyclopaedia Britannica, 2018). Furthermore, we can find the maximum kinetic energy we can release the particles with by substituting the radius of the cyclotron  $R$  with the radius of the circular path  $r$  at any time as seen in Eq. (16).

$$E_{Max} = \frac{1}{2}mv^2 = \frac{q^2B^2R^2}{2m} \quad \text{Eq. (16)}$$

We see that the limiting factors for the maximum energy we can give to charged particles are the radial size of the cyclotron  $R$  and the strength of the magnetic field  $B$  for a certain particle with mass  $m$  and charge  $q$ .

Our calculations assume non-relativistic velocities, meaning that the particles are moving considerably slower than the speed of light which is not always the case. Relativistic effects means that the angular velocity  $\omega$  changes, implying a change in the frequency of the polarity switch is necessary. Cyclotrons that can synchronize the frequency to match the particle's orbital period are called synchrocyclotrons and are used to achieve relativistic charged particles velocities (Sutton, 2020).



## 2.2 Cell Biology

This section is mostly based on “Molecular Biology of The Cell” (Alberts, 2015) and “Radiobiology for the Radiologist” (Hall and Giaccia, 2019).

Cells are the fundamental building blocks and smallest units of life. Anything that is considered alive is made up of cells or is a cell. Our interests lie in eukaryotic cells. These cells have cellular nuclei where hereditary material is kept and they make up most of the macroscopic life such as plants, animals, fungi and us. To understand how radiation affects our cells we need to understand how these cells work. We will therefore look at some structures in eukaryotic cells that are relevant for radiobiology.

### 2.2.1 Important Structures in Eukaryotic Cells

Eukaryotic cells are composed of many structures such as membrane bound organelles which are important for cellular function and survival, see Figure 12. We will cover some the structures that are relevant for our research and are important in a radiobiological and a practical cell culturing context.

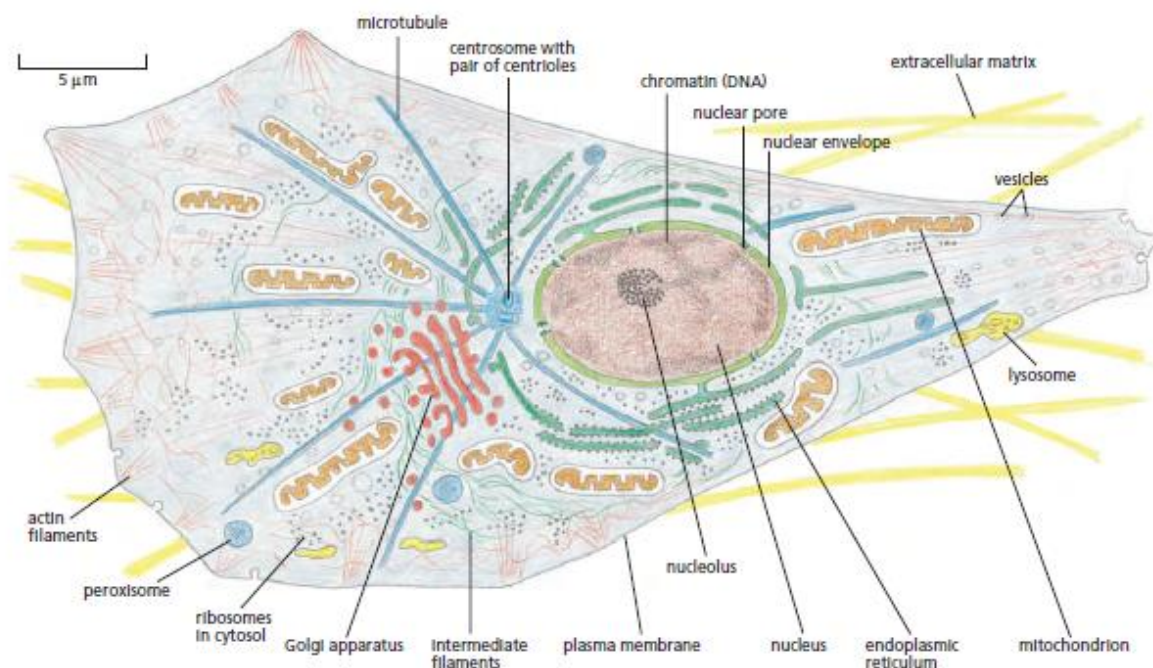


*Figure 12: The major features of the eukaryotic cell. The drawing shows an animal cell which has components that can also be found in cells of plants and fungi (Alberts, 2015).*

### The Cell Membrane

The cell membrane is the barrier separating the contents of the cell from its environment. Structurally it is built up by a phospholipid bilayer, which are amphiphilic molecules. In other



words, they consist of a polar phosphate head which is hydrophilic and two lipophilic fatty acid tails. The non-polar tails stick together while keeping the polar ends facing the liquid intracellular and extracellular space.

The cell membrane is semipermeable, meaning that smaller molecules such as water, oxygen gas and carbon dioxide may diffuse directly through the small gaps in the membrane. Larger molecules such as proteins, carbohydrates and dissolved ions cannot pass through the membrane without going through membrane bound transport proteins. This means that cells are subject to osmotic pressure, the diffusion of water through a semipermeable membrane. In addition, cells have membrane proteins called “aquaporins” (water channels) that enhance the water diffusion process considerably. These pores allow only water to flow in or out of the cell (Agre, 2006). In practice this means that, if concentration of solutes outside the cell is higher than in the cytosol (hypotonic), water will flow out and shrink the cell. The opposite is also true, if the concentration of solutes such as sugars, proteins and ions are relatively high inside the cell compared to its environment (hypertonic) water will diffuse inside the cell which can lead to the cell membrane rupturing due to the sudden increase in cytosolic volume, also known as cytolysis. Therefore, to keep cells alive during experiments they should be suspended in a liquid with similar solute concentrations as the cytosol (isotonic). Examples of liquid that maintain the tonicity of the cells are phosphate-buffered saline (PBS) or cell medium which mimics the cell’s environment inside a living animal.

Furthermore, the cell membrane contains membrane proteins which have a variety of functions. Two of these functions are as membrane receptors and the transport proteins, relaying signals from the exterior to the interior of the cell and transporting larger molecules such as ions and proteins respectively. The transportation of ions through membrane proteins allows the cell to control the tonicity of the cytosol by investing energy.

## **Mitochondria**

The mitochondrion is the cell organelle where most of the cell’s energy is produced in the form of adenosine triphosphate (ATP). The most important process that occurs in the mitochondria is oxidative phosphorylation which is how most of the ATP is produced in the cell. ATP is the energy currency of the cells and is required for many important functions such as maintaining cell tonicity. The cells can use the energy from ATP to allow movement of molecules against the concentration gradient by “active transport”. ATP is also necessary

for many other things such as DNA/RNA synthesis, cell signaling, muscle contraction and neurotransmission to name a few (Alberts, 2015).

### **Cell Nucleus and DNA**

The cell nucleus is a double membrane bound organelle containing most of the eukaryotic cell's condensed Deoxyribonucleic acid (DNA) in the form of chromosomes. DNA is the compound that carries hereditary material and is essential for the reproduction and function of the cell. Structurally DNA is built by two strands of molecule chains that wind around each other in a double helix. The strand backbone consists of alternating deoxyribose and phosphate chained together by phosphodiester bonds. Deoxyribose also forms a covalent bound with one of four nitrogenous bases known as adenine (A), cytosine (C), guanine (G) and thymine (T) (Hall and Giaccia, 2019). The two winding strands are held together by hydrogen bonds between these nitrogenous bases which are complementary to each other. A is complementary to T, likewise C and G are complementary and bind to each other. A sequence of three bases is called a "codon" which translates to a specific amino acid (Alberts, 2015).

DNA is transcribed as ribonucleic acid (RNA), a single stranded transcription of DNA where one of the nitrogenous bases, thymine (T) is replaced with uracil (U) serving the same purpose of being complementary to adenine (A). The DNA molecules can unwind with the help of an enzyme called DNA-helicase cleaving the hydrogen bonds. Since the nitrogenous bases are complementary, the enzyme RNA polymerase can synthesize RNA by using one of the DNA strands as a template, thereby creating a single stranded RNA that contains the information and codons of the DNA on a single strand. The RNA can then be transported to a ribosome for translation (Alberts, 2015).

### **Ribosomes and Endoplasmic Reticulum**

Ribosomes are the protein production sites in the cells. They can be found scattered in the cytosol or on rough endoplasmic reticulum. It is inside these macromolecular machines that mRNA translation and proteins synthesis occurs. Translation occurs with the help of transfer RNA (tRNA) which relates the codons on RNA to corresponding amino acids. By linking amino acids together with peptide bonds the primary structure of a protein is determined. Protein function also depends on how it is folded which leads us to the next structure.

The endoplasmic reticulum (ER) is a cell organelle that encloses a space called the lumen. The ER has many functions such as calcium storage, transportation and folding of proteins among others (Schwarz, 2016). There are two types of ER, smooth ER and rough ER which

as mentioned has ribosomes on the surface. Our interest in the ER also lays in a protein found inside the organelle known as “calreticulin” (CRT). Calreticulin is an ER-resident protein that acts as a calcium ion  $Ca^{2+}$  buffer and assists with correcting protein folding. CRT will be relevant later in the section about immunology.

## 2.2.2 The Cell Cycle

Proliferating cells undergo a cyclic series of events known as the cell cycle. The cell cycle can be split into two main phases namely, interphase and the mitotic phase (M-phase). As seen in Figure 13 there are four major events in the cell cycle. Non-dividing cells that are not in the cell cycle are in the G<sub>0</sub> phase where they remain either permanently or until they receive stimuli to grow and divide.

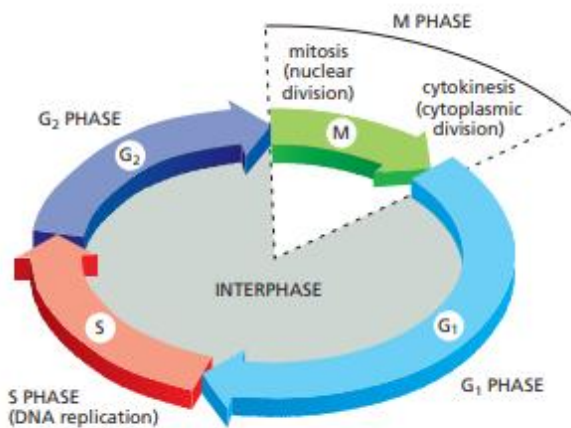


*Figure 13: The four phases of the cell cycle. The interphase encompasses most of the cycle. There is a gap phase G<sub>1</sub> and G<sub>2</sub> before the major events, DNA replication (S-phase) and mitosis followed by cytokinesis (M-phase) respectively (Alberts, 2015).*

### Interphase

Interphase is the longest phase and can be further divided into three subphases known as G<sub>1</sub>, S and G<sub>2</sub>. In the longest G<sub>1</sub> phase the cell grows, duplicates organelles, and synthesizes mRNA and proteins in preparation for S-phase. During the second longest Synthesis (S) phase the DNA in the cells are duplicated by creating two identical sister chromatids from each chromosome. The G<sub>2</sub> phase is a short gap phase after S-phase where the cell makes the final preparations for the shortest and most crucial M-phase (Cooper, 2000).

### M-phase

In M-phase cellular division occurs by segregation of the sister chromatids (mitosis) which is then followed up by cytokinesis, the creation of two daughter cells with their own nuclei. There are five subphases in M-phase as seen from Figure 14, chronologically these are known

as prophase, prometaphase, metaphase, anaphase and telophase. These phases are defined based on chromosome behavior as seen from a microscope.

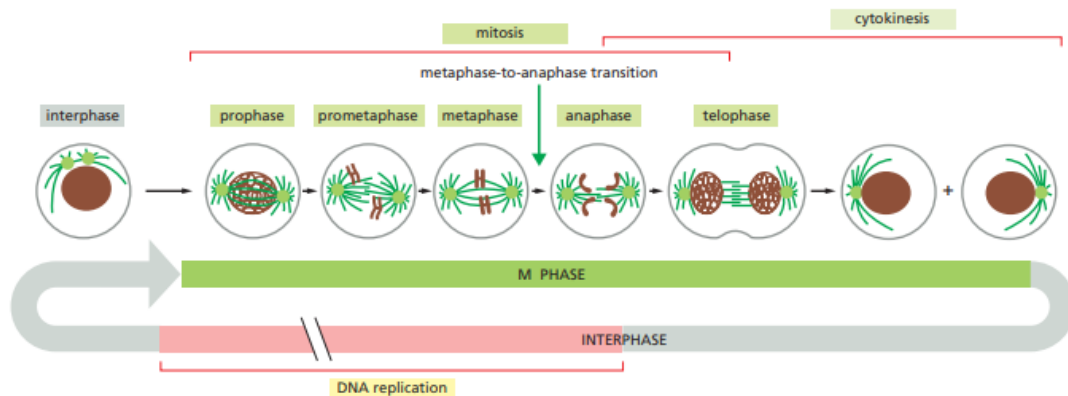


*Figure 14 The events of eukaryotic cell division as seen under a microscope. We also see an overview of the different stages of the M-phase (Alberts, 2015).*

### Cell Cycle Regulation and checkpoints

The cell cycle is driven by proteins called cyclins and a family of protein kinases called cyclin-dependent kinases (CDKs). As the names indicate, the concentration of cyclin in cells varies in a cyclic fashion as they are produced and degraded to varying degrees during the cell cycle. The CDKs depend on cyclins to be active in the form of CDK-cyclin-complex, which then acts as a protein kinase that phosphorylate (add phosphoryl group to) other molecules. When the concentration of a cyclin and its corresponding CDK-complex is sufficient at a certain stage of the cell cycle the cell progresses into the next phase. This occurs because of phosphorylation of molecules that play a major role in events that are necessary for regulation and initiation of cellular growth and division. Figure 15 shows different checkpoints in the cell cycle and what conditions need to be met in order to progress to the next phase (Alberts, 2015).

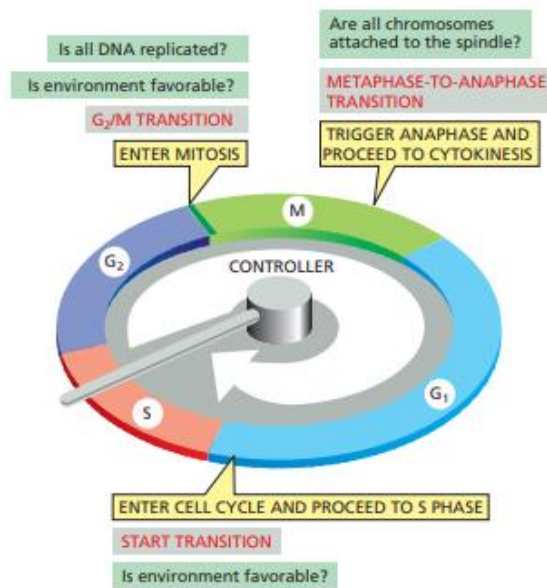


Figure 15: Checkpoints between the different phases of the cell cycle (Alberts, 2015).

On the other hand, there are proteins that regulate and delay the cell cycle. For instance, p27 is a CDK-inhibitor (CKI) which attaches to an active CDK-cyclin-complex, inactivating it and inhibiting any phosphorylation. Therefore, p27 acts as a tumor suppressor as it halts the progression of the cell cycle, usually between the G<sub>1</sub> and S phase. This delay in the cell cycle can be used to repair DNA damage before S-phase to avoid replicating damaged DNA.

Another protein that is important in cell cycle regulation is p53. p53 is also a tumor suppressor that limits the progression of the cell cycle. The concentration of p53 is stable, as it is produced continuously and then marked for degradation by the protein MDM2. If DNA damage occurs or stress signals are induced in the cell by other factors such as hypoxia or low pH values, MDM2 is phosphorylated and inactivated (Alberts, 2015). This results in an increase in active p53 concentration which acts as a brake in the cell cycle. If the damage is irreparable and p53 levels are high, p53 can induce a type of programmed cell death known as apoptosis.

### 2.2.3 Mechanisms of Cell Death

How and when cells die is an important part of maintaining multicellular organism. As opposed to ceasing to exist, cell death in a radiobiological context means that the cell stops proliferating.

## **Cellular Apoptosis and Necrosis**

We have already mentioned one type of programmed cell death or apoptosis. This is a form of cell suicide which is initiated for potentially harmful or abnormal cells or when there are more cells than necessary for a tissue to maintain size and function. For instance, during embryogenesis apoptosis is crucial for the development of fingers and toes as cells between our digits undergo apoptosis to sculpt hands and feet (Alberts, 2015). Apoptotic death is characterized by a sequence of morphological events (Hall and Giaccia, 2019). The cell ceases communication and detaches from its neighbors, the chromatin and nuclear membrane condenses, and the cell shrinks. Eventually, the cell separates into several membrane bound fragments called apoptotic bodies. Apoptosis is an advantageous mechanism for getting rid of cells as the remains are marked for phagocytosis. In other words, the apoptotic bodies are engulfed (eaten) by other cells known as phagocytes. there is no leakage of stress signals from the apoptotic bodies and therefore no inflammation response or damage to neighboring healthy cells.

On the other hand, cell necrosis is type of cell death caused by an abrupt change such as acute trauma or inadequate blood supply. The cells bursts spilling its contents to neighboring cells and causing an inflammatory response. An example of necrosis is cytolysis. If the cell lacks nutrients and energy due to insufficient blood supply, it will struggle with maintaining its tonicity. This can lead to excess water diffusion and cell membrane rupture, the cell bursts and spills its contents, including inflammatory signals. Figure 16 shows apoptosis and necrosis as seen from electron micrographs (Alberts, 2015).

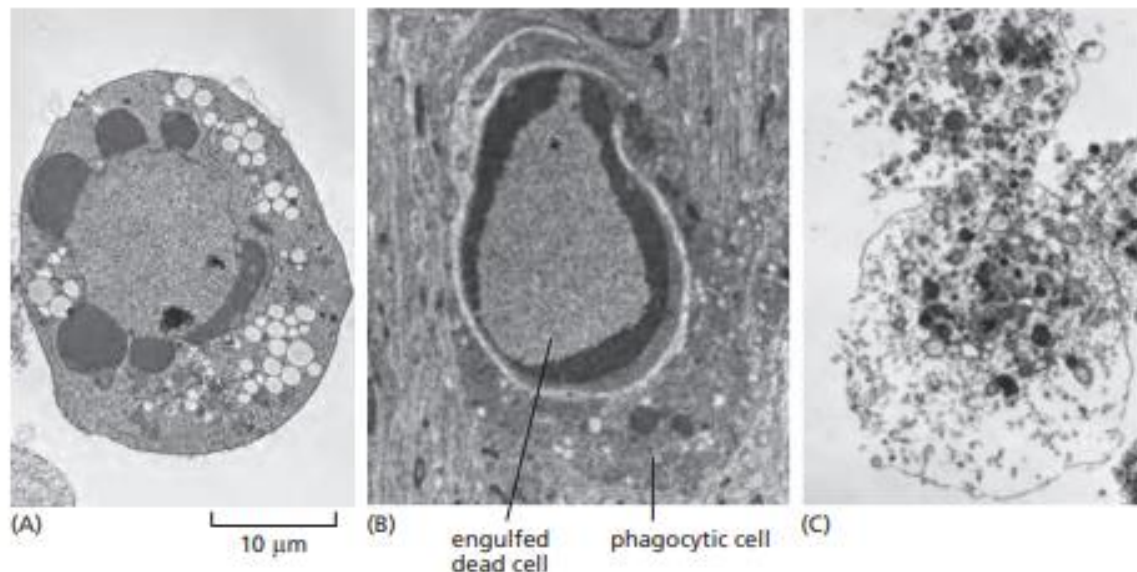


*Figure 16: Two forms of cell death shown in electron micrographs. A and B show cells that have died through apoptosis and C shows cell death through necrosis. A and C are cells grown in a cell dish while B is a cell that died in developing tissue and has been engulfed by a macrophage. We see the spillage that occurs through necrotic death C as opposed to the confined and intact membranes that are left through apoptosis A and B (Alberts. 2015).*

## Mitotic Cell Death

Mitotic cell death is the most common type of cell death caused by radiation. This type of cell death occurs during mitosis when the cells attempt to divide with damaged chromosomes. There is a clear linear relationship between mitotic cell death and chromosome aberrations (Hall and Giaccia, 2019). These are irreparable and irreversible changes in the chromosome structure and/or quantity caused by DNA damage. We will look more into chromosome aberrations in the radiobiology sections.

## Senescence

Cellular senescence is a type of stress response that causes irreversible cell cycle arrest. It is characterized by the activation of p53 and retinoblastoma (Rb). Changes in the chromatin result in silencing of the genes that promote transition from G1 into S phase. Senescent cells are metabolically active and may even secrete growth factors and mitogens but are reproductively inhibited. This means that senescent cells may promote tumor growth even if they are unable to divide (Hall and Giaccia, 2019).

## 2.3 Radiobiology

There is little doubt that the most important effect ionizing radiation has on living cells is the damage caused to the DNA. There is an overwhelming amount of evidence that points at DNA as the radiosensitive molecule, and thereby the target of ionizing radiation (Hall and Giaccia, 2019).

### **Direct and Indirect Action of radiation**

DNA damage is caused by either direct or indirect action of ionizing radiation. As the name suggests, direct action occurs when radiation interacts with the DNA molecule directly. This is typical for high LET (linear energy transfer) radiation, such as charged particles. On the other hand, we have indirect action which is more likely for low LET radiation. Indirect action occurs when radiation interacts with molecules surrounding the DNA, typically water molecules. Just like our bodies, our cells are mostly composed of water. Ionizing radiation affects the water molecules in the proximity of the cell nucleus and DNA by making destructive water radicals. These are highly reactive molecules due to an unpaired orbital electron in the outer electron shell. An example of a water radical is the hydroxyl radical

- *OH*. These radicals effectively transfer damage by stealing electrons from DNA or other biomolecules (Hall and Giaccia, 2019).

### 2.3.1 DNA Damage and Repair Mechanisms

The DNA in our cells is continuously damaged by a variety of sources, including radiation. It is crucial for cell survival and function that these damages are repaired accurately and quickly.

For instance, one or both sugar-phosphate backbones can break resulting in a single-strand break (SSB) or double-strand break (DSB) respectively, see Figure 17. The nucleobases can also be damaged or fall off. An example is depurination, which occurs when the glycosidic bond between adenine or guanine and ribose is cleaved by water molecules (hydrolysis).

Pyrimidine dimers can form which are molecular lesions caused by ultraviolet (UV) radiation. These result in the formation of covalent bonds between thymine and cytosine along a single strand of the DNA. Lack of repair enzymes and damaged DNA is the cause of many diseases including cancer (Chatterjee, 2017).



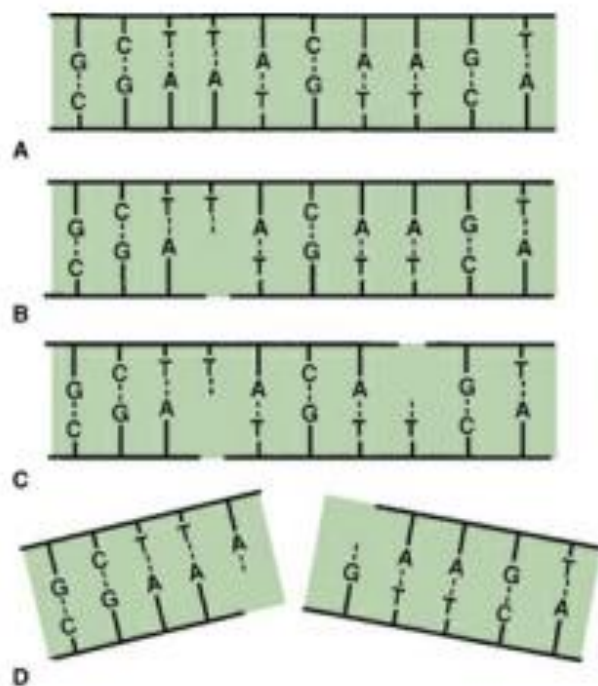


Figure 17: Diagram of single and double-strand breaks. A: Normal DNA helix in 2D. B: A single-strand break, easily repaired by using opposite strand as template. C: Two single-strand breaks that are separated, repaired independently as in case B. D: One break in both strands opposing each other or close in proximity. This leads to a double-strand break as the DNA snaps in two and no template is left to follow (Hal and Giaccia, 2019).

DNA damage is classified by lethality. We often separate between sublethal (SLD), potentially lethal (PLD) and lethal damage (LD) to the DNA. Sublethal damage as the name suggests is not lethal and is easily repaired. An example of SLD is a single-strand break or the loss of a nucleobase. If SLD is left unrepaired it can lead to potentially lethal damage. For instance, one SSB on each strand close in time and space can lead to a DSB as seen in case D in Figure 17. PLD such as double-strand breaks can still be repaired post irradiation. Left unrepaired however PLD can lead to lethal damage. At this point the damage is irreparable and irreversible and leads to cell death. This could be DNA damage such as chromosome aberrations, which are structural or numerical abnormalities in the chromosomes (Hall and Giaccia, 2019).

A dose of radiation that induces an average of one lethal event per cell is called the  $D_0$ . For mammalian cells irradiation by X-rays this dose is between 1 and 2 Gy and corresponds to approximately: 40 DSBs, 1000 SSBs, > 2000 Base damages (Hall and Giaccia, 2019).

## **DNA Repair**

There are different mechanisms for repairing DNA and they vary based on the damage.

Healthy cells are more proficient at repair DNA damage than cancer cells, something that can be utilized in radiotherapy.

### **Single-strand break and Base damage Repair**

Damage to a nucleobase is repaired through base excision repair (BER). The damaged base is removed by glycosylase or DNA lyase followed by the removal of sugar residue by apurinic endonuclease (APE1). The removed damaged parts are then replaced with the correct nucleotide using the opposing strand as a template with DNA polymerase and joined to the DNA strand by DNA ligase (Hall and Giaccia, 2019).

Bulkier DNA Damage that occurs along a single strand is fixed by a repair mechanism known as nucleotide excision repair (NER). A patch of nucleotides is removed and again, resynthesized using the other undamaged strand as a template (Alberts, 2015).

### **Double-strand Break Repair Pathways**

DNA double-strand breaks are more complicated to repair. Most DSBs have two incompatible ends because of chemical modifications or mismatching overhangs (Chang, 2017). There are two repair pathways known as non-homologous end joining (NHEJ) and homologous recombination repair (HRR).

As the name suggests, the result of NHEJ is that the two broken ends are joined together. More specifically, during NHEJ a double-strand break is repaired by removing the damaged parts and ligating the separated ends together without a template. This makes NHEJ a flexible repair pathway for repairing any kind of double strand break. However, this repair mechanism is error prone as information is lost due to the removal of parts of the DNA. This can lead to mutations and deletion of important genes (Chang, 2017).

HRR on the other hand is an accurate repair mechanism where a double-strand break is repaired by using a sister chromatid as a template for the damaged regions. Figure 18 visualizes the differences between NHEJ and HRR. Since HRR is only possible in late S-phase and early G2-phase when there is an undamaged homologous chromatid available, cells in the cell cycle become increasingly radioresistant during the S phase. However, late G2 and M-phase are especially radiosensitive as there is little to no time allowed for repair before mitosis occurs even with HRR (Hall and Giaccia, 2019).

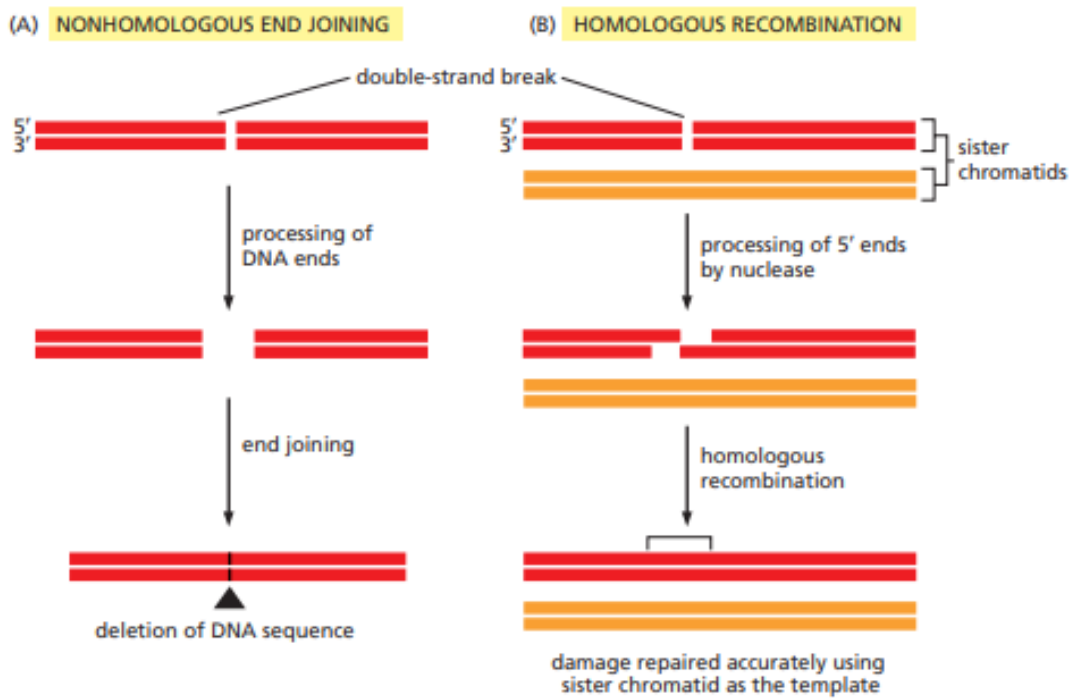


Figure 18: The two ways of repairing DSB in DNA. A: Non-homologous end joining processes both ends and ligates the remaining strands leading to deletion of some DNA sequence. B: Homologous recombination restores the original DNA sequence by using an undamaged sister chromatid as a template for the damaged parts (Alberts, 2015).

### 2.3.2 Linear Energy Transfer (LET) and Relative Biological Effectiveness (RBE)

Linear energy transfer (LET) is a measure of the energy imparted in a medium by ionizing radiation per unit length. As mentioned, LET is related to stopping power. The stopping power is the energy lost by the particle traversing matter, meanwhile LET is the energy absorbed by the matter per unit distance traveled, which is equivalent to the collision stopping power. (Mayles, 2007) In other words, LET is a measure of the ionization density or quality of a radiation beam, typical units are  $KeV/\mu m$  (Podgoršak, 2016). One tends to differentiate between low LET (sparsely ionizing, lower than  $10 KeV/\mu m$ ) and high LET (densely ionizing, higher than  $KeV/\mu m$ ) radiation. See Figure 19 for a table showing LET values for different types of radiation and energies.

Low LET radiation	LET (keV/μm)	High LET	LET (keV/μm)
x-rays: 250 kVp	2	Electrons: 1 keV	12.3
γ-rays: Co-60	0.3	Neutrons: 14 MeV	12
x-rays: 3 MeV	0.3	Protons: 2 MeV	17
Electrons: 10 keV	2.3	Carbon ions: 100 MeV	160
Electrons: 1 MeV	0.25	Heavy ions	100–2000

Figure 19: Table of LET values for different types of ionizing radiation (Podgoršak, 2016).

Since LET is a measure of beam quality it can be useful for determining the biological effect of a radiation beam. Radiation with higher LET ionizes more densely resulting in more DNA damage along a shorter distance; in other words, DNA damage that is more difficult to repair such as double-strand breaks. We can use relative biological effectiveness (RBE) to determine the damage done to tissue relative to a given dose of a given radiation quality. RBE is given as Eq. (17) and is the ratio of the dose required to reach the same biological effect between two types of radiation. An example would be the ratio of doses required to kill a certain fraction of a cell population with two different types of radiation (Mayles, 2017).

$$RBE = \frac{\text{Dose from Reference radiation}}{\text{Dose from radiation}} \quad \text{Eq. (17)}$$

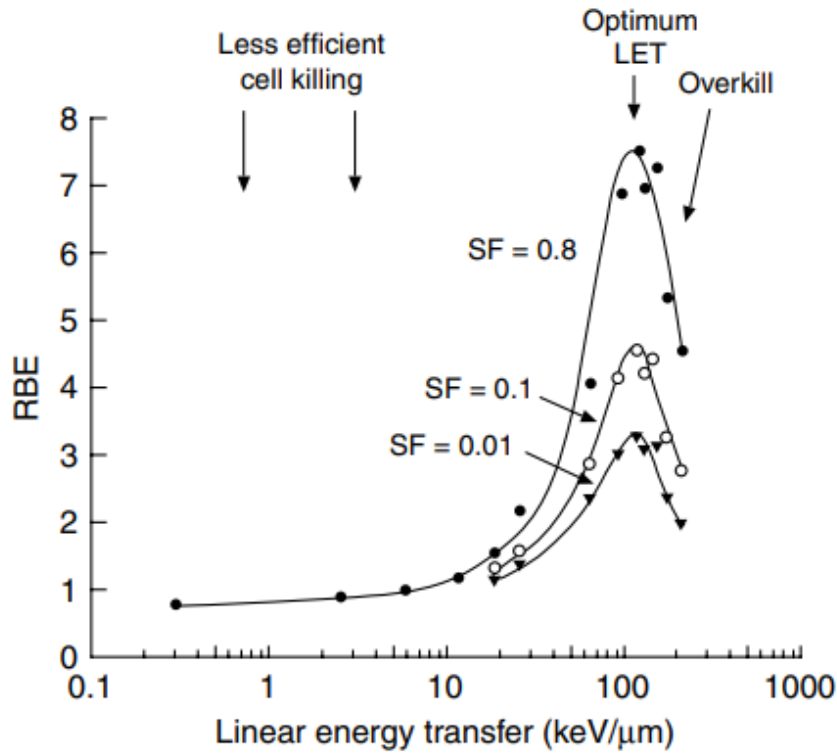


Figure 20: The relationship between RBE for cell killing and mean LET. The three curves show different levels of cell survival (survival fraction, SF). We see that low-LET radiation  $\sim 1$  to  $10 \text{ KeV}/\mu\text{m}$  has practically no effect on RBE for cell killing. High LET  $> 10 \text{ KeV}/\mu\text{m}$  increases the RBE up to a maximum at around  $100 \text{ KeV}/\mu\text{m}$  (Mayles, 2007).

In Eq. (17) we assume that the reference radiation is  $250 \text{ kV}$  X-rays considered as low LET around  $2 \text{ KeV}/\mu\text{m}$ . If the radiation we are investigating has higher LET, the RBE also increases up to a maximum of around  $100 \text{ KeV}/\mu\text{m}$ . At this point the ionization density corresponds to roughly an ionization every  $2 \text{ nm}$ , the diameter of the DNA double helix. This results in an optimal LET for double-strand breaks which are more difficult to repair and are potentially lethal to the cell. This is illustrated in Figure 20. We also notice that increasing the LET further reduces the RBE as this results in an “overkill”. In other words, we are wasting energy by using more than what is required to cause lethal DNA damage as we have more than one ionization per  $2 \text{ nm}$ .

### 2.3.3 Cell Survival Curves

A cell survival curve depicts the relationship between the fraction of cells that retain their reproductivity (surviving fraction) and a given dose.

The linear quadratic (LQ) model is often used to describe a survival curve. As the name suggests, the LQ model splits survival into a linear and a quadratic part as seen in the exponent of Eq. (18). Conventionally the survival curve is plotted in a logarithmic scale. As such, the linear part  $\alpha D$  scales linearly with dose  $D$  and represents cells killed by a single hit such as double strand breaks.  $\alpha$  is the linear coefficient and determines the importance of single hit kills. The quadratic part  $\beta D^2$  explains the bend or “shoulder region” in a survival curve and scales quadratically with dose. This part represents the multiple hits, i.e., such as the accumulation of single strand breaks that leads to cell death and is scaled by  $\beta$ . We remember that a dose of 1 to 2 Gy represents 1000 SSBs and only 40 DSBs. Higher dose represents many more SSBs that are close in time and proximity to the point where they lead to DSBs and cell death. This explains the quadratic nature of the  $\beta$  (SSB)-term (McMahon, 2019).

$$S(D) = e^{-\alpha D - \beta D^2} \quad \text{Eq. (18)}$$

The curvature of a survival curve is attributed to the ratio between the  $\alpha$  and  $\beta$  gives information about whether the cells are early or late responding to irradiation.  $\alpha/\beta$  has units of Gy and corresponds to the dose where the linear  $\alpha$  and quadratic  $\beta$  contributions are equal. Figure 21 illustrates these concepts of the LQ model. An  $\alpha/\beta$  ratio between 1.5 Gy and 5 Gy indicates late responding tissue, while ratios higher than this indicate early responding tissue (Fowler, 1984 ;Williams et al., 1985). Typically, cancer cells are early responding, i.e.  $\alpha/\beta > 5$ .

If a total dose is given at separate times (fractionated) the cell deaths related to the quadratic term  $\beta D^2$  has time to repair and there will be a reappearance of the “shoulder” in the survival curve. This favors late responding tissue as it increases their tolerance to radiation and is one of the principles behind why radiotherapy in a clinical setting is given in fractions.

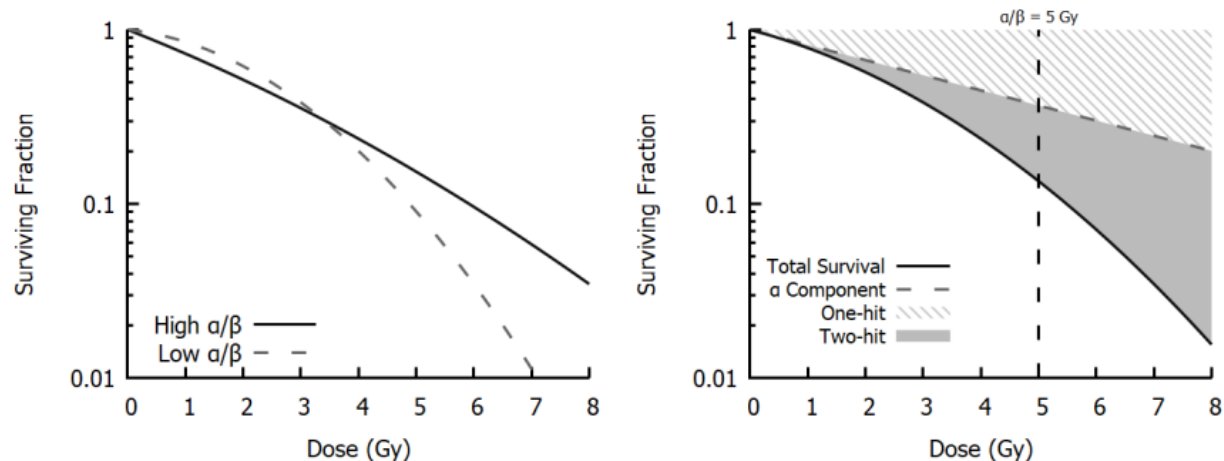


Figure 21: Illustrations of LQ survival curves. On the left we see two curves showing the dose response of two different cell lines. The dashed curve shows a survival curve with low  $\alpha/\beta$  (3 Gy) and the other straighter curve shows a curve with high  $\alpha/\beta$  (10 Gy). On the right we see the  $\alpha$  and  $\beta$  contributions. One hit ( $\alpha$ ) events dominate at low doses, as the dose increases multi hit ( $\beta$ ) events become more important. When the contributions are equal the dose is given as  $\alpha/\beta = 5 \text{ Gy}$  (McMahon, 2019).

## 2.4 Immunology

The immune system is our body's defense mechanism against microscopic threats. Under normal circumstances the immune system can make a distinction between the organism's own healthy tissue and pathogens or other disease-causing agents, including cancer.

The immune system consists of specialized cells such as dendritic cells (DCs), macrophages, T and B cells. DCs act as sentries and play a primary role in capturing and presenting antigens, molecules that can elicit an immune response. Macrophages are large phagocytes, meaning cells that engulf and remove pathogens and damaged or dead cells. T and B-cells respond to antigens such as those presented by DCs. When presented with an antigen, B-cells differentiate into memory cells which remember the antigen and plasma cells which secrete antibodies for the antigen. T-cells can be divided into T helper cells and T cytotoxic cells which are distinguished by the presence of  $\text{CD4}^+$  and  $\text{CD8}^+$  membrane glycoproteins on their surfaces respectively (Punt et al., 2019).

### Immunotherapy

The concept that the immune system can recognize and control tumor growth dates to 1893 when William Coley used bacteria as an immune stimulant to treat cancer. These first attempts at "immunotherapy" (IT) were not applied much due to their limited clinical efficacy caused by cancer cells' ability to evade the immune system. However, in the past few decades

our understanding of how cancer escapes or cooperates with the immune system through a phenomenon called immunoediting has grown (Yang et al., 2015).

One form of immunotherapy is called immune checkpoint blockade therapy (ICBT). ICBT involves using antibodies to block proteins such as CTLA-4 which functions as immune checkpoints, downregulating immune responses for cytotoxic killer T-cells. This has led to new ways of eliminating cancer cells by using the immune system, in addition to other available methods (Yang et al., 2015).

#### 2.4.1 Radiation Induced Abscopal effect and Immunogenic Cell Death

Radiotherapy (RT) is commonly perceived as an immunosuppressive procedure, useful for killing immune cells and preparing patients for procedures such as bone marrow transplants by minimizing the risk of rejection of transplanted cells (Sabloff, 2021; Liu, 2018). Contrary to this, the immune system does have an influence over tumor control, even after radiotherapy. Over 30 years ago it was demonstrated in murine fibrosarcoma that the required radiation dose to control 50% of the tumors was significantly lower in immunocompetent mice, 30 Gy as opposed to 64.5 Gy for T-cell deficient mice. In addition, the immunocompetent mice had lower incidence of metastases (Liu et al., 2018). There is also evidence of using RT to induce immunogenic signaling.

The first piece of evidence that suggests that the immune system can be stimulated by RT comes from clinical observations of tumors remission outside the radiation field in secondary tumors. This is known as an “abscopal effect”, from Latin “ab scopus” meaning away from the target (Ajona et al., 2018). However, these abscopal effect rarely happen with RT alone and emerge more frequently in patients receiving combined treatments such as RT and IT such as ICBT (Liu et al., 2018).

Abscopal effects occur due to Immunogenic cell death (ICD). ICD is a special type of apoptosis that elicits an immune response. Some tumors lack the inflammatory cytokines and chemokines to attract cells such as dendritic cells (DCs), macrophages, and T-cells. RT changes the tumor microenvironment by releasing tumor neoantigens which may potentially induce an effective immune response and cancer control. The stress response induced by irradiation causes pre-apoptotic release or translocation of danger associated molecular patterns (DAMPs), such as ATP, high-mobility group box 1 (HMGB1) and calreticulin ATP



attracts DCs and monocytes that act as scouts by alerting the rest of the immune system. HMGB1 is a protein that binds to surface pattern recognition receptors which can cause an inflammatory response. In addition, HMGB1 can facilitate DC maturation, increasing the efficiency of antigen presentation to T cells. Calreticulin promotes phagocytosis and supports anticancer immunity. In other words, Calreticulin acts as an “eat me” signal and activates immune system to engulf and kill cancer cells (Liu et al., 2018).

### 2.4.2 Calreticulin

Previously, in section 2.2.1 we mentioned calreticulin’s role as an ER resident protein. In response to ICD in cancer cells calreticulin is translocated from the ER lumen to the surface of the cell membrane. Here it acts as an important phagocytic signaling agent for the immune system. This facilitates the uptake of dying cells or their corpses by antigen presenting cells (APCs), including immature DCs that migrate to lymph nodes to cross prime naive CD8<sup>+</sup> T cells. Several studies indicate that the expression of CRT is related to formation of tumors. The level of membrane-exposed calreticulin varies considerably between different cancer types.

According to Fucikova et al. there is prognostic and predictive value to the levels of calreticulin expression in cancer cells (Fucikova et al., 2021). Low expression of CRT has been associated malignant features such as hyperproliferation in preclinical models of prostate cancers. Meanwhile, higher levels of CRT expression has been linked with improved disease outcome. This makes calreticulin a prime candidate for measuring immunogenic signaling in cancer cells (Fucikova et al., 2021; Liu et al., 2018).

## 2.5 Dosimetry

Radiation Dosimetry deals with the measurement of absorbed dose or dose rate resulting from the interaction of ionizing radiation with matter (Attix, 1986). Dosimetry can be performed by a dosimeter, a device that typically measures another quantity such as temperature or charge which can be related to the absorbed dose in matter. There are many different types of dosimeters, we will focus on the ones that are relevant for this thesis.

### 2.5.1 Ionization Chambers

An ionization chamber (IC) is a device that measures dose based on the charge released by ionizing radiation. ICs can act as absolute or relative dosimeters. An enclosed volume is filled with a sensitive medium such as air, and a voltage is applied which causes an electric field between an anode and a cathode. Ionizing radiation which enters the volume creates ion pairs, a positive ion and a dissociated electron. Due to the electric field, the charged particles are

forced to opposing electrodes and ideally do not recombine. This induces an ionization current, which is measured by an electrometer. The cumulative charge which is measured is related to the number of ionizations (energy deposited per charge) and therefore to the absorbed dose, when the density and mass of the irradiated gas is known (Attix, 1986; Podgoršak, 2016).

Transportable ICs such as cavity ICs can be used as absolute dosimeters, if they are calibrated by certified calibration laboratories. The calibration can be done by using a free-air ionization chamber. The dimensions and walls of a free-air ionization chamber allow for charged particle equilibrium to be achieved for accurate measurement of charge based on the incident X-ray irradiation. In other words, air kerma  $K_{air}$  is equal to the absorbed dose, neglecting bremsstrahlung losses. Utilizing this allows calibration of cavity ICs which are easy to use and have fewer limitations (Attix, 1986).

We are interested in the dose received by biological tissue which mostly consists of water. By using cavity theory, we can relate the dose given to the air inside the IC to dose given to water equivalent matter at the same point. For a calibrated IC we can use Eq. (19), where  $N$  is the calibration constant ( $Gy/C$ ),  $D_w$  is the known dose ( $Gy$ ) to water and  $M$  is the ion chamber reading from the electrometer ( $C$ ) (Attix, 1986). Multiplying the IC charge reading with the calibration constant yields the dose given to water equivalent matter.

$$N = \frac{D_w}{M} \quad \text{Eq. (19)}$$

## 2.6 Flow Cytometry

This section is based on “Flow Cytometry: An overview” (McKinnon, 2019), “Flow Cytometry: Basic Principles and Applications (Adan et al., 2016) and “Basic Parameters Measured by a Flow Cytometer: What is Scattered Light and Absolute Fluorescence?” (Duggan, 2016).

A flow cytometer is an instrument capable of analyzing multiple parameters of individual cells or particles based on scattered and fluorescent light signals. Traditional flow cytometers are comprised of three main systems: The fluidic, optical and electronic systems; these are illustrated in Figure 22.

# Flow Cytometry

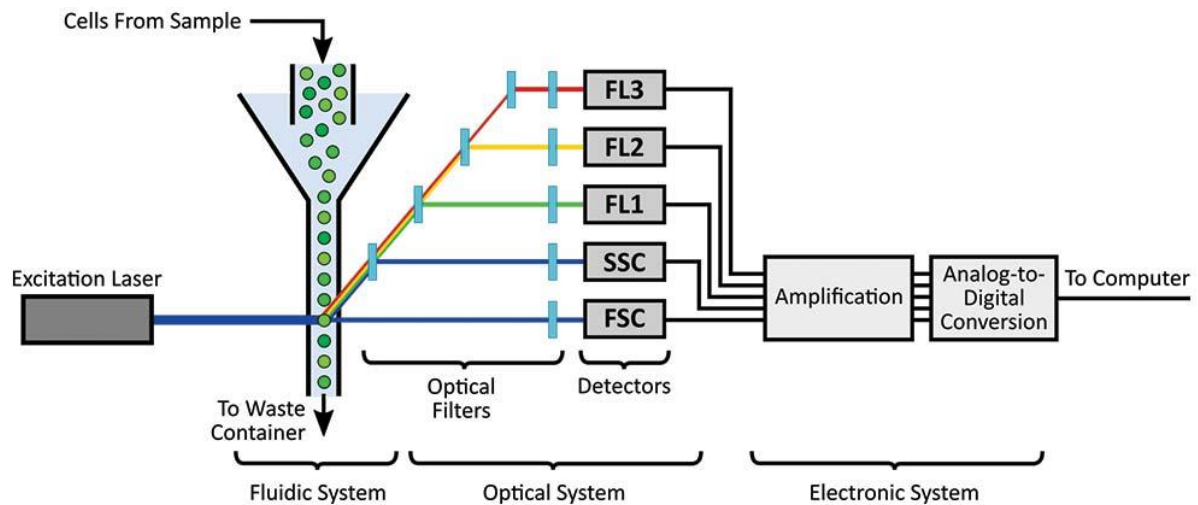


Figure 22: Schematic of a traditional flow cytometer, illustrating the fluidic, optical and electronic systems. (Sapkota, 2022)

## The Fluidic system

The fluidic system consists of sheath fluid, typically a saline solution which allows the transport of the sample cells, ideally one at a time through the laser interrogation point. Cells suspended in a fluid are injected into the machine and flow through a nozzle called the flow chamber as the central core. The sheath fluid flows as an outer layer of the central core, creating a coaxial flow. The sheath fluid and the sample fluid have different pressures and different flow rates which causes hydrodynamic focusing of the cells/particles allowing for detection and analysis of single cells/particles at a time through the optical system (Adan et al, 2016; McKinnon 2019).

## The Optical System

The optical system consists of excitation lasers and detectors, which generate and collect the signals that are used for sample analysis. It is the detection of scattered light which gives information about the size, shape, optical density, granularity and fluorescence of the cells. There are two main types of scattered light in flow cytometry, these are forward scattered (FSC), and side scattered (SSC) light. Detected FSC gives information about the size and shape of the cell. This is based on light that is scattered along the same axis as the initial laser light. There is also an obstruction bar which blocks light going directly from the laser to the FSC detector to avoid it from getting overwhelmed (Duggan, 2016). On the other hand, SSC represents light that is scattered through reflection and refraction of light in all directions,

detected orthogonally to the forward scattered light. SSC depends on the granularity or internal complexity of the cell and the cell size as well. As more objects such as organelles are in the way, the light gets increasingly side scattered. Fluorescent light is detected along with the light from SSC (Adan et al, 2016).

The absorption and subsequent emission of electromagnetic radiation (light), also known as fluorescence is an important part of the optical system in flow cytometry. Fluorochromes are fluorescent chemicals that are used as detection reagents, they absorb specific wavelengths of light and re-emit it at a longer wavelength. Attaching fluorochromes to molecules such as antibodies allow detection of membrane bound antigens on the surface of cells, thus giving information about immunological properties of cells. Detection of fluorescence is achieved by a series of dichroic filters (mirrors) along the SSC channels steering the fluorescent light to specific detectors and bandpass filters, which determine the light wavelengths that are read. This allows for detection and measurement of fluorochromes. Dichroic filters allow the passage of either shorter or longer wavelengths of light while reflecting the remaining wavelengths at an angle. For instance, a 450 Dichroic Long Pass filter (DLP) allows passage of wavelengths of light that are longer than 450 nm and reflects light with shorter wavelengths to a detector. Bandpass filters only allow the passage of a small window of specified light wavelengths. An example would be a 450/50 bandpass filter, which passes fluorescent light with wavelength  $450 \pm 25 \text{ nm}$  (McKinnon, 2019). This way the detectors only get specified wavelengths of light corresponding to those emitted by fluorochromes.

### **The Electronic System**

Lastly the electric system converts the light signals in the detectors into signals that can be read by a computer. This is done by converting the light signals into electrical signals such as a current. This can be achieved by photodetectors such as photomultiplier tubes (PMTs) or photodiodes which absorb photons and release electrons. The electrons travel to an amplifier and are converted into voltage pulses. These signals are processed by analog to digital converters (ADC) making digital data which is displayed as plots or histograms (Adan et al, 2016).

### **Flow Cytometry Relativity**

The important thing to remember with flow cytometry is that everything is relative. The dots on plots or the hills on a histogram have no absolute value as they can be adjusted by the voltage applied to the detectors. For any measurement there needs to be a control to compare it to some reference. Finding a value  $X$  for a stained cell sample does not give any insight unless there is an unstained sample and/or a similarly stained sample of different cells to make a comparison (Duggan, 2016).

## 3 Materials and Methods

### 3.1 Tumor-cell Lines and Practical Cell Culturing Techniques

All the experimental work done during this thesis was performed in the cell laboratory at the department of Biological and Medical Physics and the Oslo Cyclotron Laboratory (OCL) in the University of Oslo (UiO), Blindern.

#### 3.1.1 Cell Lines

Studying cells requires removal of cells from animals or plants and their subsequent growth in a favorable artificial environment, also known as a cell culture. A primary cell culture refers to a cell culture that has grown until it occupies the surface it grows on (reaches confluence) and is subcultured (passaged) by transferring to a new vessel with fresh medium and is provided room for continued growth. If the cells survive the first subculture the primary culture becomes a cell line (Davis, 2011).

Three cell lines were used during this thesis. The first one being A549 (human lung epithelial cells), commonly used for research and drug testing. A549 was bought from American Type Culture Collection (ATCC) and have been used by previous master students because of high levels of membrane bound calreticulin after X-ray irradiation (Thingstad, 2019; Ruud, 2020). The cell line was developed by D. J. Giard et al. in 1972 by removing pulmonary carcinoma tissue from a 58-year-old Caucasian male (Giard et al. 1973). The other two cell lines were MOC1 and MOC2 (Mouse oral squamous cell carcinoma) bought from Kerafast. MOC1 was derived from primary tumors in C57BL/6WT mice and is very immunogenic. MOC2 is less immunogenic and was derived from chemokine receptor CXCR3 deficient mouse on a pure C57BL/6 background. These cell lines were chosen because they can be used in a syngeneic mouse model (C57BL/6J) to study immunogenic response in vivo.

#### 3.1.2 Cell Cultivation: Culture Growth Conditions, Media and Dissociation of Cells

##### Cell Flasks and Dishes

All cells were grown in T25 (25 cm<sup>2</sup>) flasks. Occasionally during shortages (due to the pandemic) or for cyclotron experiments petri dishes (100mm x 15 mm) were used. The T25 flasks came with two cap options, vented or filter caps. Vented T25 (T25V) were used for irradiation experiments, while filtered T25 (T25F) were used for seeding or control flasks. T25V has the option of fully closing the flask, allowing no gas exchange during irradiation and transport. T25F can also be sealed using parafilm, if no vented flasks are available.

Previous protocols for calreticulin assay would use T75 (75  $cm^2$ ) flasks for control cells, in section 3.4 we will discuss why these were not needed anymore.

### **The Medium**

A cell culture medium provides the cells with essential nutrients, vitamins, inorganic ions, cofactors, metabolic substrates, amino acids and trace elements required to support cellular functions and proliferation. These components are supplied by the basal medium but is not enough to support cell viability for more than a few hours. To induce cell growth and multiplication basal media are supplemented with growth factors through fetal bovine serum (FBS) (Davis, 2011).

A549 cells were supplied with a 1: 1 mixture of Dulbecco's Modified Eagle Medium and Ham's F-12 (DMEM F-12). This gives the cells a high concentration of glucose, amino acids and vitamins with F-12s wide variety of components. As DMEM F-12 contains no proteins, lipids or growth factors the medium should be supplemented with 10% FBS. MOC1 and MOC2 were sustained by Iscovo's Modified Dulbecco's Media (IMDM) which is better suited for rapidly proliferating, high-density cell cultures IMDM was also supplemented with 10% FBS.

Before use, the bottles or vials containing the media were heated for approximately 15 minutes in a Grant JB Aqua 18 water bath set to a temperature of 37 °C.

### **The Buffer Solution and PH**

Media need to be buffered to maintain PH levels. Generally, an optimal pH condition for a mammalian cell culture is between 7.0 – 7.4, although exceptions do exist. Bicarbonate is both an important nutrient for cells and a buffer that is used in basal media, such as DMEM F-12 and IMDM. In order to maintain the pH the basal media are designed to have, an atmosphere of 5 – 10%  $CO_2$  is required (Davis, 2011). To accommodate for this, the incubators were injected with  $CO_2$  until they reached an atmosphere of 5%  $CO_2$ .

If cells were to be suspended immediately or washed after a procedure, we used phosphate buffered saline (PBS), to not waste basal medium or cause any unwanted cellular effects during an experiment. PBS is a salt solution that maintains the PH-values and the tonicity of the cells in a normal air atmosphere. The PBS that was used during this thesis came in bottles of 1:10 concentration, meaning that we would add 1 part concentrated PBS to 9 parts purified/deionized (milli-Q) water. In our case we added 50  $mL$  concentrated PBS to 450  $mL$  milli-Q water which yielded a bottle of 500  $mL$  to be used for experiments.

## **Trypsin**

Trypsin is an enzyme that hydrolyses proteins and was used as a dissociating agent. The main use of trypsin is to remove cells from flasks/dishes and make cell suspensions. Typically, trypsin is combined with EDTA, Ethylenediaminetetraacetic acid (Trypsin-EDTA) which enhances the trypsin activity by acting as a chelating agent. Prior to use, trypsin was heated in a water bath.

For calreticulin experiments we replaced trypsin-EDTA with TrypLE. TrypLE outperforms trypsin in preserving cell surface epitope expression and can directly substitute trypsin without protocol changes (ThermoFisher, 2020).

### **3.1.3 Cell Cultivation: Seeding, Sterility and Incubation.**

#### **Seeding**

All cells during this master thesis were ordered and prepared in flasks or dishes by Julia Marzioch or occasionally by Joe Alexander Sandvik, Olga Zlygosteva or Ingunn Hanson. These cell flasks were placed in the incubators with medium, ready for use. For calreticulin experiments our work only included irradiation, incubation and analysis of cells.

For cell survival experiments with MOC1 cells one flask of cells was ordered. These cells were seeded into several flasks depending on the number of irradiation doses. For each experiment, 8 controls T25 flasks (0 Gy) were seeded and used to calculate the plating efficiency. For each intended irradiation dose, 4 T25 flasks were seeded.

#### **Sterility**

Working in a cell laboratory, sterility is a major concern. The growth rates of animal cells are relatively slow requiring around 24 hours compared with bacteria which can double roughly every 30 minutes (Davis, 2011). For experiments such as those concerning cell survival where cells are kept inside an incubator for several days, contamination could result in infection and unwanted loss of cells. During all kinds of laboratory work disposable gloves were used and strayed with 75 % ethanol before contact with any other equipment, containers or cell flasks.

All containers and equipment were sterilized by spraying 75 % ethanol before use.

Procedures where long-term sterility was a concern, such as cell cultivation and seeding were performed in a laminar air flow (LAF) bench. Inside the LAF-bench air is filtered through a



high efficiency particulate air (HEPA) filter which removes particles including potential pathogens, thereby keeping the inside of the bench sterile. Figure 23 shows the most used LAF-bench (Gelaire, Australia and Safe 2020, Thermo Scientific).



*Figure 23: Photograph of the main LAF-bench in the department of biological and medical physics at UiO, cell laboratory, room KV342.*

Every equipment was sterilized by spraying with 75% ethanol before being placed inside the LAF-bench. The LAF bench was cleaned after use with 5% Virkon solution, milli-Q water and lastly sprayed with 75% ethanol.

The calreticulin assay does not have a strict requirement for sterility. Cells are prepared and analysed with flow cytometry in a relatively short time. After incubation following the irradiation, the rest of the experiments were therefore performed without a LAF-bench.

### **Incubation**

Cells in flasks or dishes were incubated in a Thermo Scientific Steri-Cycle  $CO_2$  incubator (Thermo Scientific Forma, USA), a Steri-Cult 200  $CO_2$  incubator (Thermo Forma 3307, USA) or a Thermo forma Series II water jacketed  $CO_2$  incubator. The temperature of the incubators was set to 37 °C and  $CO_2$  saturation of 5%. Inside the incubators, a water bath was placed at the bottom to evaporate water and maintain a humidity between 80 – 90% to avoid drying of the cell media.

## 3.2 X-ray Irradiation

### 3.2.1 Preparation

Experiments involving X-ray irradiation were performed in the basement of the chemistry building at UiO, room VK08. Before use, the X-ray system (PANTAK PMC 100, Pantak, USA) requires warming up for about 20 minutes. Before that we turn on a heater. Below the X-ray chamber is a heater that warms the surface the cells are placed on, up to 37 °C, see Figure 24 for X-ray set-up.



*Figure 24: Photograph of X-ray set-up. From Bottom to top, 1. is the heater, 2. Is the X-ray chamber and 3. Is the X-ray tube, the source of the X-rays.*

To minimize the risk of contaminating and damaging the cells, multiple precautions were taken. The cell laboratory is on the third floor of the chemistry building in room KV342, while the X-ray machine is in the basement. The vented cell flasks were sealed tightly and during shortages filter cell flasks were sealed with parafilm to maintain sterility and  $CO_2$  levels while transporting and irradiating the cells.

The cell flasks/dishes were transported in a Styrofoam box that was sprayed with ethanol and left to dry before use. Near the X-ray room in the basement of the chemistry building is a cell laboratory room VK10B with a LAF-bench room where cell flasks were placed before irradiation. The room acts as an incubator with a temperature around 37 °C. All preparation

before X-ray irradiation were performed here. On the LAF-bench there is PMMA slabs with 4 cavities for 4 flasks, shown in Figure 25. There are similar slabs for dishes. This allows for irradiation of four samples at a time, for a given dose. The flasks or dishes were placed on one of these slabs and transported in the Styrofoam box when the X-ray machine was ready.



*Figure 25: Photograph showing the LAF-bench and the PMMA slabs located in a room in VK10B. Before X-ray irradiation the cells flasks are kept here.*

### 3.2.2 Irradiation

The X-ray machine is separated from the X-ray room by thick walls and a door reinforced with lead plating to minimize radiation leakage. The door to the X-ray machine and the X-ray chamber lid is connected to a safety switch, meaning that if either one is not closed properly the X-ray machine will not start.



*Figure 26: Photograph of X-ray chamber. We see the PMMA board which can be slid into different distances from the X-ray source (top of the chamber). The PMMA slab (in Figure 25) is placed along the tapes at the center of board with the cell culture flasks/dishes.*

Inside the X-ray chamber is a flat PMMA board which can be slid into different positions corresponding to different distances from the X-ray source, see Figure 26. Our experiments were performed at a distance of 60 cm from the X-ray source. The settings used for X-ray experiments were a voltage of 220 kV with a current of 10 mA. The X-rays were filtered with 1.52 mm aluminium and 0.7 mm thick sheet of copper. Dosimetry had already been performed in this configuration and a table such as Table 1 is provided for the dose rates.

Time	Dose
<b>1 minute and 37 seconds</b>	1 Gy
<b>3 minutes and 14 seconds</b>	2 Gy
<b>8 minutes 4 seconds</b>	5 Gy
<b>16 minutes 8 seconds</b>	10 Gy

*Table 1: Irradiation time for a given dose (dose rate). The Settings for the X-ray machine is 220 kV across X-ray tube with a current of 10 mA, using 1.52 aluminum and 0.7 mm copper filters.*

After irradiation the cells were transported to the LAF-bench in room VK10b or to one of the incubators in the cell laboratory, room KV342.

### 3.3 Proton Irradiation

Proton irradiation experiments were performed at the Oslo Cyclotron Laboratory (OCL) with the Scanditronix MC-35 Cyclotron. The laboratory is in the basement of the physics building at Blindern Campus of the University, which is across the chemistry building (Görge et al., 2021). The cyclotron experiments were performed as a group, including the author of this thesis, fellow master students, supervisors, two cyclotron engineers, PhDs and Senior engineers. Figure 27 shows the floor plan of the OCL, we were using beamline 4.

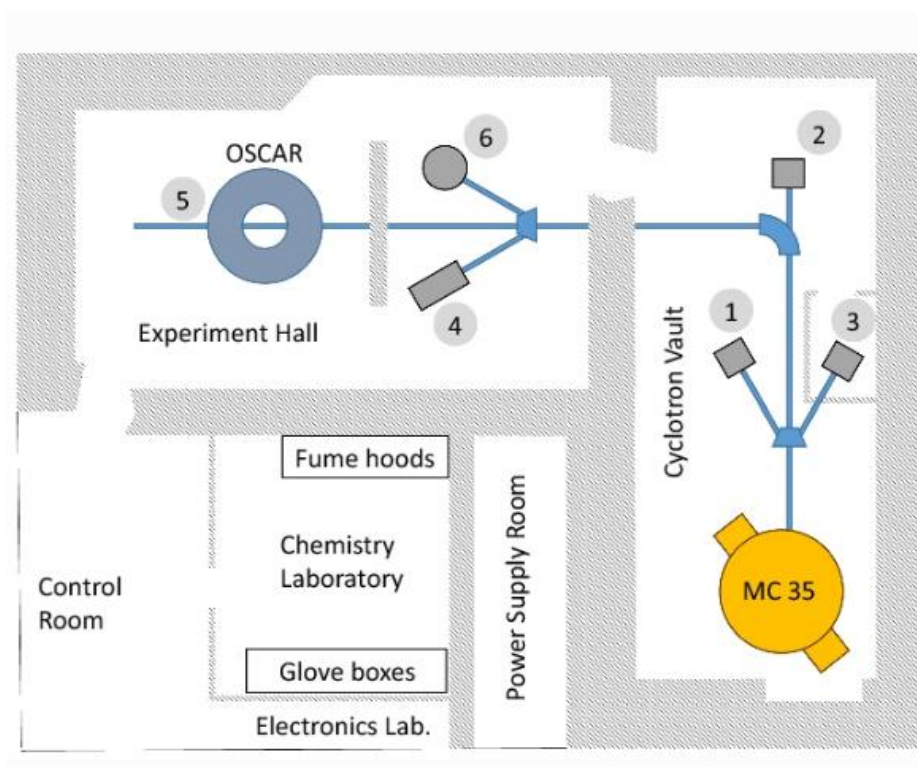


Figure 27: Floor plan of OCL showing the cyclotron vault, experiment hall and adjacent laboratories (Görge et al., 2021)

#### 3.3.1 Preparation

The Cyclotron is shared between many researchers and requires constant maintenance. As such we were only allowed to use the cyclotron for 4-5 days at a time to perform experiments. Preparation had to be done before the “proton week”. Some days prior to proton irradiation Parafilm was cut into strips and pieces, sterilized by soaking in a 75% ethanol bath for 20 minutes and left to dry overnight in a LAF-bench before being placed in sterile glass dishes. The equipment that was going to be used was autoclaved and/or sterilized and placed in a room designated for biomedical physics in the OCL facility a week before irradiation. This included laboratory coats, cotton swabs, disposable gloves, a glass beaker, adhesive tape,



pipettes and an electronic pipette. A few days prior to irradiation cells were seeded in cell dishes.

The day of the irradiation, medium was heated and taken to the LAF-bench inside the OCL facility. The cell dishes were placed in an incubator in the same room. Before irradiation cell dishes were taken out one at a time and placed on the LAF-bench. Here the medium was removed and discarded into a beaker with the electronic pipette and pipettes. In addition, a cotton swab was used to remove the few drops of medium that were left. The cell dishes were placed inside a sterilized and heated PMMA cylinder, which was fitted to the cell container. In addition, there was a small motor in the cell container which would rotate the PMMA cylinder and the cell dish slowly during irradiation, to avoid any drips of medium collecting at the sides of the cell dish.

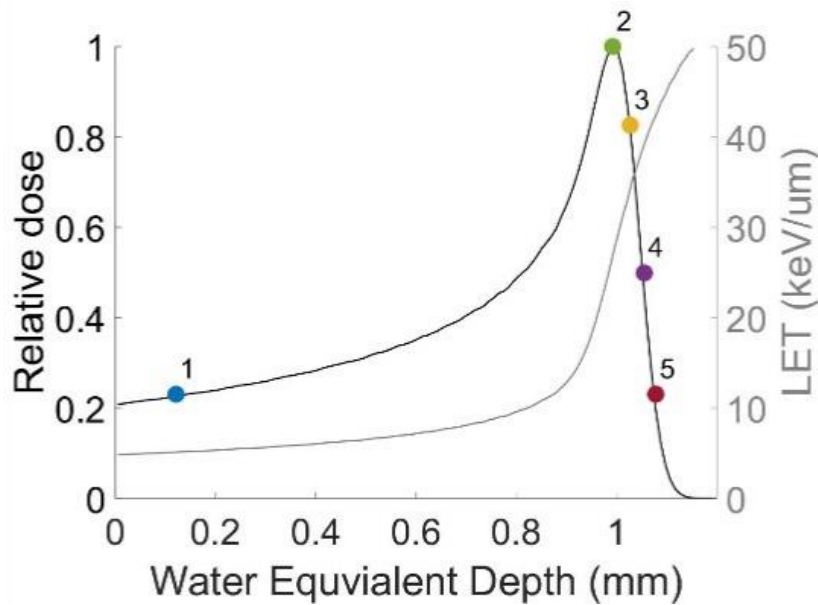


Figure 28: Dose-depth curve (black) and LET-depth curve (grey) made by Anne Marit Rykkelid based on LET values found with Monte Carlo simulations by Delmon Arous (unpublished).

There were two main configurations giving equal dose position 1, front of Bragg peak, lower LET protons ( $\sim 10 \text{ KeV}/\mu\text{m}$ ) and position 5, back of Bragg peak, higher LET protons ( $\sim 40 \text{ KeV}/\mu\text{m}$ ) as seen in Figure 28. Cell dishes to be irradiated position 1 were placed inside the PMMA cylinder with a parafilm lid which was secured with adhesive tape. A Cell dish to be irradiated in position 5 had its cell dish lid on, sealed with parafilm, also inside the PMMA

cylinder. There was also a slight difference in distance from beam window between the lid and parafilm due to their differences in stopping power.

### 3.3.2 Proton Dosimetry

Dosimetry was performed before irradiation and occasionally between irradiation sample sets, due to fluctuations in ion source current supply.

Beam line 4 is used for irradiation of cells and other samples in air. A 50  $\mu m$  thick tungsten window is used to scatter the beam into air, producing a homogenous particle radiation field. EBT3 films were used to measure the beam homogeneity, but we did not partake in these measurements. Dosimetry measurements were performed by two ionization chambers. One of these was as a transmission monitor chamber (MC), used to measure the fluence of particles or monitor units (MU). The MC is a thin ionization chamber and has minimal effect on proton beam. The other ionization chamber is used as a dosimeter, measuring the charge corresponding to the absorbed dose and had been calibrated at the Norwegian Radiation and Nuclear Safety Authority. The calibration factor for the ionization chamber was  $N = 1.411 \text{ Gy/nC}$ . The ionization chamber was used in conjunction with the transmission MC in order to relate the particle fluence (MU) to the given dose when the ionization chamber was replaced with the cell container. The general set-up in the experimental hall can be seen in Figure 29. This area was cleared of people when the cells were ready for irradiation.

The ionization chamber used for dosimetry was connected to an electrometer (MAX4000, Standard Imaging, USA), while the transmission MC was connected smart reference class electrometer (Unidos Tango, PTW, Germany). The former allowed for remote control and measurement on a computer which was necessary to measure the dose during irradiation and stop the beam accordingly.

To find the two configuration, position 1 and position 5, we had to identify the positions for the front, top and back of the Bragg peak, while simultaneously measure dose rates for a given fluence.

Because of the low energy of the protons (15 MeV), the lid on the cell dishes absorbed enough radiation to reach the Bragg Peak and for irradiations in front of the Bragg peak, the cell dishes were covered with parafilm instead. To find position 1, we would therefore place a sterile parafilm sheet in front of the ionization chamber. Position 5 was chosen as the position behind the Bragg peak with the same dose rate as position 1. To find this, a cell dish lid was

placed in front of the ionization chamber and the position of the chamber was adjusted using the readings of the transmission chamber relative to the reading of the ionization chamber. Thus, by identifying these two equivalent dose and dose rate positions (1 and 5) we could determine that any differences between these samples were due to the differences in LET.

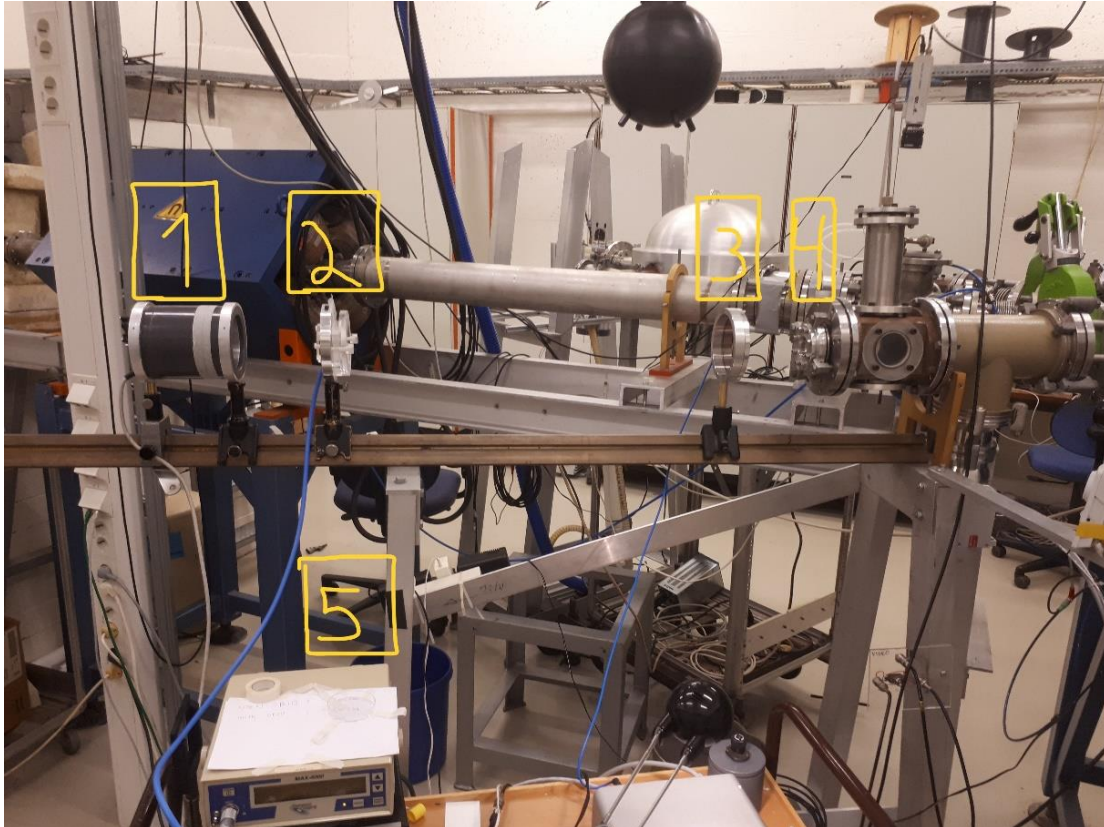


*Figure 29: The set up during proton irradiation preparation at beam line 4. 1 is the cell container attached to a heater. 2 is the ionization chamber connected to 5, the electrometer. 3 is the monitor chamber, 4 is the beam exit window.*

### 3.3.3 Proton Irradiation

The cells were prepared as described above and placed inside the heated cell container and the rotating motor was turned on. As the cell were ready for irradiation and the experiment hall was cleared, we waited in front of the control room. The cyclotron ion source was always on, to irradiate cells we had to press a button which would remove the cup stopping the proton beam from entering the experiment hall. This cup was removed and the particle fluence was measured until it reached a certain value, which had been determined by dosimetry



measurements. This was done by a person, in our case a fellow master student manually pressing the button and estimating when to stop the beam to reach the required dose. All samples for calreticulin assay were ideally irradiated with either 4 Gy or 8 Gy, which took less than 30 seconds as the dose rate was relatively high compared to X-rays (see Table 1). The exact dose given was noted for each cell dish. While a sample was being irradiated the next sample was prepared in the LAF-bench.

After proton irradiation we waited until it was safe to enter the experimental hall. There were ionizing radiation detectors inside the room which would light up as red, yellow or green, depending on the ionizing radiation levels. The colours indicate the dose rate, and we were only allowed to enter when the detectors were green. We would then go into the experimental hall and transfer the cells to the LAF-bench where medium was added, and the cell dish was placed in the incubator. The next cell dish was prepared and placed inside the PMMA cylinder.

For each calreticulin assay experiment there were 3 cell dishes that received proton radiation and 1 cell dish which was left in the incubator as control, so 4 samples in total for each dose. Three different cell lines (A549, MOC1 or MOC2) were given two different doses (4 Gy or 8 Gy) in two different positions (1 or 5) during the proton week.

## 3.4 Survival Curves

### 3.4.1 Colony Formation Assay

In order to find cell survival curves, we need to perform a clonogenic or colony formation assay (CFA), which can be found in appendix 5. This involves seeding a certain number of single cells in flasks, irradiating them, waiting and counting the number of colonies that survived. The process and time between procedures can vary based on the cell line, we will describe the protocol used for MOC1 and MOC2 cells. I was tasked with finding the survival curve for MOC1 cells while a fellow master student, Frida Larsen, performed the same experiments and provided data for MOC2 cells.

The first step in CFA was to obtain cells. As mentioned, the cells were ordered and for CFA all we needed was a T25 flask or two (as a reserve). Ideally, the flasks are neither too full nor too empty with cells, about 60% – 80% confluent worked for us. Since the cell flasks are supposed to be in the incubator for days or weeks after seeding and irradiation, sterility is a major concern. The work was therefore done in a LAF-bench.

The number of flasks depended on the number of treatments the cells were to receive. Table 2 gives an overview of the number of flasks and the number of cells seeded for each treatment. In total this means 29 flasks were marked and prepared, this could be done while waiting for the heating of trypsin and IMDM medium in the water bath. After marking, the flasks were placed in a sterilized metal tray, filled with 4 ml medium and the tray along with the flasks were subsequently placed in an incubator. For T25V flasks the lids were half sealed to allow for gas exchange and create an optimal environment for the cells that were to be seeded.

Dose/treatment	Number of flasks	Cells seeded in each flask
<b>0 Gy (control)</b>	8	200
<b>1 Gy</b>	4	200
<b>2 Gy</b>	4	200
<b>5 Gy</b>	4	500
<b>7.5 Gy</b>	4	1500
<b>10 Gy</b>	4	10 000
<b>0 Gy (multiplicity)</b>	1	10 000

Table 2: Overview of the doses and corresponding flasks and ideal number of cells seeded in each flask for CFA.

## Trypsinization

When the unseeded cell flasks were ready, we started making a single cell suspension. We took an ordered cell flask, removed the medium, flushed with PBS (4 *ml*) or Trypsin-EDTA (1.5 *ml*) and added trypsin-EDTA (3 *ml*). The cell flask was then placed in an incubator for 8 – 10 minutes, normally 4 minutes is enough but MOC1 cells are as mentioned, especially adhesive and difficult to disassociate from the cell flask surface. While waiting, we filled a tube with 3 *ml* medium. After waiting until the cells were sufficiently disassociated, we used a 2 *ml* pipette with a rubber bulb to create a single cell suspension by continuously resuspending the cells. The single cell suspension was then pipetted into the tube prefilled with 3 *ml* cell culture medium. The medium was used to neutralize the trypsin cells.

Afterwards, the tube with a 6 *ml* mix of trypsinized cells and medium was then centrifuged for 4 minutes at 200 g. After centrifuging, the fluid in the tube was aspirated and the cell pellet was subsequently resuspended in 5 *ml* medium.

## Finding the Cell Concentration

The next step was to use a cell counter to find the cell concentration. In the same cell lab, room KV342, there was a cell counter (IPRASENSE, NORMA XS, France) connected to a laptop. Using a micropipette, we deposited a 13  $\mu\text{l}$  sample from the cell suspension to a cell counting fluidic chamber. The chamber was placed on the measuring slide and analyzed using a software program called HORUS. The program yielded the number of viable cells per *ml*. A typical value would be around  $200\,000 \frac{\text{cells}}{\text{ml}}$ .

## Cell Suspension Dilution

After finding the cell concentration in our cell suspension tube the next step was to dilute the cells accordingly. Each cell flask would receive 1 *ml* of a cell suspension. We knew from Table 2 that 16 flasks should be seeded with 200 cells, 4 flasks with 500 cells, 4 flasks with 1500 and 5 flasks with 10 000 cells. This gave us an idea of how much of each concentration we needed.

The goal was to minimize medium waste while having a comfortable amount of fluid to seed the cell flasks. The cells were constantly resuspended before and after transfer using a 2 *ml* pipette and rubber bulb to ensure that the concentrations were correct. Using  $200\,000 \frac{\text{cells}}{\text{ml}}$  as an example, we started by diluting with 1: 10. This means we filled a tube marked  $\frac{20000}{\text{ml}}$  with 9 *ml* medium and pipetted 1 *ml* from our  $200\,000 \frac{\text{cells}}{\text{ml}}$  tube. To get to  $10\,000 \frac{\text{cells}}{\text{ml}}$  we needed a 1: 2 solution, but this would be too little for further use. We therefore made a 4:8 solution,

meaning a new tube marked  $\frac{10000}{ml}$  filled with 4 *ml* medium and we added 4 *ml* from the  $\frac{20000}{ml}$  tube. The next concentration was  $1500 \frac{cells}{ml}$  which was achieved by diluting  $10\ 000 \frac{cells}{ml}$  by 1: 6.67, meaning a tube marked  $\frac{1500}{ml}$  filled with 5.57 *ml* medium and adding 1 *ml* from  $10\ 000 \frac{cells}{ml}$  tube. For  $500 \frac{cells}{ml}$  we would dilute  $\frac{10000}{ml}$  again by 0.5: 10, i.e. new tube with 9.5 *ml* medium and 0.5 *ml* from  $\frac{10000}{ml}$  tube. Similarly, the concentration of  $200 \frac{cells}{ml}$  was achieved by diluting  $\frac{10000}{ml}$  by 0.5:25, a tube with 24.5 *ml* medium and 0.5 *ml* from  $\frac{10000}{ml}$ . In total we would have 25 *ml* of  $200 \frac{cells}{ml}$ , 10 *ml* of  $500 \frac{cells}{ml}$ , 6.67 *ml* of  $1500 \frac{cells}{ml}$ , 6 *ml* of  $10\ 000 \frac{cells}{ml}$  for use. This covered what we needed considering the number of flasks, as seen in Table 2.

### Cell Flask Seeding

When we had tubes filled with the desired cell concentrations ready it was time to seed the cell flasks. The flasks were taken out of the incubator and seeded one at a time using a 2 *ml* pipette and a rubber bulb. Before seeding, the cells in the tubes were thoroughly resuspended to maintain an even concentration. As mentioned, each flask would receive 1 *ml* of their respective cell concentration based on Table 2. After seeding, the cell flasks were placed in an incubator on the same metal tray.

### X-ray Irradiation

After waiting 5 – 6 hours the cells would adhere to the bottom of the cell flask and were ready for irradiation. The X-ray irradiation process is explained in section 3.2. During or after X-ray irradiation the multiplicity flask with 10 000 cells was fixated (explained below). After irradiation the cells would be placed in the incubator for a few days. The number of days varies considerably from cell line to cell line. MOC1 cells grow and divide rapidly, meaning that we waited less than a week. The first two experiments we waited 3 days, but after realizing that the cell colonies were relatively small, we tried 4 and 5 days. The experiments where we waited 4 days the colonies were still a bit small and when we tried waiting 5 days they were a bit too large as some colonies were on top of each other, making proper counting difficult. The best solution we found was to make a compromise. The flasks that received a high dose such as 5, 7.5 and 10 Gy had lower survival rates, as such they would be fixated after 5 days. The other flasks, the controls, 1 and 2 Gy samples were fixated after 4 days.

## Fixation

Fixation means stopping the cells in time by killing and staining them with a dye. To fixate cells we started by removing the cell culture medium and flushing the flasks gently with 3 *ml* PBS. The next step was to add 3 *ml* of 96% ethanol and expose the cells for 3 minutes. This was done to kill the cells without disrupting the structure and to permeabilize the membrane for the dye, methylene blue, to get into the cells. After removing the ethanol, methylene blue was added and left in the cell flasks for 5 minutes before it was removed for reuse and the flasks were washed with lukewarm water. The cell flasks were dried for 1-2 days before counting the colonies.

## Colony Counting

After fixation the colonies were visible to the naked eye as blue dots on the bottom of the cell flasks. We used a cell colony counter to mark and count the cells with a marker. To count as a survivor, a colony needs to consist of at least 50 cells. Colonies that looked relatively small or different was examined later using a microscope (Nikon Eclipse TS100, Japan) to confirm whether it should be counted or not.

### 3.4.2 Calculation of Cell Survival

Cell survival was calculated using the principles and equations described in Håvar Sollund's master thesis "Mechanism for Elimination of Low-Dose Hyper-Radiosensitivity" (Sollund, 2009). Multiplicity corrections were first developed by Elkind and Whitmore (1967), but the derivation used by Sollund was based on Melvik (1983).

First, we find the plating efficiency  $PE$  using Eq. (20) where  $N(C)$  is the mean number of surviving colonies in the control flasks (C),  $N_0$  is the number of cells seeded for each control flask.

$$PE = \frac{N(C)}{N_0} \quad \text{Eq. (20)}$$

The apparent surviving fraction  $F(B)$  for samples receiving treatment  $B$  (i.e. 5 Gy irradiation) is given as **Error! Reference source not found.**

$$F(B) = \frac{N(B)}{N_0(B) \cdot PE} = \frac{N(B)}{N_E(B)}, \quad \text{Eq. (21)}$$

where  $N(B)$  is the mean number of surviving colonies counted for flasks given treatment  $B$ .  $N_E(B)$  is the number of cells seeded for flasks given treatment  $B$  multiplied by plating

efficiency.  $N_E(B)$  is also known as the expected number of surviving colonies, in other words how many colonies that would have survived without treatment.

The standard error of the mean number of colonies  $\Delta N$  is given as Eq. (22)

$$\Delta N(B) = \sqrt{\frac{1}{n(n-1)} \sum_{i=1}^n (N_i(B) - N(B))^2}, \quad \text{Eq. (22)}$$

where  $n$  is the number of flasks in a set receiving treatment  $B$  and  $N_i(B)$  is the number of colonies counted in flask  $i$ .

The surviving fraction is a function of two variables,  $N(B)$  and  $N_E(B)$ . Therefore the error is given  $\Delta F$  is given as Eq. (23)

$$\Delta F(B) = \sqrt{\left(-\frac{N(B)}{N_E^2(B)} \cdot \Delta N_E(B)\right)^2 + \left(\frac{1}{N_E(B)} \cdot \Delta N(B)\right)^2}, \quad \text{Eq. (23)}$$

where  $\Delta N_E(B) = \frac{N_0(B)}{N_0(C)} \cdot \Delta N(C)$ .

### Correcting for Multiplicity

Ideally, all the cells were seeded one at a time, such that one colony formation unit (CFU) represented survival of a single cell. This seldom was the case and is corrected for using the multiplicity flask. As mentioned, this flask is fixated during or after irradiation in a CFA experiment. Later, by using a microscope CFUs such as singlets, doublets, triplets etc. of cells were counted to a total of around 200 CFUs. The multiplicity  $M$  is found as the sum seen in Eq. (24)

$$M = \sum_{i=1}^n x_i \cdot i, \quad \text{Eq. (24)}$$

where  $x_i$  is the fraction of CFUs which consisted of  $i$  cells. For example if we were to count a total of 200 CFUs with 125 singlets, 60 doublets, 10 triplets and 5 quadruplets the multiplicity in this case would be

$$M = \frac{125 \cdot 1 + 60 \cdot 2 + 10 \cdot 3 + 5 \cdot 4}{200} = 1.475.$$

To correct for the multiplicity we need to make some assumptions.  $S$  is the corrected surviving fraction, which is also the probability of maintaining clonogenic capacity,

independent of the number of cells in the CFU and of inactivation of other cells in the CFU. The fraction of cells losing their colony forming ability is  $(1 - S)$ . Independent survival of a cell is tied to the probability of inactivating a CFU with  $m$  cells,  $(1 - S)^m$ . This implies a corrected surviving fraction  $S$  given as Eq. (25), where  $F$  is the apparent surviving fraction from Eq. (21), for this specific CFU.

$$F = 1 - (1 - S)^m \quad \text{Eq. (25)}$$

For a population of CFUs containing up to  $n$ , the expected surviving probability is given as Eq. (26) which can be solved numerically for  $S$ :

$$F = \sum_{i=1}^n x_i (1 - (1 - S)^i) \quad \text{Eq. (26)}$$

Sollund further shows how to derive a simplified equation for the corrected survival probability  $S$ , seen in Eq. (26). For the special case where  $n = 2$ , meaning assuming only singlets and doublets in CFUs an analytical ( $n = 2$  approximation-based) solution can be derived which yields Eq. (27). If the number of triplets and quadruplets were very small, this is the equation we used to find colony survival corrected by multiplicity. Again,  $F = F(B)$  as seen in Eq. (21) and  $M$  is calculated by using the multiplicity flask.

$$S = \frac{M - \sqrt{(M-1)F}}{2(M-1)} \quad \text{Eq. (27)}$$

The standard error in Eq. (27)  $\Delta S$  is a function of  $F$  and  $M$ , given as Eq. (28).

$$\Delta S = \sqrt{\left(\frac{\partial S}{\partial F} \cdot \Delta F\right)^2 + \left(\frac{\partial S}{\partial M} \cdot \Delta M\right)^2} = \sqrt{\left(\frac{\Delta F}{\sqrt{M^2 - 4(M-1)F}}\right)^2 + \left(\frac{-1 + \frac{M-2(M-1)F}{\sqrt{M^2 - 4(M-1)F}}}{2(M-1)^2} \cdot \Delta M\right)^2} \quad \text{Eq. (28)}$$

We used the error in the multiplicity  $\Delta M = 0.03$  found by Sollund (Sollund, 2009) for our calculations of the standard error. For the average survival in multiple experiments we used the standard error of the mean (SEM).

In this thesis, there was a relatively high number of triplets and for the MOC2 cell line. The calculations were therefore performed both by an approximation using the solution for the special case  $n = 2$  with  $M$  calculated from Eq. (24) and as an exact solution of Eq. (26) found by Python programming.

## 3.5 Calreticulin Protocol Development

The goal with calreticulin assay is to detect membrane bound calreticulin based on the protocol received from Adrian Eek Mariampillai and his team from the Radiation Biology and DNA Damage Signaling group at the Institute for Cancer Research at Radiumhospitalet. Emma Thingstad (Thingstad, 2019) and subsequently Martine Dorthea Engelhardt-Olsen Ruud (Ruud, 2020) adjusted the protocols for A549 cells. We also implemented further protocol changes.

### 3.5.1 Adjustments for a New Protocol Assay

The original protocol used DyLight stained unirradiated (control) cells from a T75 flask as a control. This allowed the control cells to be mixed with the irradiated samples as an internal control, so-called barcoding. Thingstad used DyLight Alexa Flour 650 (Thermo Scientific, Germany) as a barcode to separate control (unirradiated) cells from irradiated cells with the flow cytometer (Thingstad, 2019). The DyLight stained cells were added to the irradiated samples, then antibodies were added and washed prior to flow cytometry. DyLight Alexa Flour 650 was used because the fluorochrome used for the calreticulin measurements emitted light at a lower wavelength. However, using live cells turned out to give a lot of autofluorescence with the same low wavelength. It was therefore decided to change fluorochrome for calreticulin in the experiments of Ruud (Ruud, 2020), which implied a change to DyLight Alexa Flour 488 for the barcoding. Hence, she tried various concentrations of DyLight Alexa Flour 488 (DyLight) for staining instead and was able to find the right concentration where separation of cells was possible. When we tried using this protocol it was difficult or at times impossible to distinguish the control and irradiated samples during flow cytometry. This was the case for all the cell lines we worked with. We tried Increasing the concentration and buying fresh DyLight. This slightly improved the results for A549 cells. However, there was no such improvement for MOC cells. We therefore decided to analyze the control and the irradiated samples separately. See Appendix 1 for “CRT Assay for Flow Cytometry (no dye, control as sample)”

The main change in the protocol was treating the controls as a normal sample. This removes the need for DyLight and cells in T75 flasks, as unirradiated cells in T25 flasks or dishes now was a separate sample as control. The previous protocols also used a different kind of control for the antibodies, one tube with irradiated and control cells did not receive any antibodies. This was used to measure autofluorescence. Since the dose response of the autofluorescence



was established, this was regarded as redundant as the sample receiving only secondary antibody can be used to correct for both the unspecific binding (of secondary antibody) and autofluorescence (fluorescence signal with no antibody) simultaneously for each sample.

Instead, we had a separate control sample which only has unirradiated cells and was split like the other samples, one receiving primary and secondary, the other only secondary antibodies. Otherwise, the same analysis was performed with flow cytometry. The ratio of the mean or median values of fluorescence intensity was calculated as seen in Eq. (29) (Thingstad, 2019; Ruud, 2020). To clarify, *Irr. sample (p + s)* is the sample that was irradiated and received primary and secondary antibody. *Irr. sample (s)* is the other half of a split sample which received only secondary antibody. Similarly, *Control(p + s)* is the unirradiated sample with both antibodies and *Control(s)* is the split which received only secondary antibody.

$$Ratio = \frac{Irr. sample (p+s) - Irr sample(s)}{Control(p+s) - Control(s)} \quad Eq. (29)$$

### 3.6 Calreticulin (CRT) Assay

The CRT assay was performed 48 hours after X-ray or proton irradiation, typically with 3 irradiated samples and 1 unirradiated control, which we also refer to as a sample. For all samples the medium was removed, and the flask/dish was flushed with 5 *ml* PBS using 10 *ml* pipettes. After removing the PBS, 2 *ml* TrypLE was added, and the flasks were placed in the incubator for ~4 minutes at 37 °C. MOC1 cells were especially adhesive when they settled on a dish/flask surface and required up to 10 minutes in the incubator to disassociate from the cell flasks/dishes. Using a 1 *ml* or 2 *ml* pipette the cells were suspended to single cells and added to tubes prefilled with 4 *ml* medium, DMEM/F12 for A549 cells, IMDM for MOC1 and MOC2 cells. These tubes were then centrifuged for 4 minutes at 200 g, the liquid above the cell pellets were aspirated and the cells were resuspended in 10 *ml* PBS.

In the next step each sample was split into two. For each sample an empty tube was filled with 5 *ml* PBS and 5 *ml* was added from a sample, subsequently 5 *ml* PBS was added back to the

original sample to make both portions 10 *ml*. All samples were centrifuged for 4 minutes at 200 g and aspirated.

After splitting, centrifuging and aspirating the samples, the primary antibody (PA) was added to the original samples. The primary antibody, Anti-Calreticulin antibody ab2907, rabbit polyclonal (Abcam, UK) attaches to the membrane bound calreticulin. The PA was kept in a freezer in aliquots of 2.25  $\mu$ l in Eppendorf tubes. PBS with 1% bovine serum albumin (BSA) was added to the Eppendorf tube with PA and subsequently distributed between the original samples. The other samples from the split would only receive PBS with BSA (1%) and all the samples were put on ice and incubated in dark at room temperature. Afterwards, the samples were washed in two rounds. 3 *ml* PBS was added to each sample and centrifuged for 4 minutes at 200 g. Subsequently, the supernatant was aspirated, and the cell pellet resuspended in 3 *ml* PBS for another round of centrifuging and aspiration for each sample. The samples were now ready for the secondary antibody (SA), Alexa Fluor 647 goat anti-rabbit IgG (H+L) (Abcam, UK) which attaches to the PA and acts as the fluorochrome, emitting detectable light signals during flow cytometry. The SA was kept in the fridge, prior to use it was diluted in PBS with 1% BSA and added to all samples. The samples were put on ice and incubated in dark for 30 minutes at room temperature. Afterwards, the samples were washed twice with PBS in the same manner as before. After washing the cells, each sample was suspended in 250 *ml* PBS. The samples were now ready for flow cytometry, while they were kept in a fridge at 4 °C.

Prior to flow cytometry we added 0.5  $\mu$ l of 1 *mg*/ $\mu$ l propidium iodide (PI) (Thermo Scientific, Germany) to a sample for live/dead staining. PI stains double stranded DNA if the cell membrane is leaking and can be detected by the FL2 or FL3 channels during flow cytometry. The cell suspension was filtered through filter paper into a 5 *ml* flow cytometry tube. Samples were placed on the sample injection port (SIP) and run through the flow cytometer for analysis.

### 3.7 Flow Cytometry Analysis

The flow cytometry analysis was performed on an Accuri C6 Flow cytometer (BD Biosciences, USA) connected to a computer, located in the department of Biological and Medical Physics, UiO, room KV350b. We used the software program “CFlow” on the computer connected to the flow cytometer for analysis and general use of the instrument.

### 3.7.1 Flow Cytometry channels

Table 3 shows the channels that were used during flow cytometry analysis for the specified fluorochromes. Channels FL2 or FL3 is used to distinguish between living and dead cells based on the PI solution that was added to the cells. To make sense out of the fluorescence intensity signals obtained from flow cytometry we need to correct for the background or innate signals that would be detected without fluorochromes. As mentioned in section 2.6, flow cytometry is based on relative measurements, from Eq. (29) we see that this is done by subtracting the signals from samples with primary antibody (PA) and secondary antibody (SA) with samples which only received SA. This removed signals caused by autofluorescence and unspecific binding of the SA and is the reason why samples were split in two during CRT assay.

Hence, FL4 is the channel that was used to measure fluorescence from membrane bound calreticulin antibodies based on the SA which attaches to the PA. For the first couple of experiments, we used the previous protocol which includes the FL1 channel for detection and separation of dyed control cells and irradiated cells.

Laser wavelength		Name	Substance	Channel
Excitation max (nm)	Emission max (nm)			
		Primary antibody (PA)	Anti-Calreticulin antibody (ab2907), rabbit polyclonal	
<b>651</b>	<b>667</b>	Secondary antibody (SA)	Alexa Fluor 647 goat anti rabbit IgG (H+L)	FL4
<b>536</b>	<b>617</b>	Live/dead staining	Propidium iodide (PI) solution	FL2, FL3
<b>493</b>	<b>518</b>	Barcoding	DyLight 488-NHS Ester Dye	FL1

*Table 3: The substances used and corresponding flow cytometry channels and light wavelengths responsible for excitation and emission with maximal intensity. FL1 channel is not used in new protocol as the newer experiments were performed without using dye on control cells.*

### 3.7.2 Flow cytometry CFlow Gating

#### Forward Scattered and Side Scattered Cells

Membrane-bound calreticulin was analyzed by using the CFlow program to gate and single out viable cells. Gating in this context means designating a set of events to analyze. We start by comparing the forward scattered signal (FSC) and side scattered signal (SSC) in a density plot. In Figure 30 we see an example one of the earlier experiments. Here we have gated most of the cells, 79.2% of all events, while avoiding cells with relatively high side scattering compared to forward scattering as these tend to be cells with broken membranes.

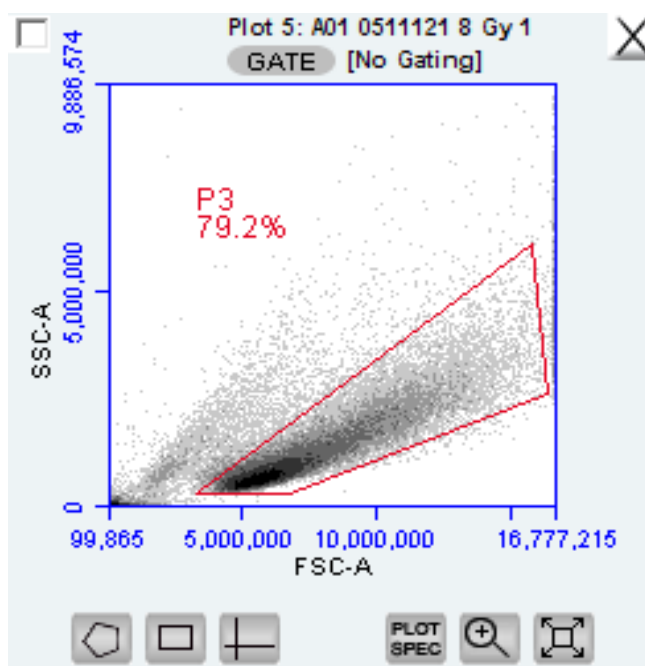


Figure 30: Gating of FSC area vs SSC area, density plots for 8 Gy A549 cells experiment 05.11.2021.

Next, we applied this general gating in a similar density plot where the y-axis represents the height of FSC instead of side scattering, as seen in Figure 31. This way we could further assure that we only analyze single cells. Cells outside this gating could be doublets or triplets which would misrepresent the fluorescence signal.

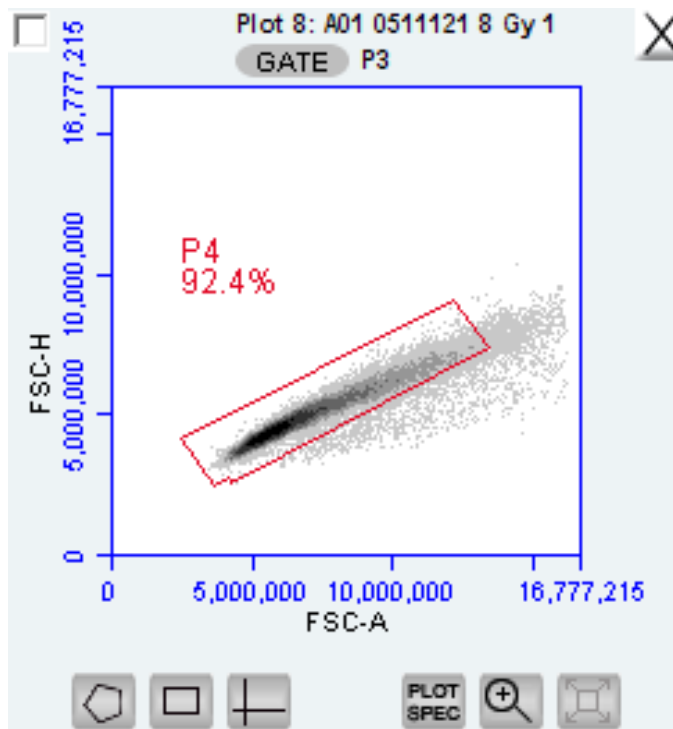


Figure 31: Gating of FSC area vs FSC height, density plot gated by P3 from Figure 30.

### Live/dead Staining and gating

Propidium iodide for live/dead staining can be seen in channel FL2 or F3. By applying the gating from the FSC and SSC plots to histograms showing the FL2 or FL3 channel we get something akin to Figure 32. Here we can separate between living cells with intact membranes from dead cells. As mentioned, PI stains only dead cells. An intact membrane will prevent the PI from entering the cell and binding to double stranded DNA. Therefore, in a sample containing cells with only intact membranes, the only apparent signal will be that of living, viable cells. In the case with Figure 32, we see only 1 peak which indicates that most of the cells were alive. This also indicates that the previous gating was well chosen and did not include dead cells.

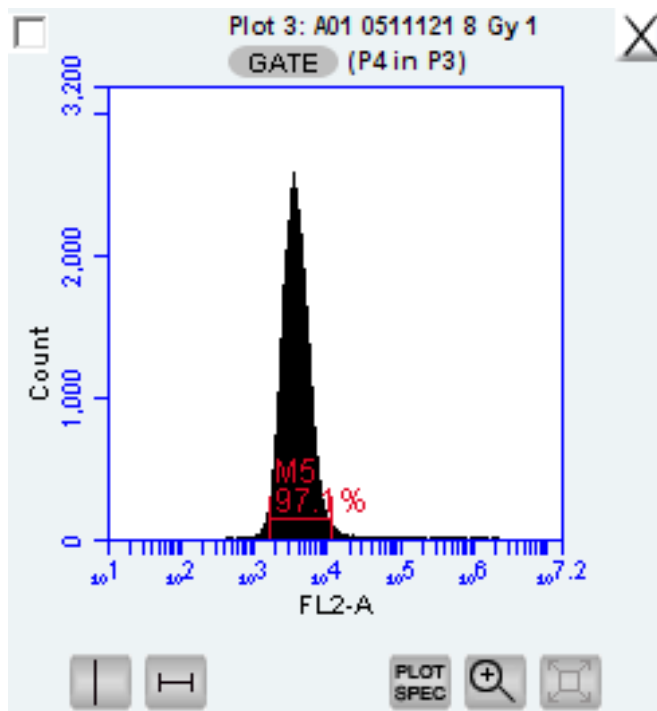


Figure 32: Histogram of FL2 channel, where PI is detected. Gated by P4 from Figure 31

### Gating DyLight Stained Cells

For the protocol using DyLight Alexa Flour 488 the next step was to look at channel FL1. As seen in Figure 33, here some of the problems of using DyLight stains became apparent. Ideally, we would see two clearly separated peaks/columns representing irradiated cells and control cells. Instead, in most if not all cases with experiments using stained control cells along with irradiated cells, we would find it difficult to get a clear distinction in the FL1 channel. Nonetheless, we tried to create two separate gates for the irradiated cells and the control cells.

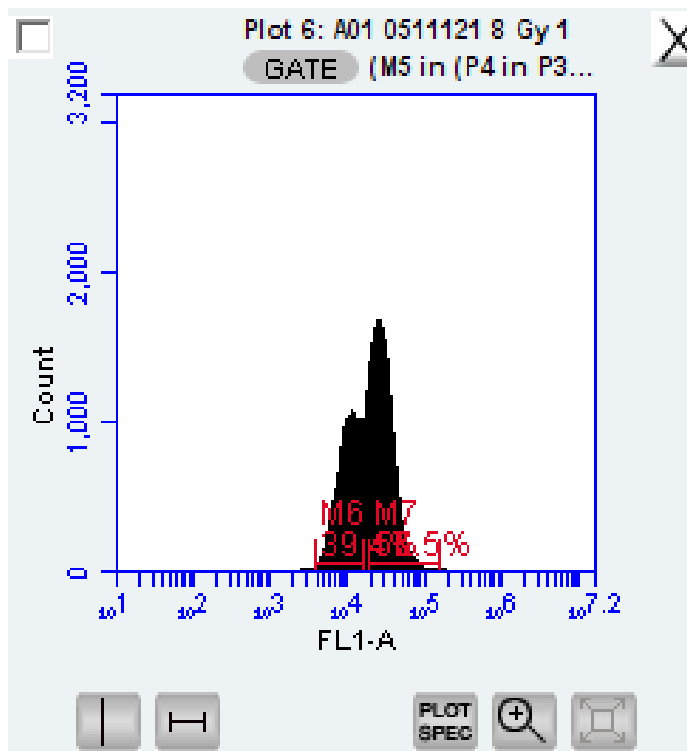


Figure 33: Histogram of FL1 channel, gated by M5 from Figure 32. We see the histograms of the irradiated and control cells are merged making it difficult to separate control and irradiated cells.

The last step involves applying the gating from the FL1 channel to the FL4 channel, which detects the secondary antibody fluorescence. When we had two peaks in the FL1 channel, we had to look at these separately, one in each plot. As seen in Figure 34 the left histogram is gated by M6 from Figure 33 while the right plot gated with M7, representing the irradiated cells and control cells, respectively.

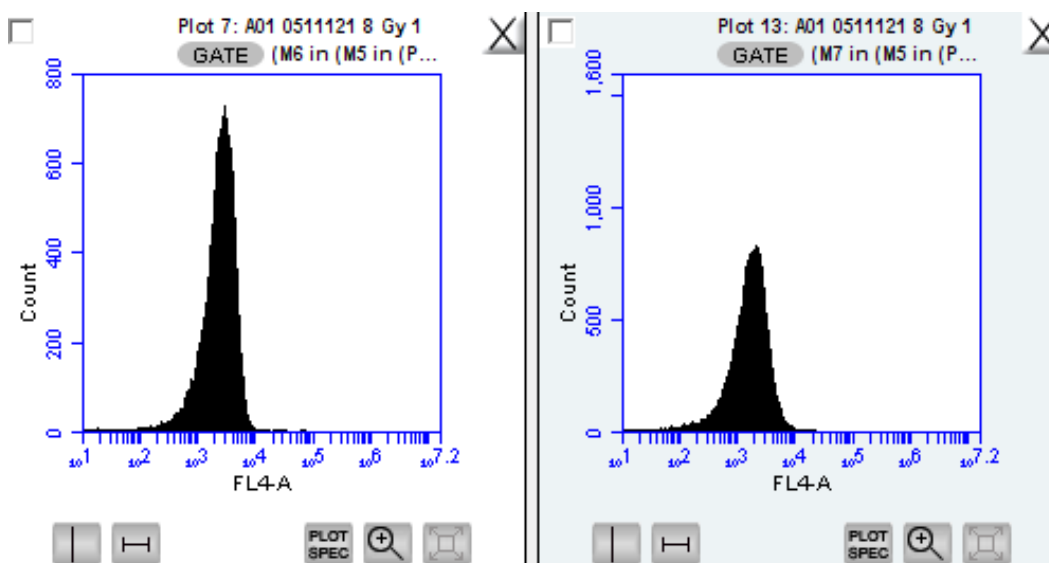


Figure 34: Histogram of FL4 channel. Left: Gated by irradiated cells (M6 from Figure 33). Right: Gated by control cells (M7 from Figure 33).

For the new assay protocol this process was simplified as we no longer used any DyLight. Figure 35 gives an overview of how the membrane bound calreticulin was gated and measured in this case.

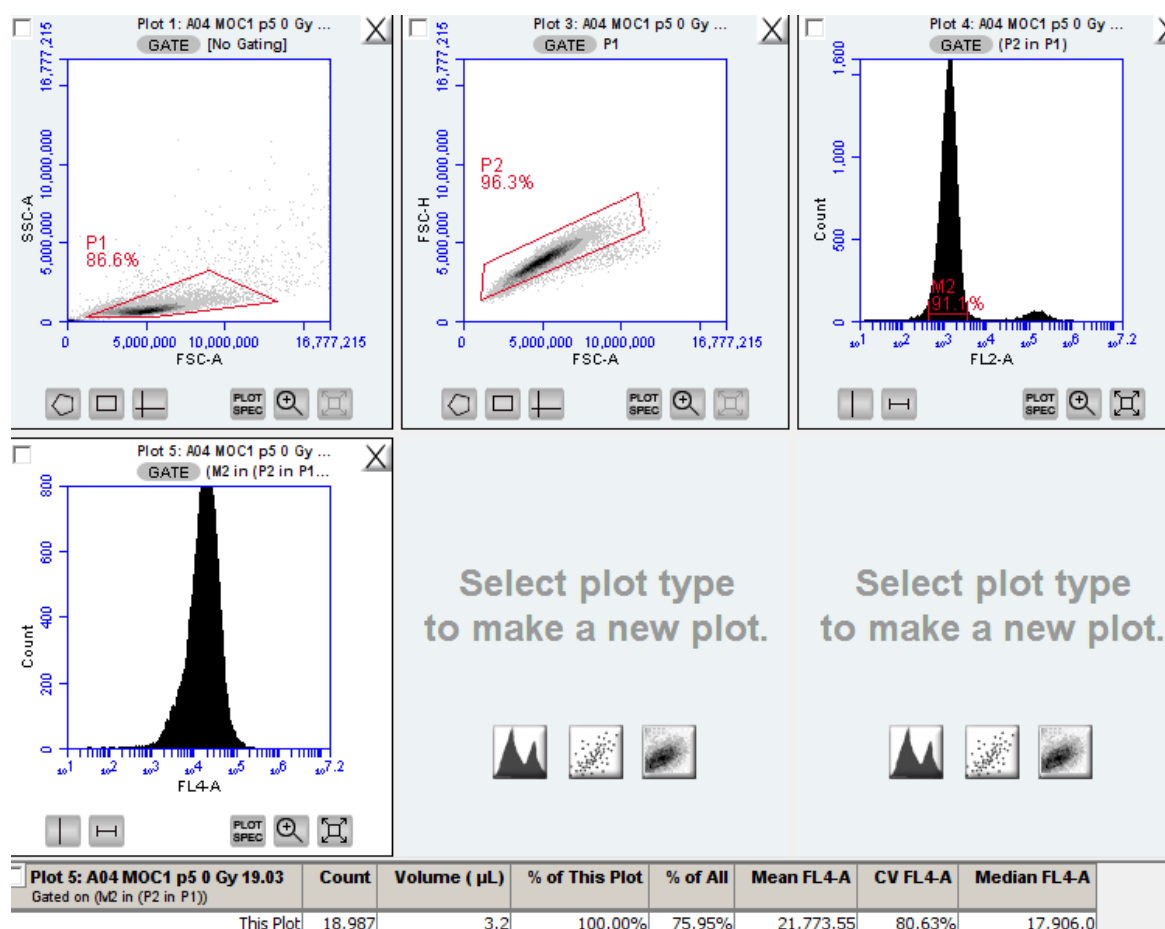


Figure 35: CFlow analysis and gating of MOC1 position 5, 4 Gy protons 19.03.

### 3.7.3 CFlow Data Statistical Significance and Student's T-test

To determine whether there was a statistical significance between a set of samples we used a Student's t-test. The t-test was performed in Microsoft excel and yields a P-(probability) value based on two sets of data, such as the median fluorescence intensity values. We considered P-value  $P < 0.05$  as statistically significant. Meaning, there is low probability that the results occurred due to chance.



## 4 Results

In this section we will present the results obtained during this thesis, while in section 5 the results will be discussed and analyzed.

Table 4 shows an overview of the calreticulin assay experiments, while Table 5 is a similar overview of the colony formation experiments that were performed during this thesis.

Date	Irradiation type – Dose [Gy]	Cell Line	Comment
15.10.2021	X-rays - 8	A549	Unable to distinguish control and irradiated sample
05.11.2021	X-rays - 8	A549	
24.11.2021	X-rays - 8	A549	
26.01.2022	X-rays	A549	Unusable data, cells were too damaged
03.02.2022	X-rays	A549	Unable to distinguish live and dead/damaged cells
04.02.2022	X-rays -2, 4, 6, 8	MOC1	Test experiment, too many samples, low cell viability
25.02.2022	X-rays -2, 4, 6, 8	MOC2	Test experiment, too many different dose samples, low cell viability
11.03.2022	X-rays – 6	MOC2	
17.03.2022	Protons, P1, P5 – 4	A549, MOC2	4 experiments
18.03.2022	Protons, P1, P5 – 8	A549, MOC2	4 experiments
19.03.2022	Protons, P1, P5 - 4	MOC1	2 experiments
20.03.2022	Protons, P1, P5– 4, 8	MOC1	2 experiments
31.03.2022	X-rays – 4, 8	MOC1	2 experiments
07.04.2022	X-rays – 4, 8	MOC2	2 experiments

Table 4: Overview of all calreticulin experiments performed during thesis (2021-2022). Experiments highlighted in red were excluded or did not yield any results due to various reasons.

Date	Doses [Gy]	Comment
07.09.2021	1, 2, 5	
25.10.2021	1, 2, 5	
30.11.2021	1, 2, 5, 7.5, 10	Problems with LAF-bench, no cells in flasks after fixation
7.12.2021	1, 2, 5, 7.5, 10	No cells were found after fixation, most likely caused by medium without FBS
14.12.2021	1, 2, 5, 7.5, 10	No cells were found after fixation, most likely caused by medium without FBS
18.01.2022	1, 2, 5, 7.5, 10	
20.01.2022	1, 2, 5, 7.5, 10	Very few cells/colonies after fixation, problems with seeding
08.02.2022	1, 2, 5, 7.5, 10	Very few cells/colonies after fixation, problems with seeding
11.02.2022	1, 2, 5, 7.5, 10	
21.02.2022	1, 2, 5, 7.5, 10	

Table 5: Overview of colony formation assay experiments performed during master thesis (2021-2022). Experiments highlighted in red were excluded or did not yield any results due to various reasons

The subject of interest for this thesis was to measure the effects of different kinds of irradiation on cancer cell surface expression of calreticulin, which is related to immunogenic signaling. All doses were given in a single fraction and the focus was mainly on the effects of 4 Gy and 8 Gy doses. Each experiment, after protocol development included 1 control and 3 samples receiving the same dose. Earlier experiments or test experiments could have more samples or follow a different protocol. In addition, we have made cell survival curves and LQ-model fits for MOC1 and MOC2 to compare the radiosensitivity of the two cell lines.

## 4.1 Colony Survival Experiment Results

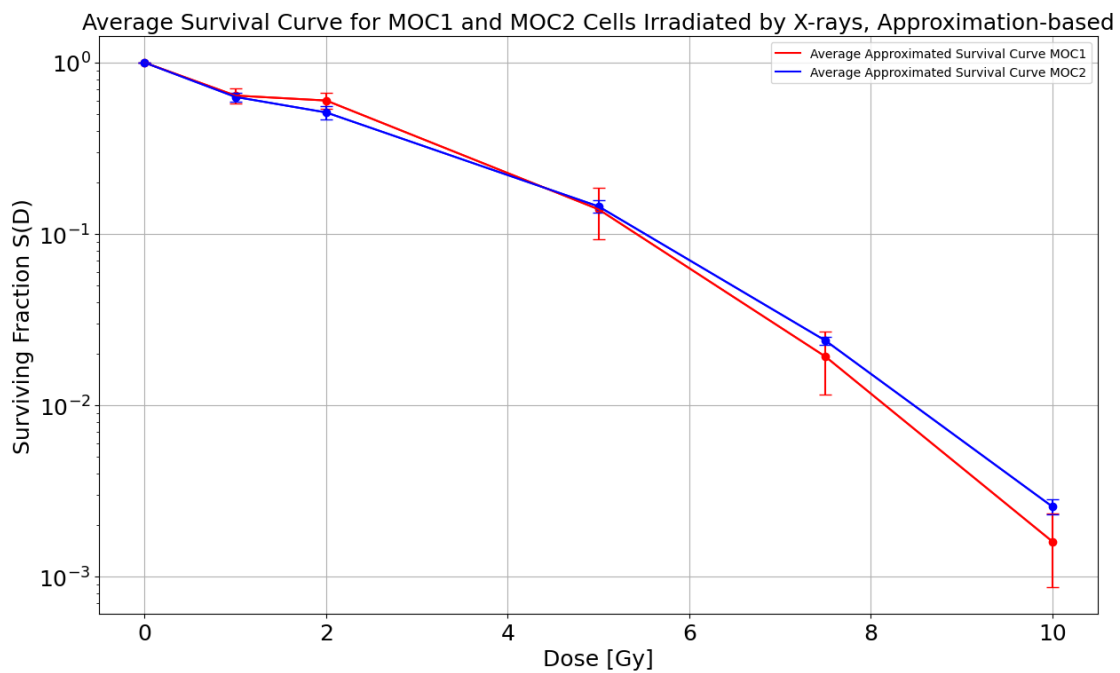


Figure 36: Plot showing the approximated average survival curves based on Eq. (27) and the average results of all CFA experiments. The x-axis shows dose ( $D$ ) in Gy while the y-axis is the surviving fraction  $S(D)$  on a logarithmic scale. The MOC1 cell survival curve (in red) was found by the author of this thesis, while the MOC2 (in blue) data was provided by Frida Larsen. Data points are mean values from 4-5 independent experiments. Error bars indicate the standard error of mean between experiments.

The results for the clonogenic experiments can be seen above in Figure 36, which is based on Eq. (27), assuming CFUs containing only singlets and doublets, but calculating a value for multiplicity ( $M$ ) including CFUs with more than two cells, an approximation used by previous master students. The raw data for these experiments are found in tables in appendix 4, while the equations and methods of survival calculation are found in section 3.4.2. In Figure 36 we notice how similar the dose responses for MOC1 and MOC2 seem, especially for 5 Gy or higher doses. The earlier experiments were done with samples receiving 1, 2 and 5 Gy. To

find how the survival curves behaves at higher doses 7.5 and 10 Gy samples were included for later experiments. The data indicates that MOC1 and MOC2 react somewhat similarly to ionizing radiation in terms of cell survival measured as the ability to divide.

Because of the high multiplicity and high number of CFUs with more than two cells for MOC2 cells, correction for multiplicity was also done using the exact solution for the surviving fraction. In Figure 37 we have omitted the first two experiments with MOC1 and the first experiment with MOC2 and plotted the exact (Eq. (26)) and approximated (Eq. (27)) surviving fraction. These removed experiments were more practice and learning oriented and the seeding and colony counting was not optimal due to lack of experience. We noticed a drastic difference in MOC2 survival curves between the approximated and exact solution in Figure 37, therefore we continued our analysis with the exact multiplicity correction for both MOC1 and MOC2. The approximated and exact curves for MOC1 cells are nearly identical due to the low number of triplets or higher order CFUs with MOC1 cells.

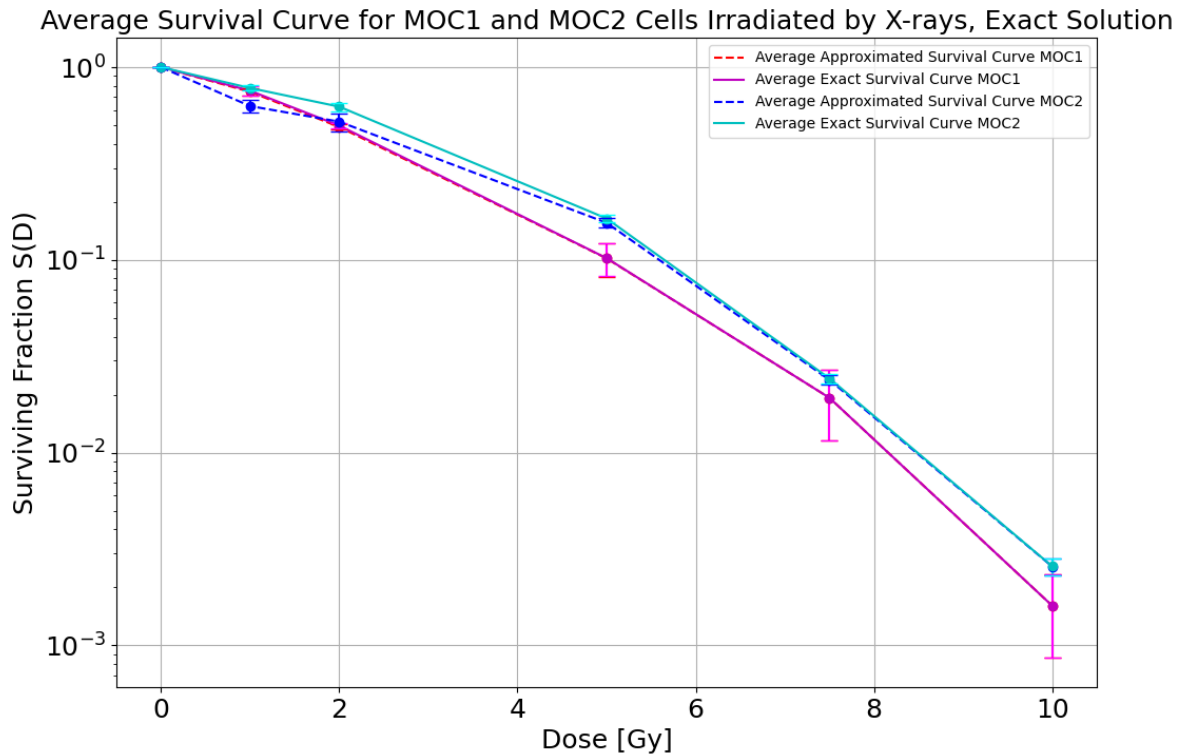


Figure 37: Plot showing the exact and approximated average survival curves based on multiplicity corrected surviving fractions shown in Eq. (26) and Eq. (27), respectively. The x-axis shows dose ( $D$ ) in Gy while the y-axis is the surviving fraction  $S(D)$  on a logarithmic scale. Data points are mean values from 3-4 independent experiments. Error bars indicate the standard error of mean between experiments. The magenta curve shows the average exact survival curve, while the overlapping dashed red curve is the approximated average survival curve for MOC1 cells. The cyan curve shows

the average exact survival curve, and the dashed blue curve shows the approximated average survival curve for MOC2 cells.

In Figure 38 we have used the data points in Figure 37 to create LQ-model curve fits for the MOC1 and MOC2 average data. The curve fits were made using python programming and the SciPy.Optimize.curve\_fit function. Errors for  $\alpha$  and  $\beta$  are based on the square root of the diagonal elements in the covariance matrix from the curve fit function. Error in  $\alpha/\beta$  is based on error propagation from  $\alpha$  and  $\beta$ .

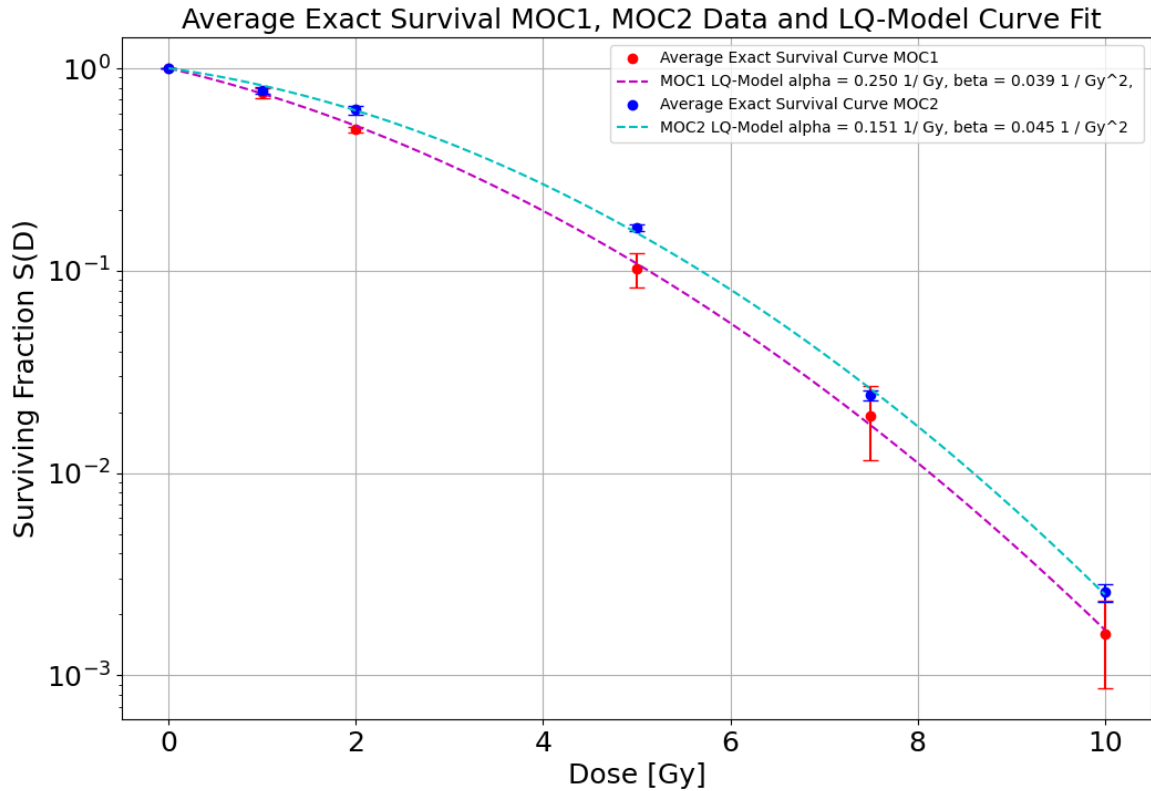
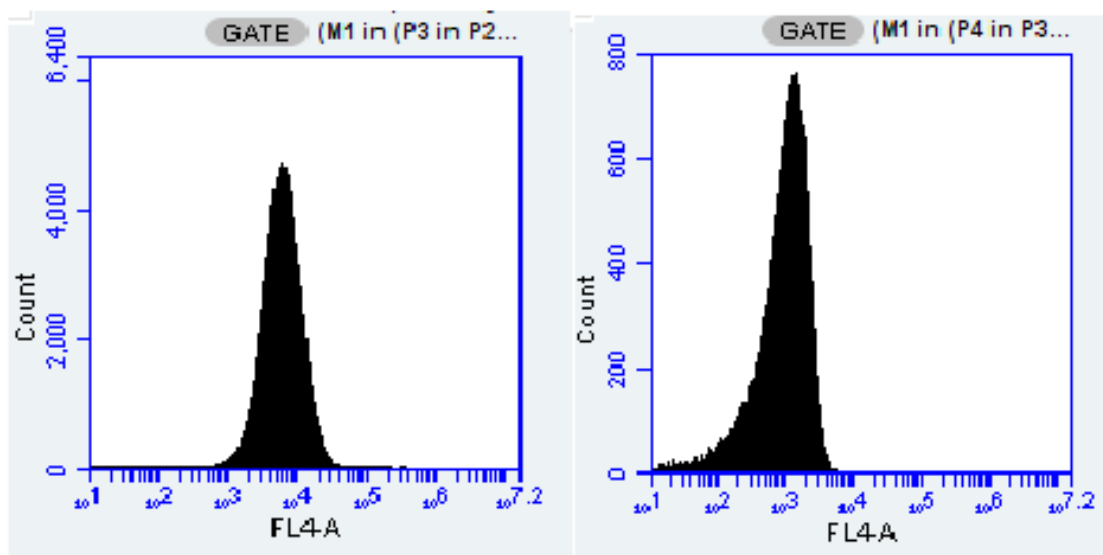


Figure 38: Plot showing LQ-model curve fits based on the average exact survival data seen in Figure 37 for MOC1 and MOC2 cells. The x-axis shows dose (D) in Gy while the y-axis is the surviving fraction  $S(D)$  on a logarithmic scale. Error bars indicate the standard error of mean between experiments. MOC1 LQ curve fit (dashed magenta curve) parameters:  $\alpha = 0.25 \pm 0.02 \text{ Gy}^{-1}$ ,  $\beta = 0.039 \pm 0.002 \text{ Gy}^{-2}$ ,  $\frac{\alpha}{\beta} = 6.4 \pm 0.7 \text{ Gy}$ . MOC2 LQ curve fit (dashed cyan curve) parameters:  $\alpha = 0.15 \pm 0.02 \text{ Gy}^{-1}$ ,  $\beta = 0.0045 \pm 0.02 \text{ Gy}^{-2}$ ,  $\frac{\alpha}{\beta} = 3.4 \pm 0.4 \text{ Gy}$ .

## 4.2 Membrane Bound Calreticulin After Calreticulin Assay

Results in this and following sections will be shown in terms of the median fluorescence intensity values found in the FL4 channel histograms. This is due to the skewed or asymmetric nature of the histograms making the median a better estimate for the intensity than the mean values, which are better suited for normal distributions. See Figure 39 showing two examples of histograms in the FL4 channel, one looks somewhat symmetrical, and the other is skewed to the left. The raw data used to make the plots and calculate the fluorescence ratios based on Eq. (29) can be found in Appendix 1, while the calculated ratios and standard errors of mean (SEM) used in the plots can be found in Appendix 2. These appendices contain both mean and median values for each experiment. The mean of the median intensity values for the SA-corrected controls (X-rays and protons) are shown in Figure 48.



*Figure 39: FL4 channel histograms in CFlow after flow cytometry. Left: A549 irradiated with 4 Gy in position 1, 17.03.2022. Right: A549 irradiated with 6 Gy X-rays, 15.10.21.*

### 4.2.1 X-ray Irradiation Results

The number of cells in the samples from 4 Gy X-ray irradiation for the A549 cell line were very low. The most reliable results for A549 cells were therefore for 8 Gy and these can be seen along with the MOC1 and MOC2 results summarized for 4 Gy and 8 Gy in Figure 40.

The bar charts in Figure 41 and Figure 42 show the average of the median fluorescence intensity values for samples receiving (PA + SA) and SA, respectively for all X-ray experiments. The error bars indicate the standard error in the mean for all experiments.

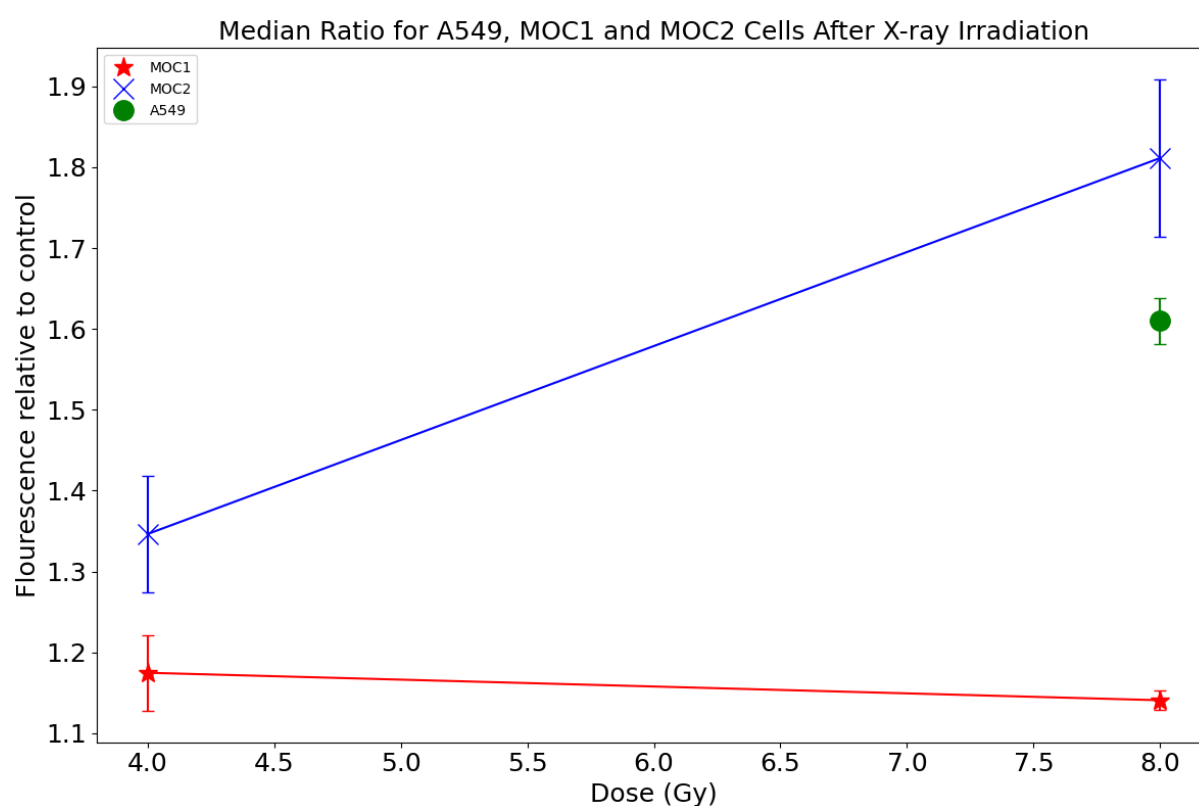


Figure 40: The average median fluorescence intensity relative to control cells, plotted as a function of the dose received by X-ray irradiated samples. Error bars indicate the standard error of mean (SEM)

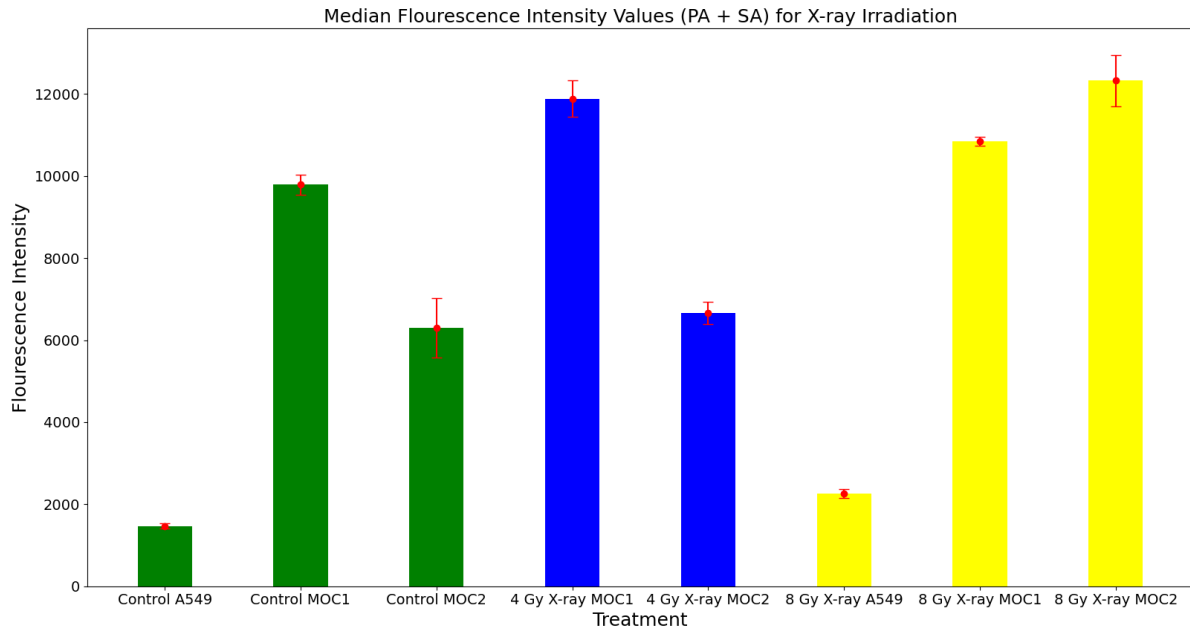


Figure 41: Bar plots of the average median intensity values for samples receiving PA and SA, X-ray experiments. Error bars indicate the standard error of mean (SEM).

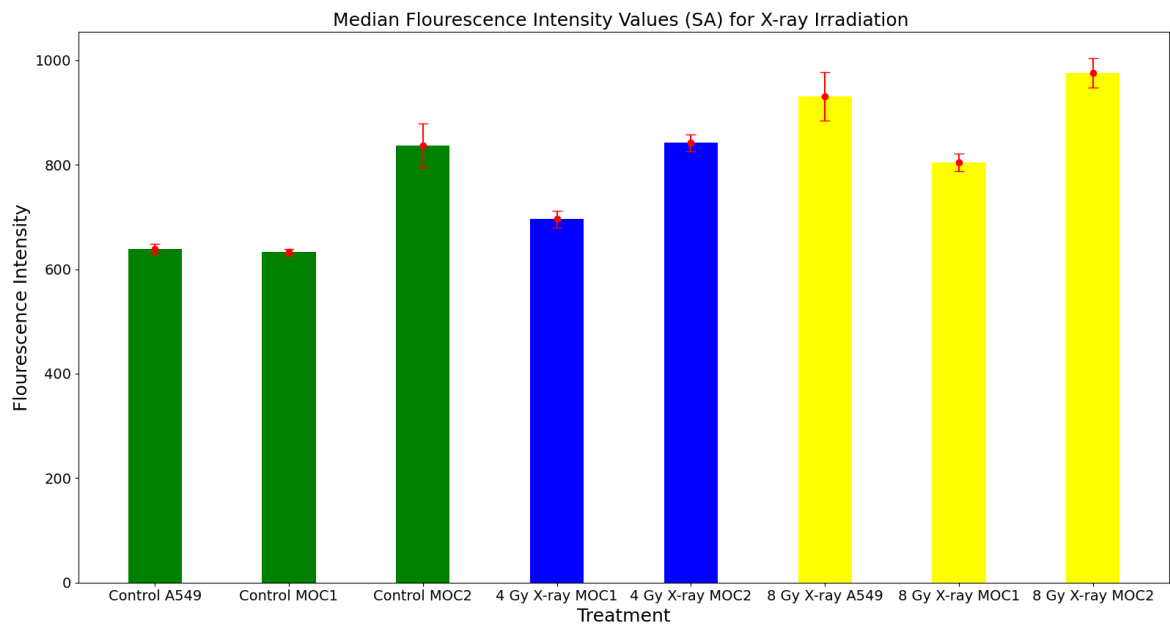


Figure 42: Bar plots of the average median intensity values for samples receiving only SA, X-ray experiments. Error bars indicate the standard error of mean (SEM).



## 4.2.2 Proton Irradiation Results

All calreticulin assay experiments with protons were performed using the new protocol, without DyLight. Figure 43 gives an overview of the results for proton irradiated relative calreticulin levels after irradiation. Figure 44 and Figure 45 show the average of the median fluorescence intensity values for samples receiving (PA + SA) and SA, respectively for 4 Gy and controls. Figure 46 and Figure 47 are similar bar plots for 8 Gy and controls.

The irradiations were done in two different positions in the Bragg peak, position 1 (P1) and position 5 (P5) in Figure 28. It should be noted that for proton experiments the dosimetry was performed several times between irradiation of samples. It was later recognized that for some samples the positions found were not always accurate in terms of P1 and P5. In addition, there is the human error element, a fellow master student was manually stopping the beam by pressing a button, occasionally giving more or less than the intended dose. However, the exact dose was recorded for each sample. The variation was used together with the uncertainty in the position in the Bragg peak to calculate an estimation of the combined error in dose to about 10%. In other words, for protons the doses given should be thought of as  $4.0 \pm 0.4$  Gy and  $8.0 \pm 0.8$  Gy and can be seen as the error bars along the x-axis in Figure 43.

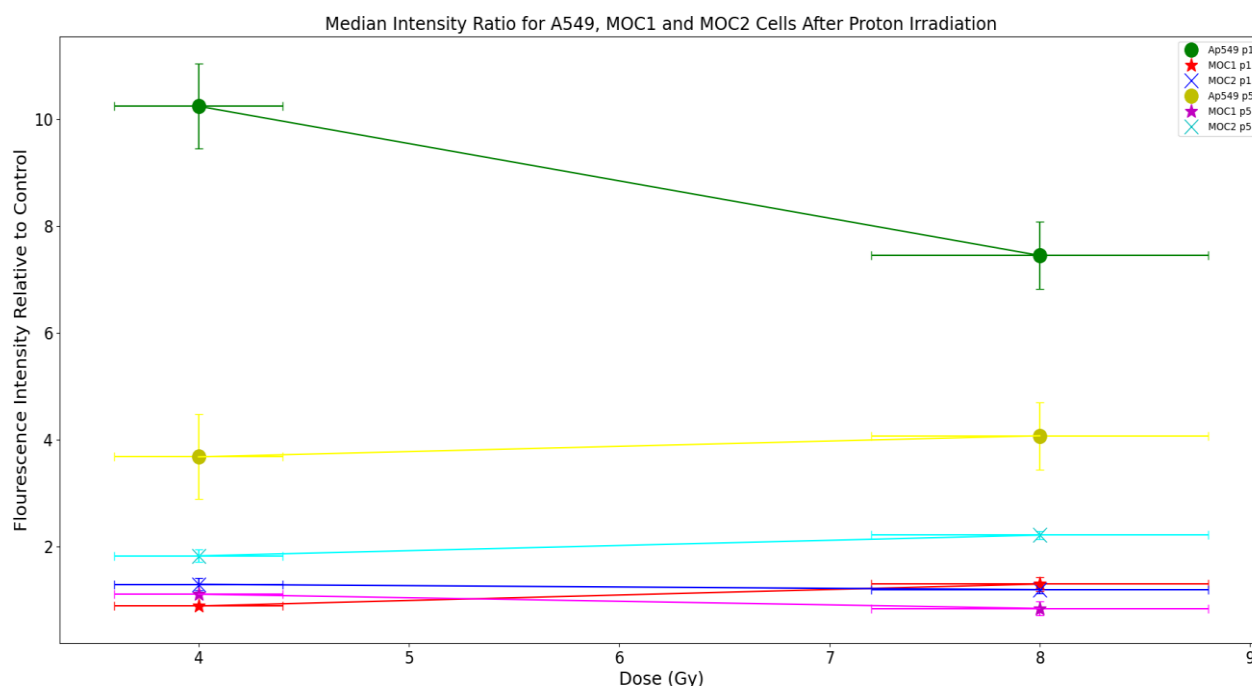


Figure 43: The median fluorescence intensity relative to control cells plotted as a function of the dose received by proton irradiated samples. X-axis error bars indicate the estimation of error in dose due to fluctuations in dose and position in Bragg peak, y-axis error bars indicate the standard error of mean in calculated ratios (SEM)

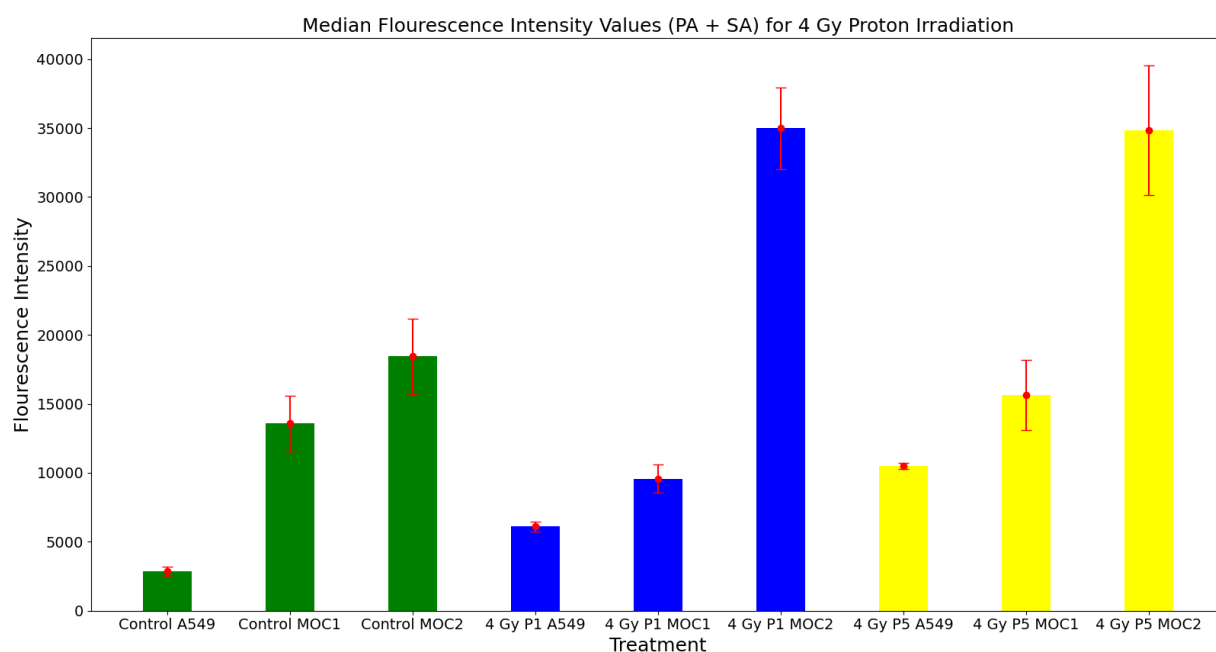


Figure 44: Bar plots of the average median intensity values for samples receiving PA and SA, 4 Gy proton experiments. Error bars indicate the standard error of mean (SEM).

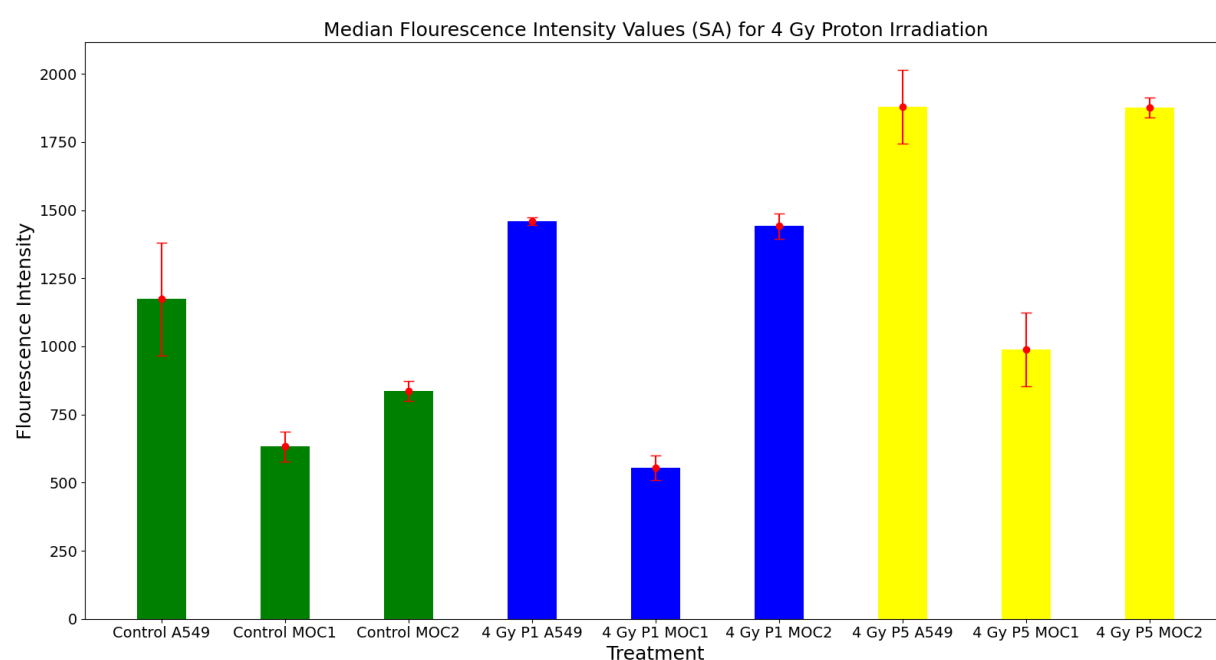


Figure 45: Bar plots of the average median intensity values for samples receiving SA, 4 Gy proton experiments. Error bars indicate the standard error of mean (SEM).

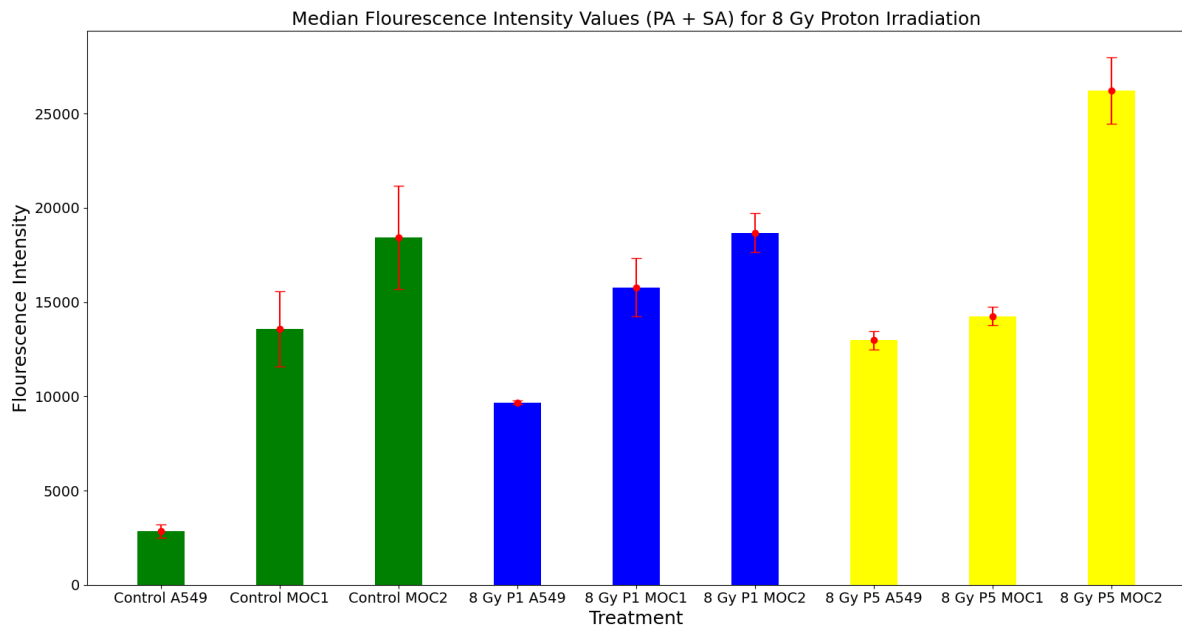


Figure 46: Bar plots of the average median intensity values for samples receiving PA and SA, 8 Gy proton experiments. Error bars indicate the standard error of mean (SEM).

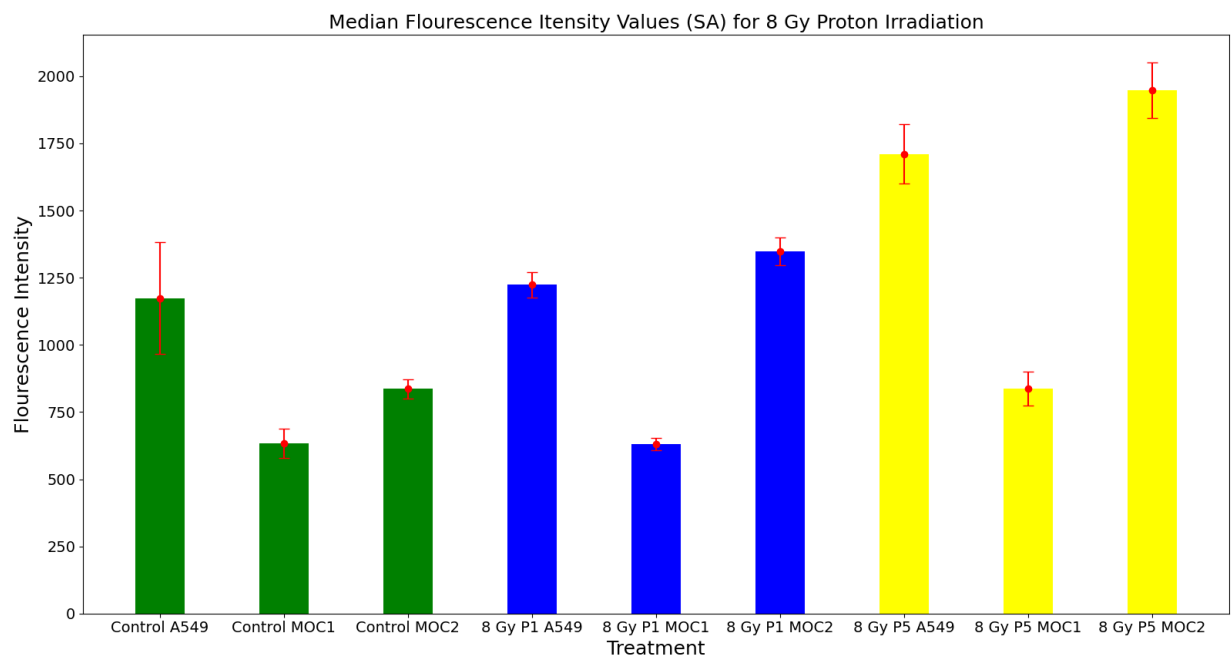


Figure 47: Bar plots of the average median intensity values for samples receiving SA, 8 Gy proton experiments. Error bars indicate the standard error of mean (SEM).

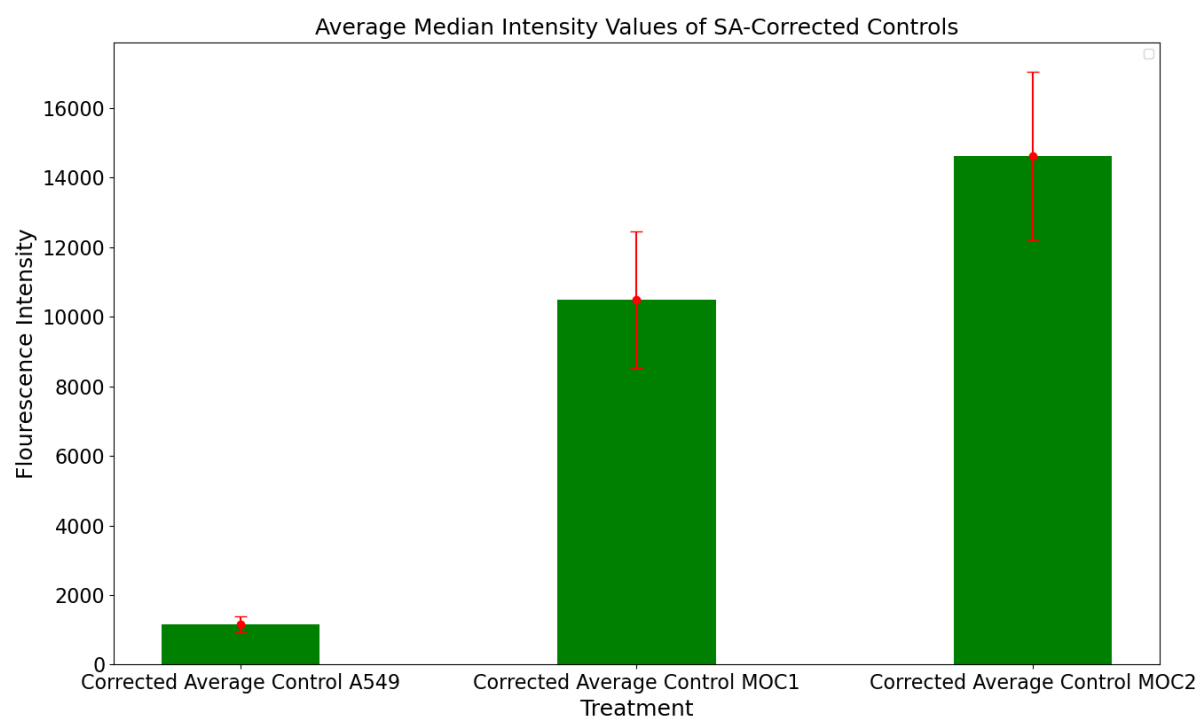


Figure 48: Bar plots of total average (X-rays and protons) median intensity values for SA-corrected control samples. Errors are shown as red error bars, indicating SEM.

## 5 Discussion and Analysis

### 5.1 MOC1 and MOC2 Survival

Figure 37 show survival curves for MOC1 and MOC2 cell lines. These cell lines are relatively new and most of the research on them are performed in in vivo as opposed to in vitro which we have done. Jin et al. performed clonogenic assays using chemotherapy with anti-human epidermal growth factor receptor (huEGFR), cetuximab, combined with 8 Gy radiotherapy in vitro (Jin et al., 2021). They claim that cetuximab did not affect the radiosensitivity of MOC1 and MOC2 cells. We can therefore make a rough comparison between their results for 8 Gy with our results for 7.5 Gy. Using Figure 37 which is based on the exact solution a closer look, we see that the surviving fraction for 7.5 Gy is  $(1.9 \pm 0.8)\%$  for MOC1 and  $(2.4 \pm 0.1)\%$ , for MOC2. Meanwhile, Jin et al.'s results show a surviving fraction closer to 5% for 8 Gy irradiated MOC1 and 8 % for MOC2 cells. These values are higher than ours but more importantly, they show the same pattern, MOC1 is more radiosensitive than MOC2.

In Figure 38 we see an LQ-model curve fit for MOC1 and MOC2 cells based on the exact solution using Eq. (26). Based on these curves we see that:  $\alpha = 0.25 \pm 0.02 \text{ Gy}^{-1}$  and  $\beta = 0.039 \pm 0.002 \text{ Gy}^{-1}$ , meaning a ratio  $\frac{\alpha}{\beta} = 6.4 \pm 0.7 \text{ Gy}$  for MOC1, while  $\alpha = 0.15 \pm 0.2 \text{ Gy}^{-1}$  and  $\beta = 0.045 \pm 0.002 \text{ Gy}^{-2}$ , yielding a ratio  $\frac{\alpha}{\beta} = 3.4 \pm 0.4 \text{ Gy}$  for MOC2. We see that MOC1 cells can be classified as early responding tissue while MOC2 is closer to late responding tissue. We can compare this to the results from similar clonogenic assays with X-ray irradiation of A549 cells performed by Skeie (2021):  $\alpha = 0.40 \pm 0.05 \text{ Gy}^{-1}$ ,  $\beta = 0.031 \pm 0.005 \text{ Gy}^{-2}$ ,  $\frac{\alpha}{\beta} = 12.90 \pm 0.05 \text{ Gy}$ . We see that A549 cells have high  $\alpha/\beta$  ratio, typical for early responding cancer tissue. The surviving fraction for A549 cells after 7.5 Gy can be calculated by using the  $\alpha$  and  $\beta$  values found by Skeie (2021) to be  $(0.9 \pm 0.2)\%$  which makes them more radiosensitive than the MOC cell lines.

By working with MOC1 and MOC2 we also noticed some practical differences between these two cell lines. In the methods section, we mentioned that MOC1 cells adhere strongly to the bottom of the cell flasks, making it difficult to disassociate these cells. On the other hand, MOC2 cells have strong cell to cell adhesion but are easy to disassociate from the cell flask. In addition, Frida Larsen mentioned that the trypsin for the later experiments was

degraded/outdated. This is also reflected in the multiplicity values found for CFA experiments, for MOC1 the average multiplicity was  $M_{MOC1} = 1.35 \pm 0.02$ . The MOC2 data we used which was provided by Frida Larsen had an average multiplicity of  $M_{MOC2} = 1.93 \pm 0.21$ . The multiplicity corrected surviving fraction for MOC2 should be calculated using Eq. (26), rather than Eq. (27) which assumes only singlets and doublets. This is what we have done in Figure 37 and we see a clear difference between the approximation-based and exact multiplicity corrected surviving fraction for MOC2. MOC1 experiments yielded few triplets or higher order CFUs, which explains why the exact and approximation-based solutions are nearly identical and difficult to distinguish in Figure 37.

If doublets or triplets etc. were analyzed during flow cytometer the signals would not represent the calreticulin expression of a single cell. However, we will assume that this high cell-to-cell adhesion of the MOC2 cells had a negligible effect on the CRT assay experiments as opposed to the CFA experiments because of two reasons. Firstly, the assays are different, CRT assay being a longer assay with multiple washing, aspirating and centrifuging cycles. It is possible that this will give a better single cell suspension at the end of the assay. Secondly and most importantly, the flow cytometer software allowed us to gate out single cells based on the FSC area and FSC height signals (see Figure 31).

## 5.2 Calreticulin Expression on Cell Membrane

The purpose of calreticulin (CRT) assay was to measure calreticulin that is translocated to the cell surface as a result of cells succumbing to ICD after being exposed to ionizing radiation. Translocated calreticulin acts as a pro-phagocytic signal and is therefore a way of measuring immunogenic signaling by irradiation. As described in 3.6, each sample was split in two, one incubated with both primary and secondary antibody, the other incubated only with secondary antibody. This was done to be able to correct the signal for autofluorescence and unspecific binding of the secondary antibody. The importance of this is emphasized by the clear dose response in the samples without primary antibody shown in Figure 42, Figure 45 and Figure 47. In these bar plots we notice two things. 1. The median intensity values are relatively similar between cell lines (as opposed to samples receiving PA and SA) and 2. The median intensity values increase with dose. The second point has already been categorized by Ruud (2020) and is due to an increase in autofluorescence with irradiation dose. Without the correction for these artifacts, we would have come to the wrong conclusion that all cell lines have a dose response as seen in figures Figure 41, Figure 44 and Figure 46 with the

uncorrected data. To compare the baseline surface exposed calreticulin levels we have Figure 48 which represents the mean of all the corrected control sample's median intensities for each cell line.

### 5.2.1 Differences in Cell Lines

#### **CRT Expression Before and After Irradiation**

Looking at the results for X-rays, the effect of radiation on calreticulin expression varies from cell line to cell line. Comparatively speaking, A549 cells have a low level of calreticulin expression in general. This can be seen in the bar plots in section 4.2 where A549 is the cell line with the lowest median intensity value for all doses and irradiation types. On the other hand, A549 has the clearest increase in calreticulin levels after irradiation. Irradiated samples show a clear dose dependent, radiation induced immunogenic signaling for A549 cells after X-ray irradiation.

MOC1 calreticulin expression seems to be unaffected by irradiation dose or irradiation type. Although unirradiated MOC1 cells are highly immunogenic compared to A549 cells as seen from the bar plots in section 4.2, there is practically no difference in MOC1 calreticulin levels after irradiation. This is clearly seen in Figure 40 for X-rays and Figure 43 for protons, the relative fluorescence intensity is a flat, horizontal line between 4 and 8 Gy, and the ratios are close to 1 and occasionally lower than 1 for both 4 Gy and 8 Gy. This trend for MOC1 cells can be seen for X-rays and proton alike.

MOC2 cells showed the highest calreticulin expression before and after irradiation. Looking at Figure 41, Figure 44 and Figure 46 we can tell that MOC2 cells have the highest fluorescence intensity out of the three cell lines, especially for irradiated samples. This indicates a clear dose dependance on CRT expression for MOC2 cells. However, for some reason we saw no increase related to dose in P1. We will discuss this further in the next subsection.

#### **The Effects of LET on Different Cell Lines**

The most significant effects of LET on membrane bound calreticulin levels can be seen for A549 cells. The proton experiments with A549 cells yielded larger ratios than X-rays. Comparing the ratios for 8 Gy irradiated with control A549 cells, P1 has a 4.35 times higher signal than X-ray irradiated samples ( $P_{X,P1} = 0.02$ ), while P5 has a 2.23 times higher signal ( $P = 0.002$ ). We also notice in Figure 43 that the ratio for 4 Gy P1 A549 cells is drastically

higher than 8 Gy P1 A549 cells ( $10.6 \pm 0.8$  for 4 Gy and  $6.96 \pm 0.63$  for 8 Gy). However, the control sample values for both 4 Gy P1 and 8 Gy P1 irradiated cells are for some reason very low, especially after correcting for autofluorescence and unspecific binding. In fact, if we used the control sample values for 4 Gy P5 instead of 4 Gy P1 controls we get an average ratio of  $2.07 \pm 0.15$  and  $3.61 \pm 0.31$  for 4 Gy P1 and 8 Gy P1, respectively. Meanwhile for P5 the ratio is relatively unchanged from 4 Gy to 8 Gy ( $3.64 \pm 0.07$  for 4 Gy and  $3.57 \pm 0.21$  for 8 Gy), although there is no statistical significance between 8 Gy P1 and 8 Gy P5 ( $P_{P1,P5} = 0.06$ ). At first glance this seems to be the opposite of what we expected, as P1 is supposed to have lower LET ( $\sim 10 \text{ KeV}/\mu\text{m}$ ) than P5 ( $\sim 40 \text{ KeV}/\mu\text{m}$ ), meaning higher biological effect for P5. However, our group has previously found that increasing the dose beyond 8 Gy for X-rays lead to a decrease in calreticulin fluorescence. Calreticulin signaling is induced by immunogenic cell death, so it is possible that when the dose or LET increases above a certain threshold, the damages become so complex that other cell death mechanisms take over. It is also possible that there will be a higher effect for position 5 below 4 Gy. This should be investigated in future experiments.

MOC1 cells seem unaffected by neither dose or LET and there is little to no effect caused by irradiation on immunogenic signaling for MOC1 cells, at least in terms of calreticulin expression. This however does not mean that MOC1 is not immunogenic. On the contrary, MOC1 cells are the highly immunogenic without irradiation as seen by the bar plots Figure 41, Figure 44 and Figure 46. The bars representing the MOC1 cells is in most cases considerably taller than A549, but shorter than MOC2. According to Cash et al. MOC1 is very immunogenic while MOC2 is moderately immunogenic (Cash et al., 2015). It is possible that MOC1 is more immunogenic in terms of other DAMPs such as ATP or HMGB1 or pathways e.g. the so-called cGAS-STING pathway, which activates the immune system.

MOC2 cells also had an increase in the relative fluorescence based on LET. For X-ray irradiation, the fluorescence ratio between the control and the irradiated samples for MOC2 is even higher than A549. For MOC2 irradiated by protons however, position 1 yielded lower a fluorescence ratio than X-rays for 8 Gy dose, although this is not statistically significant ( $P_{X,P1} = 0.1$ ). More specifically, the fluorescence ratio for MOC2 cells is  $1.81 \pm 0.09$  for X-rays, and  $1.19 \pm 0.08$  or  $2.21 \pm 0.15$  for 8 Gy for protons in P1 and P5, respectively. There is barely statistical significance between 8 Gy P1 and 8 Gy P5 ( $P_{P1,P5} = 0.05$ ) and



there is a statistical significance between X-ray samples and P5 samples  $P_{X,P5} = 0.03$ . For P1 there was a decrease in relative fluorescence between 4 Gy and 8 Gy. For P5 however, there is a clear, statistically significant increase in relative fluorescence both for 4 Gy and 8 Gy. This indicates that there is a dose and LET dependence in immunogenic signaling for MOC2 cells, albeit less so than A549 cells.

It is interesting to see such a big difference between MOC1 and MOC2 cells before and after irradiation. Based on Jin et al.'s and our results MOC1 is more radiosensitive than MOC2 (Jin et al., 2021). MOC2 is clearly more immunogenic in terms of surface exposed calreticulin as seen in Figure 48. On the other hand, MOC1 has high levels of membrane bound calreticulin that do not change with radiation. A factor that can influence the calreticulin signaling in different cell lines is the ability or proneness to immunogenic cell death. As mentioned above, it is possible that very complex or very high numbers of DNA damages induce different cell death mechanisms such as necrotic cell death without immunogenic signaling. Even though A549 cells are even more radiosensitive than MOC1 cells and have a strong CRT response to radiation, the induction of different cell death mechanisms may be different for different cell types. The cell survival based on the LQ-model curve fits in Figure 38 is  $\sim 20\%$  and  $\sim 26\%$  for 4 Gy and  $\sim 1\%$  and  $\sim 2\%$  for 8 Gy irradiated MOC1 and MOC2 cells, respectively. These differences are not large enough to explain the differences in CRT expression between MOC1 and MOC2 in Figure 41, Figure 44 and Figure 46. MOC1 being more radiosensitive might be more prone to other death mechanisms than ICD, which is not reflected in the difference in cell survival alone. Another factor could be that the surface of MOC1 is saturated with CRT and the CRT levels cannot be enhanced by radiation. In other words, MOC1 already has close to the maximum obtainable calreticulin levels on the cell membrane, while the values for MOC2 are high but can be increased further. CRT assay with MOC1 could be performed after irradiation with lower doses to investigate further.

### 5.2.2 Comparing Our Results

The results with A549 cells can be compared with the previous master student Ruud's results for X-ray irradiated A549 cells (Ruud, 2020). The general trend for A549 cells irradiated in one fraction seems to be a slight increase or a plateau in relative fluorescence from 2 Gy to 6 Gy, a sharp increase from 6 Gy to 8 Gy and a sharp decrease from 8 Gy to 12 Gy. A similar

pattern was seen for two fractions, but for higher total doses. Our results for 4 Gy and 8 Gy seem to be in the region where there is either a small or sharp increase in relative fluorescence, except for P1 protons, where we see a sharp decrease from 4 Gy to 8 Gy. As discussed above, this could be caused by questionable control samples. However, it could also be due to a shift in the threshold for the decrease in calreticulin signal for proton compared to X-rays due to the difference in LET ( $\sim 10 \text{ keV}/\mu\text{m}$  in front of the Bragg peak compared to  $\sim 1.1 \text{ keV}/\mu\text{m}$  for 220 kV X-rays).

For 8 Gy we see that Ruud has a median relative fluorescence of  $2.11 \pm 0.12$  for one fraction and  $1.56 \pm 0.02$  for two fractions (4 + 4) Gy. The result we have for 8 Gy given as one fraction is  $1.60 \pm 0.03$ , which is oddly enough closer to the two-fraction result of Ruud (Ruud, 2020). We did not experiment with anything other than single fraction dose treatments. Ruud also worked with cells human glioblastoma (T98) cell line which had no change in calreticulin expression post irradiation, similar to what we experienced with MOC1 cells (Ruud, 2020).

Gameiro et al. performed similar experiments by measuring DAMPs associated with ICD, including calreticulin. They used the cell lines MDA-MB-231 breast carcinoma, NCI-H522 lung carcinoma and LNCaP clone FGC. Calreticulin expression was measured using flow cytometry to analyse control cells (0 Gy) and cells irradiated with 10 Gy. They found an increase in cell surface expression for all the cell lines. In addition, they found that exposed CRT augmented CTL (cytotoxic T lymphocytes) killing of cancer cells. They also concluded with the fact RT induces a continuum of immunogenic alterations in tumor biology including radiation induced stress, subsequently leading to tumor sensitivity and CTL killing. They also claimed that CRT exposure alone is not sufficient for to elicit antitumor responses (Gameiro et al., 2014).

Huang et al. performed very similar experiments with human cancer cell lines, including A549. They used photon (X-ray), proton and carbon-ion irradiated cells with doses 0, 2, 4 10 Gy. They used 225 kV X-rays, 173.27 MeV protons and 333.82 MeV/u carbon ions, corresponding to an LET of approximately  $2 \text{ KeV}/\mu\text{m}$ ,  $1.98 \text{ KeV}/\mu\text{m}$  and  $29.1 \text{ KeV}/\mu\text{m}$ , respectively. It should be noted that the protons they used were sparsely ionizing, compared to ours. In fact, our 15 MeV protons in P5  $\sim 40 \text{ KeV}/\mu\text{m}$  had more LET

than their carbon ions  $\sim 30 \text{ KeV}/\mu\text{m}$ . Similarly, our “low” LET P1 protons  $\sim 10 \text{ KeV}/\mu\text{m}$  had roughly five times the LET of their protons  $\sim 2 \text{ KeV}/\mu\text{m}$ . The membrane bound calreticulin or ecto-CRT exposure was analysed with flow cytometry after 12, 24 and 48 hours post irradiation, and they calculated the median fluorescence intensities. What they found was a clear increase in CRT exposure for all cell lines irradiated with X-rays and protons from 0 Gy to 10 Gy, for carbon ions however, the largest increase was seen for 4 Gy and higher doses gave lower exposure. They assumed the decrease for carbon ions seen for 10 Gy was due to a combination of dose/LET that was too high induce ICD and these cells may have undergone a different death pattern (Huang et al., 2019). In general, looking at Huang et al.’s and our results we can assume that there is an optimal dose region where radiation induces the most amount of ICD for each cell line and radiation type. This means in a realistic setting where we are to combine RT and immune therapy (IT) for patient treatment, protons or heavy ion treatment may be favourable as less dose is required to achieve the same increase in immunogenicity, not to mention the benefits of better localized dose. One of the biggest goals with RT is to minimize the risks and side effects of the treatment, while having the same curative or palliative effects. This is especially the case with HNC, where there are many risk organs in the vicinity of a tumor. In this case the carbon ions are superior for treatment as we only require a dose of 4 Gy to achieve similar calreticulin expression levels in cells that received 10 Gy with X-rays or protons. The immunogenic signaling makes the immune system recognize the cancer cells as dangerous. However, the immune system also has a suppressive mechanism to avoid overreaction and autoimmune responses. This can be addressed by treatment with so-called immune checkpoint inhibitors. We already know that protons or other heavy charged particles have great potential for RT, but the data on immunogenic responses indicate that combining charged particles RT and IT could yield great benefits especially for HNC patients

Another study by Huang et al. looked at the impact of different types of irradiations under normoxic and hypoxic conditions on cell survival, CRT and programmed death-ligand 1 (PD-L1) expression of tumor cells after photon, proton and carbon ion irradiation (Huang et al., 2020). They found that for normoxic cells, colony formation was significantly inhibited after exposure to all types of irradiations. Hypoxic cells were radioresistant to photons and protons, but not carbon ions. Normoxic cells saw an increase in CRT expression after irradiation, which is consistent with previous study by the same authors. Hypoxic cells had an increase in

baseline CRT expression levels and did not see an increase in these levels after irradiation. Huang et al. claim that the increase in hypoxic cells seems to be a result of ER stress induced by hypoxia and seems to be similar to the ER stress radiation induces mediated by reactive oxygen species (ROS). In terms of calreticulin translocation to the cell membrane, ER stress induced by hypoxia seems to be similar to the ER stress radiation induces mediated by reactive oxygen species (ROS).

### 5.3 Protocol Development, Future Perspectives and Suggestions

The new assay without DyLight for barcoding control cells had some advantages and disadvantages. One advantage was that the assay became shorter and there was less waiting time. Previously the assay would start by harvesting and staining control cells for 30 minutes. One of the consequences of not having to do this anymore was that it was now much easier to perform two assays in parallel. For the last few experiments, two assays were performed in parallel, which practically doubled the rate of data acquirement. We followed the protocol seen in appendix 3 up until point 3, where we added primary antibody and incubated the samples on ice. At this point we could start from point 1 on the second assay. Assuming that the materials were ready, the second assay would be incubated for 30 minutes as the first assay was ready for washing. This cycle of working on one assay while waiting on the other made it so there was little to no down time and minimal waiting. It is a recommended method for those that have experience with the assay to gather more data in a shorter time. One of the later suggested changes which is found in the assay in appendix 3 is using cold PBS as opposed to PBS heated in a water bath. This way there would be less of a temperature difference between the PBS and samples incubated in ice with antibodies.

The new CRT assay protocol also had its weaknesses. This is mainly related to the fact that there is only one control for 3 irradiated samples. It can be difficult to assert whether a high fluorescence ratio is caused by a significant increase in calreticulin expression, or by a questionable control sample. It should be noted that looking at the median intensity values instead of the ratios between the control and irradiated samples can be misleading. Differences in laboratory procedures and assay techniques, such as how supernatant fluid is aspirated and how much fluid is left before adding antibodies can result in different concentrations of antibodies during incubation. This leads to differences in absolute value for the intensities detected by the FL4 channel in the flow cytometer. Hence, why it is important

to include at least one control sample for each assay, because one cannot compare the absolute values found for the samples receiving the same treatment, such as the control cells for the same cell line. Ideally, the control values should always be the same as the cells are identical and receive the same treatment. This is not always the case and sometimes significant differences are seen by the large error bars for MOC1 and MOC2 in Figure 48. An example is the previously discussed control values (PA +SA and SA) for 4 Gy P1 irradiated A549 cells compared to the control for 4 Gy P5 irradiated A549 cells. This problem could be resolved by increase the number of control samples or performing two CRT assays in parallel with samples receiving the same treatment. The former suggestion would change the protocol, increasing the time, the number of samples and substance volumes required for an assay, while the latter would double the workload for a single experiment.

Proton experiments, especially those that did not have a statistical significance with the X-ray results should be repeated. X-ray experiments should also be repeated for MOC2 and A549 cells to confirm our results. CRT assay should not be prioritized with MOC1 cells, due to the lack of immunogenic signaling after irradiation. Although our results show that MOC1 has lower fluorescence intensity than MOC2, meaning less CRT expression this does not mean that MOC1 is less immunogenic. Other DAMPs in MOC1 could be measured and investigated in future experiments. Clonogenic assay should also be repeated for MOC1 and MOC2 to reevaluate our results.

It could also be interesting to change some parameters for CRT assay. We performed CRT assay roughly 48 hours after irradiation. Huang et al. performed analysis 12, 24 and 48 hours post irradiation (Huang et al., 2019), which should be replicated. It is possible that the timing for the full signal is different for different doses and LET and should be adjusted accordingly. In addition, varying the time post irradiation could also be combined with fractionating doses. Ruud's results showed a significant difference between samples receiving the same total dose with different number of fractionations (Ruud, 2020). It also makes sense to try different fractionations regimes with respect to radiotherapy.

## 6 Conclusion

The main goal with this thesis was to investigate immunogenic signaling in human lung A549, mouse oral squamous carcinoma MOC1 and MOC2 cell lines after X-ray and proton irradiation. This was done by measuring calreticulin (CRT) translocated to the cell surface as a result of immunogenic cell death induced (ICD) by ionizing radiation. Clonogenic assays were performed to make survival curves for MOC1 and MOC2 to compare survival fraction with CRT expression after irradiation. The CRT assay protocol established by previous master students were adjusted to accommodate for the MOC1 and MOC2 cell lines.

Based on our results we can conclude with the following: MOC1 is more radiosensitive than MOC2, with  $\alpha/\beta$ - values  $6.4 \pm 0.7$  and  $3.4 \pm 0.4$ , respectively. Out of the three cell lines we used for calreticulin measurements, A549 had the lowest calreticulin expression, but was also the cell line that experienced the greatest change in CRT expression after irradiation. A549 cells irradiated with a dose of 8 Gy had an increase in CRT expression level by a factor of  $1.60 \pm 0.03$  for X-rays,  $6.96 \pm 0.63$  for protons in front of the Bragg peak (P1, LET  $\sim 10 \text{ KeV}/\mu\text{m}$ ) ( $P_{X,P1} = 0.02$ ) and  $3.57 \pm 0.21$  at the distal end of the Bragg peak (P5, LET  $\sim 40 \text{ KeV}/\mu\text{m}$ ) ( $P_{X,P5} = 0.02$ ). A lower ratio for higher LET might be caused by a saturation effect or different forms of cell death being induced. MOC1 had high calreticulin expression levels, but these levels did not change with irradiation, no matter the dose or LET, the ratios before and after irradiation were close to 1 for all doses and radiation types. MOC2 was the most immunogenic in terms of calreticulin expression especially after 8 Gy irradiation, with an enhancement in CRT expression by a factor  $1.81 \pm 0.09$  for X-rays,  $1.19 \pm 0.08$  for P1 protons (not statistically significant,  $P_{X,P1} = 0.1$ ) and  $2.21 \pm 0.15$  for P5 protons ( $P_{X,P5} = 0.03$ ). Based on Huang et al.'s (2019) and our results, ionizing radiation with higher LET seems to be more efficient at inducing immunogenic cell death in certain dose regions. This could indicate a great benefit of combining protons or heavy ions with immunotherapy for difficult to treat cancers such as HNC.

# References

- Adan, A., Alizada, G., Kiraz, Y., Baran, Y., Nalbant, A. (2016). *Flow Cytometry: Basic Principles and Applications*. Critical Reviews in Biotechnology.
- Agre, Peter (2006). *The Aquaporin water channels* Proceedings of the American Thoracic Society.
- Alberts, B. (2015). *Molecular Biology of the Cell sixth edition*. New York, NY: Garland Science, Taylor and Francis Group.
- Ashrafizadeh, M., Farhood, B., Eleojo Musa, A., Taeb, S., Rezaeyan, A., & Najafi, M. (2020). *Abscopal effect in radioimmunotherapy*. International immunopharmacology.
- Attix, F. H. (1986). *Introduction to radiological physics and radiation dosimetry*. New York: John Wiley & Sons.
- Blanchard, P, et al., *Proton Therapy for Head and Neck Cancers*. Semin Radiat Oncol, 2018; 28: 53-63.
- Britannica, The Editors of Encyclopaedia (2018). *Cyclotron*. Encyclopedia Britannica, <https://www.britannica.com/technology/cyclotron>. Accessed 26 December 2021.
- Cash, H., Shah, S., Moore, E., Caruso, A., Uppaluri, R., Van Waes, C., & Allen, C. (2015). *mTOR and MEK1/2 inhibition differentially modulate tumor growth and the immune microenvironment in syngeneic models of oral cavity cancer*. Oncotarget.
- Chang, H., Pannunzio, N. R., Adachi, N., & Lieber, M. R. (2017). *Non-homologous DNA end joining and alternative pathways to double-strand break repair*. Nature reviews. Molecular cell biology
- Chatterjee, N., & Walker, G. C. (2017). *Mechanisms of DNA damage, repair, and mutagenesis*. Environmental and molecular mutagenesis.
- Cooper GM. The Cell: A Molecular Approach. 2nd edition. Sunderland (MA): Sinauer Associates; 2000. The Eukaryotic Cell Cycle. <https://www.ncbi.nlm.nih.gov/books/NBK9876/> Accessed 16. April 2022
- Davis, J. M. (2011). *Animal Cell Culture Essential Methods*. Wiley-Blackwell.
- DMEM/F-12 (n.d.). <https://www.thermofisher.com/order/catalog/product/11320033>. Accessed (01.05.2022)

Duggan, Ryan (2016). Basic Parameters Measured by a Flow Cytometer: What is Scattered Light and Absolute Fluorescence? Bitesizebio.com. Accessed (16.05.2022)

Elkind MM, Whitmore GF (1967) Survival Curve Theory. In *The Radiobiology of Cultured Mammalian Cells*, Elkind MM, Whitmore GF (eds) pp 7-52. Gordon and Breach: New York

Fowler J. F. (1984). *Review: total doses in fractionated radiotherapy--implications of new radiobiological data*. International journal of radiation biology and related studies in physics, chemistry, and medicine.

Fucikova J, Spisek R, Kroemer G, Galluzzi L (2021). *Calreticulin and cancer*. *Cell Research*

Gameiro, S. R., Jammeh, M. L., Wattenberg, M. M., Tsang, K. Y., Ferrone, S., & Hodge, J. W. (2014). *Radiation-induced immunogenic modulation of tumor enhances antigen processing and calreticulin exposure, resulting in enhanced T-cell killing*. *Oncotarget*. s

Giard, D. J., Aaronson, S. A., Todaro, G. J., Arnstein, P., Kersey, J. H., Dosik, H., & Parks, W. P. (1973). *In vitro cultivation of human tumors: establishment of cell lines derived from a series of solid tumors*. Journal of the National Cancer Institute.

Hall, E. J., & Giaccia, A. J. (2019). *Radiobiology for the Radiobiologist Eight Edition*. Philadelphia: Wolters Kluwer.

Hofmann, Siegfried (2013). *Auger- and X-ray Photoelectron Spectroscopy in Material Science*. Springer-Verlag Berlin Heidelberg.

Huang, Y., Dong, Y., Zhao, J., Zhang, L., Kong, L., & Lu, J. J. (2019). *Comparison of the effects of photon, proton and carbon-ion radiation on the ecto-calreticulin exposure in various tumor cell lines*. *Annals of translational medicine*.

Huang, Y., Huang, Q., Zhao, J., Dong, Y., Zhang, L., Fang, X., Sun, P., Kong, L., & Lu, J. J. (2020). *The Impacts of Different Types of Radiation on the CRT and PDL1 Expression in Tumor Cells Under Normoxia and Hypoxia*. *Frontiers in oncology*.

Hussain, A., Muhammed, W. (2017). *An Introduction to Medical Physics*. Springer International Publishing AG.



Iscove's Modified Dulbecco's Medium (IMDM) (n.d). <https://www.thermofisher.com/>  
Accessed (01.05.2022)

Jin, W. J., Erbe, A. K., Schwarz, C. N., Jaquish, A. A., Anderson, B. R., Sriramaneni, R. N., Jagodinsky, J. C., Bates, A. M., Clark, P. A., Le, T., Lan, K. H., Chen, Y., Kim, K., & Morris, Z. S. (2020). *Tumor-Specific Antibody, Cetuximab, Enhances the In Situ Vaccine Effect of Radiation in Immunologically Cold Head and Neck Squamous Cell Carcinoma*. *Frontiers in immunology*.

Ko, E. C., Benjamin, K. T., & Formenti, S. C. (2018). *Generating antitumor immunity by targeted radiation therapy: Role of dose and fractionation*. *Advances in radiation*

Linz, U. (2012). *Ion Beam Therapy*. Springer-Verlag Berlin Heidelberg.

Liu, Y., Dong, Y., Kong, L., Shi, F., Zhu, H., & Yu, J. (2018). *Abscopal effect of radiotherapy combined with immune checkpoint inhibitors*. *Journal of hematology & oncology*

Mayles, P., Nahum, A., Rosenwald, J. C. (2007). *Handbook of Radiotherapy Physics, Theory and Practice*. Taylor & Francis Group, LLC.

Marcu, L. G., Dasu, I. T., Dasu, A. (2015). *The Six Rs of Head and Neck Cancer Radiotherapy*. *Contemporary Issues in Head and Neck Cancer Management*, Intech Open, London

McMahon, S. J. (2019). *The Linear Quadratic Model Usage, Interpretation and Challenges*. *Phys. Med. Biol. IPEM*.

McKinnon, Katherine M. (2019). *Flow Cytometry: An Overview*. *Curr Protoc Immunol*.

Melvik, J. E. (1983). *Effekt av cisplatin på celleoverlevelse, cellesyklusprogresjon og strålefølsomhet hos mammalske celler i kultur*. Cand. Real. thesis: University of Oslo

Obodovski, I. (2019). *Radiation: Fundamentals, Applications, Risks and Safety*. Elsevier

Pardoll, D. M. (2016). *The blockade of immune checkpoints in cancer immunotherapy*. *Nat Rev Cancer*.

Podgoršak, E. B. (2016). *Radiation Physics for Medical Physicists* Springer Heidelberg Dordrecht London New York.

Punt, J., Stranford, S., Jones, P., Owen, J. (2019). *Kunt Immunology (Eight Edition)*. W. H. Freeman.

Ruud, M. Engelhard-Olsen (2020). *Immunogenic signaling in lung cancer in response to ionizing radiation*. Cand. Scient. thesis: University of Oslo

Sabloff, M., Tisseverasinghe, S., Babadagli, M. E., & Samant, R. (2021). *Total Body Irradiation for Hematopoietic Stem Cell Transplantation: What Can We Agree on?* Current oncology

Sapkota, Anupama (2022). *Flow Cytometry – Definition, Principle, Parts, Types, Uses*. Microbe Notes. Retrieved <https://microbenotes.com/flow-cytometry/> (07.05.2022)

Schwarz DS, Blower MD (2016). *The endoplasmic reticulum: structure, function and response to cellular signaling*. Cell Mol Life Sci.

Seibert, J. A. (2004). *X-ray Imaging Physics for Nuclear Medicine Technologists Part 1: Basic Principles of X-ray Production*. Journal of Nuclear Medicine Technology.

Skeie, H. S. (2021). *The Relative Biological Effectiveness of Low Energy Protons for Human Lung Carcinoma Cells*. Cand. Scient. thesis: University of Oslo.

Sollund, Håvar (2009). *Mechanisms for Elimination of Low-Dose Hyper-Radiosensitivity*. Cand. Scient. thesis: University of Oslo.

Sutton, Christine. *Particle accelerator*. *Encyclopedia Britannica*, 9 Apr. 2020, <https://www.britannica.com/technology/particle-accelerator>. Accessed 17 January 2022.

Thermo Fisher Scientific. (2020). Retrieved from <https://www.thermofisher.com/no/en/home/life-science/cell-culture/mammalian-cell-culture/reagents/trypsin/tryple-express.html> (01.05.2022)

Thingstad, E. K. (2019). *Immunogenic calreticulin signaling in lung and glioblastoma cancer cells after X-ray and proton irradiation*. Cand. Scient. thesis: University of Oslo

Torre, L. A., Siegel, R. L., Ward, E. M., & Jemal, A. (2016). *Global Cancer Incidence and Mortality Rates and Trends--An Update*. Cancer epidemiology, biomarkers & prevention.

van Leeuwen, C.M., Oei, A.L., Crezee, J. et al. (2018). *The alfa and beta of tumours: a review of parameters of the linear-quadratic model, derived from clinical radiotherapy studies*. Radiat Oncol.

van den Bulk, J., Verdegaal, E. M., & de Miranda, N. F. (2018). *Cancer immunotherapy: broadening the scope of targetable tumours*. Open biology.

Wille, Klaus (2001). *The Physics of Particle Accelerators: An Introduction*. Oxford University Press, USA.

Williams, M. V., Denekamp, J., & Fowler, J. F. (1985). *A review of alpha/beta ratios for experimental tumors: implications for clinical studies of altered fractionation*. International journal of radiation oncology, biology, physics.

Yang, Y. (2015). *Cancer immunotherapy: harnessing the immune system to battle cancer*. J Clin Invest.

## Appendix 1

Table 6 and Table 7 gives an overview of the median and mean values found in the FL4 channel for each CRT assay performed during this thesis, respectively. The Strikethrough data was not included due to various reasons.

Date	P+S AB Median		SAB Median		Cell Line / Irradiation type
	Control Sample	Irr. Sample (Dose)	Control Sample	Irr. Sample (Dose)	
15.10.2021	-	-	-	-	A549/X-rays
05.11.2021	1584	2439 (8 Gy)	665	1055 (8 Gy)	A549/X-rays
	1669	2573 (8 Gy)	671	1022 (8 Gy)	A549/X-rays
	1598	2515 (8 Gy)	646	932 (8 Gy)	A549/X-rays
24.11.2021	1389	2198 (8 Gy)	608	971 (8 Gy)	A549/X-rays
	1262	1966 (8 Gy)	634	900 (8 Gy)	A549/X-rays
	1296	1848 (8 Gy)	610	704(8 Gy)	A549/X-rays
26.01.2022	-	-	-	-	A549/X-rays
03.02.2022	-	-	-	-	A549/X-rays
04.02.2022	<del>6799</del>	<del>5481 (2 Gy)</del>	<del>684</del>	<del>663 (2 Gy)</del>	MOC1/X-rays
	<del>6038</del>	<del>5491 (4 Gy)</del>	<del>787</del>	<del>654 (4 Gy)</del>	MOC1/X-rays
		<del>5261 (6 Gy)</del>		<del>673 (6 Gy)</del>	MOC1/X-rays
		<del>4987 (8 Gy)</del>		<del>760 (8 Gy)</del>	MOC1/X-rays
25.02.2022	<del>2981</del>	<del>4410 (2 Gy)</del>	<del>704</del>	<del>937 (2 Gy)</del>	MOC2/X-rays
		<del>4374 (4 Gy)</del>		<del>960 (4 Gy)</del>	MOC2/X-rays
		<del>5071 (6 Gy)</del>		<del>991 (6 Gy)</del>	MOC2/X-rays
		<del>5422 (8 Gy)</del>		<del>968 (8 Gy)</del>	MOC2/X-rays
11.03.2022	<del>12850</del>	<del>10912 (6 Gy)</del>	<del>923</del>	<del>1215 (6 Gy)</del>	MOC2/X-rays
	<del>9578</del>	<del>15165 (6 Gy)</del>	<del>977</del>	<del>1246 (6 Gy)</del>	MOC2/X-rays

17.03.2022	3210	10986 (4 Gy) 10489 (4 Gy) 9983 (4 Gy)	873	2209 (4 Gy) 1677 (4 Gy) 1753 (4 Gy)	A549/P5 A549/P5 A549/P5
	19074	45936 (4 Gy) 32052 (4 Gy) 26527 (4 Gy)	1044	1958 (4 Gy) 1806 (4 Gy) 1867 (4 Gy)	MOC2/P5 MOC2/P5 MOC2/P5
	1626	6999 (4 Gy) 5598 (4 Gy) 5743 (4 Gy)	1172	1470 (4 Gy) 1484 (4 Gy) 1426 (4 Gy)	A549/P1 A549/P1 A549/P1
	26955	42192 (4 Gy) 31342 (4 Gy) 31416 (4 Gy)	1055	1472 (4 Gy) 1523 (4 Gy) 1330 (4 Gy)	MOC2/P1 MOC2/P1 MOC2/P1
18.03.2022	3561	13926 (8 Gy) 13157 (8 Gy) 11870 (8 Gy)	796	1647 (8 Gy) 1515 (8 Gy) 1971 (8 Gy)	A549/P5 A549/P5 A549/P5
	12168	30201 (8 Gy) 25702 (8 Gy) 22802 (8 Gy)	1211	2171 (8 Gy) 1943 (8 Gy) 1730 (8 Gy)	MOC2/P5 MOC2/P5 MOC2/P5
	2986	11649 (8 Gy) 8635 (8 Gy) 8746 (8 Gy)	1852	1447 (8 Gy) 1138 (8 Gy) 1086 (8 Gy)	A549/P1 A549/P1 A549/P1
	15542	16583 (8 Gy) 18458 (8 Gy) 21001 (8 Gy)	1036	1447 (8 Gy) 1371 (8 Gy) 1228 (8 Gy)	MOC2/P1 MOC2/P1 MOC2/P1
19.03.2022	17999	21123 (4 Gy) 20670 (4 Gy) 18939 (4 Gy)	754	1399 (4 Gy) 1201 (4 Gy) 1055 (4 Gy)	MOC1/P5 MOC1/P5 MOC1/P5
		9088 (4 Gy)		679 (4 Gy)	

	7709	8408 (4 Gy) 7069 (4 Gy)	478	607 (4 Gy) 450 (4 Gy)	MOC1/P5 MOC1/P5 MOC1/P1
20.03.2022	12165	10824 (4 Gy) 10794 (4 Gy) 19550 (8 Gy) 13621 (8 Gy) 14147 (8 Gy)	522	579 (4 Gy) 637 (4 Gy) 684 (4 Gy) 618 (8 Gy) 589 (8 Gy)	MOC1/P1 MOC1/P1 MOC1/P1 MOC1/P1 MOC1/P1
	16414	14219 (8 Gy) 15291 (8 Gy) 13241 (8 Gy)	514	733 (8 Gy) 987 (8 Gy) 794 (8 Gy)	MOC1/P5 MOC1/P5 MOC1/P5
31.03.2022	9444	10707 (8 Gy) 11103 (8 Gy) 10733 (8 Gy)	642	834 (8 Gy) 813 (8 Gy) 766 (8 Gy)	MOC1/X-rays MOC1/X-rays MOC1/X-rays
	10139	12532 (4 Gy) 12308 (4 Gy) 10800 (4 Gy)	623	724 (4 Gy) 658 (4 Gy) 707 (4 Gy)	MOC1/X-rays MOC1/X-rays MOC1/X-rays
07.04.2022	7327	13643 (8 Gy) 10979 (8 Gy) 12350 (8 Gy)	897	957 (8 Gy) 929 (8 Gy) 1043 (8 Gy)	MOC2/X-rays MOC2/X-rays MOC2/X-rays
	5271	7253 (4 Gy) 6635 (4 Gy) 6105 (4 Gy)	777	844 (4 Gy) 876 (4 Gy) 806 (4 Gy)	MOC2/X-rays MOC2/X-rays MOC2/X-rays

Table 6: Raw data from flow cytometer showing the median fluorescence values found in the FL4-channel. Values that are not separated constitutes a single experiment

Date	P+S AB Mean		SAB Mean		Cell Line / Irradiation type
	Control Sample	Irr. Sample (Dose)	Control Sample	Irr. Sample (Dose)	
15.10.2021	-	-	-	-	A549/X-rays
05.11.2021	1788	2584(8 Gy)	778	1133(8 Gy)	A549/X-rays
	1889	2663(8 Gy)	805	1114(8 Gy)	A549/X-rays
	1828	2731(8 Gy)	777	1035(8 Gy)	A549/X-rays
24.11.2021	1509	2440(8 Gy)	759	1132 (8 Gy)	A549/X-rays
	1378	2174(8 Gy)	763	1094 (8 Gy)	A549/X-rays
	1402	2099(8 Gy)	736	873 (8 Gy)	A549/X-rays
26.01.2022	-	-	-	-	A549/X-rays
03.02.2022	-	-	-	-	A549/X-rays
04.02.2022	8115	<del>6552 (2 Gy)</del>	992	<del>830(2 Gy)</del>	MOC1/X-rays
	7035	<del>6803 (4 Gy)</del>	1137	<del>890(4 Gy)</del>	MOC1/X-rays
		<del>6623 (6 Gy)</del>		<del>879(6 Gy)</del>	MOC1/X-rays
		<del>6298 (8 Gy)</del>		<del>903(8 Gy)</del>	MOC1/X-rays
25.02.2022	3511	<del>5303 (2 Gy)</del>	1161	<del>1484(2 Gy)</del>	MOC2/X-rays
		<del>5247(4 Gy)</del>		<del>1385(4 Gy)</del>	MOC2/X-rays
		<del>6529(6 Gy)</del>		<del>1238(6 Gy)</del>	MOC2/X-rays
		<del>6362(8 Gy)</del>		<del>1283(8 Gy)</del>	MOC2/X-rays
11.03.2022	<del>16591</del>	<del>15532 (6 Gy)</del>	<del>1421</del>	<del>2228 (6 Gy)</del>	MOC2/X-rays
	13144	20972 (6 Gy)	1301	2347 (6 Gy)	MOC2/X-rays

17.03.2022	3812	12434 (4 Gy) 11950 (4 Gy) 11662 (4 Gy)	1080	2382 (4 Gy) 1818 (4 Gy) 1967 (4 Gy)	A549/P5 A549/P5 A549/P5
	25603	58215(4 Gy) 41620 (4 Gy) 34909 (4 Gy)	1908	2834 (4 Gy) 2957 (4 Gy) 3027 (4 Gy)	MOC2/P5 MOC2/P5 MOC2/P5
	1813	7765 (4 Gy) 6374 (4 Gy) 6630 (4 Gy)	1310	1609 (4 Gy) 1623 (4 Gy) 1558 (4 Gy)	A549/P1 A549/P1 A549/P1
	35427	54648 (4 Gy) 40848 (4 Gy) 39956 (4 Gy)	2056	2941 (4 Gy) 2139 (4 Gy) 2636 (4 Gy)	MOC2/P1 MOC2/P1 MOC2/P1
18.03.2022	4359	15546 (8 Gy) 14862 (8 Gy) 13522 (8 Gy)	902	1787 (8 Gy) 1646 (8 Gy) 3490 (8 Gy)	A549/P5 A549/P5 A549/P5
	16174	41371 (8 Gy) 35082 (8 Gy) 32584 (8 Gy)	3089	3456 (8 Gy) 2640 (8 Gy) 3082 (8 Gy)	MOC2/P5 MOC2/P5 MOC2/P5
	3414	13632 (8 Gy) 10242 (8 Gy) 10258 (8 Gy)	1979	1625 (8 Gy) 1274 (8 Gy) 1258 (8 Gy)	A549/P1 A549/P1 A549/P1
	20130	21928(8 Gy) 24068 (8 Gy) 27582 (8 Gy)	2084	2575 (8 Gy) 2281 (8 Gy) 2043 (8 Gy)	MOC2/P1 MOC2/P1 MOC2/P1
19.03.2022	21912	32037 (4 Gy) 30761 (4 Gy) 26274 (4 Gy)	932	1696 (4 Gy) 1421 (4 Gy) 1275 (4 Gy)	MOC1/P5 MOC1/P5 MOC1/P5
		12609 (4 Gy)		822 (4 Gy)	



	9215	11566 (4 Gy) 8444 (4 Gy)	559	729 (4 Gy) 559 (4 Gy)	MOC1/P5 MOC1/P5 MOC1/P1
20.03.2022	15069	13691 (4 Gy) 13779 (4 Gy) 26017 (8 Gy) 18981 (8 Gy) 19313 (8 Gy)	656	708 (4 Gy) 766 (4 Gy) 848 (8 Gy) 799 (8 Gy) 740 (8 Gy)	MOC1/P1 MOC1/P1 MOC1/P1 MOC1/P1 MOC1/P1
	19499	24247 (8 Gy) 25135 (8 Gy) 20997 (8 Gy)	651	907 (8 Gy) 1250 (8 Gy) 1054 (8 Gy)	MOC1/P5 MOC1/P5 MOC1/P5
31.03.2022	11764	15466 (8 Gy) 15770 (8 Gy) 15108 (8 Gy)	803	992 (8 Gy) 1015 (8 Gy) 948 (8 Gy)	MOC1/X-rays MOC1/X-rays MOC1/X-rays
	12646	16955 (4 Gy) 16411 (4 Gy) 14170 (4 Gy)	742	864 (4 Gy) 875 (4 Gy) 862 (4 Gy)	MOC1/X-rays MOC1/X-rays MOC1/X-rays
07.04.2022	9306	17267 (8 Gy) 14161 (8 Gy) 15853 (8 Gy)	1433	1301 (8 Gy) 1197 (8 Gy) 1347 (8 Gy)	MOC2/X-rays MOC2/X-rays MOC2/X-rays
	7035	9531 (4 Gy) 8299 (4 Gy) 7954 (4 Gy)	1175	1102 (4 Gy) 1439 (4 Gy) 1181 (4 Gy)	MOC2/X-rays MOC2/X-rays MOC2/X-rays

Table 7: Raw data from flow cytometer showing the mean fluorescence values found in the FL4-channel. Values that are not separated constitutes a single experiment.

## Appendix 2

Table 8 and Table 9 gives an overview of the average values for the relative median and mean fluorescence intensities, respectively. These ratios are based on the raw data in Table 6 and Table 7, respectively.

Dose	Relative Median Fluorescence Intensity	Cell Line	Irradiation type
<b>8 Gy</b>	$1.60 \pm 0.03$	A549	X-rays
<b>4 Gy</b>	$1.17 \pm 0.05$	MOC1	X-rays
<b>8 Gy</b>	$1.14 \pm 0.01$	MOC1	X-rays
<b>4 Gy</b>	$1.34 \pm 0.07$	MOC2	X-rays
<b>8 Gy</b>	$1.81 \pm 0.09$	MOC2	X-rays
<b>4 Gy</b>	$10.6 \pm 0.8$	A549	Protons P1
<b>8 Gy</b>	$6.96 \pm 0.63$	A549	Protons P1
<b>4 Gy</b>	$3.64 \pm 0.07$	A549	Protons P5
<b>8 Gy</b>	$3.57 \pm 0.21$	A549	Protons P5
<b>4 Gy</b>	$0.89 \pm 0.01$	MOC1	Protons P1
<b>8 Gy</b>	$1.30 \pm 0.13$	MOC1	Protons P1
<b>4 Gy</b>	$1.11 \pm 0.03$	MOC1	Protons P5
<b>8 Gy</b>	$0.84 \pm 0.03$	MOC1	Protons P5
<b>4 Gy</b>	$1.29 \pm 0.11$	MOC2	Protons P1
<b>8 Gy</b>	$1.19 \pm 0.08$	MOC2	Protons P1
<b>4 Gy</b>	$1.83 \pm 0.26$	MOC2	Protons P5
<b>8 Gy</b>	$2.21 \pm 0.15$	MOC2	Protons P5

Table 8: The median fluorescence intensity ratio by using Eq. (29) for raw data in Table 6. Uncertainties are given as SEM.

Dose	Relative Mean Fluorescence Intensity	Cell Line	Irradiation type
<b>8 Gy</b>	$1.64 \pm 0.06$	A549	X-rays
<b>4 Gy</b>	$1.26 \pm 0.06$	MOC1	X-rays
<b>8 Gy</b>	$1.31 \pm 0.01$	MOC1	X-rays
<b>4 Gy</b>	$1.35 \pm 0.10$	MOC2	X-rays
<b>8 Gy</b>	$1.92 \pm 0.09$	MOC2	X-rays
<b>4 Gy</b>	$10.6 \pm 0.69$	A549	Protons P1
<b>8 Gy</b>	$6.96 \pm 0.57$	A549	Protons P1
<b>4 Gy</b>	$3.64 \pm 0.04$	A549	Protons P5
<b>8 Gy</b>	$3.56 \pm 0.27$	A549	Protons P5
<b>4 Gy</b>	$0.905 \pm 0.002$	MOC1	Protons P1
<b>8 Gy</b>	$1.43 \pm 0.13$	MOC1	Protons P1
<b>4 Gy</b>	$1.33 \pm 0.05$	MOC1	Protons P5
<b>8 Gy</b>	$1.19 \pm 0.05$	MOC1	Protons P5
<b>4 Gy</b>	$1.28 \pm 0.11$	MOC2	Protons P1
<b>8 Gy</b>	$1.23 \pm 0.08$	MOC2	Protons P1
<b>4 Gy</b>	$1.77 \pm 0.24$	MOC2	Protons P5
<b>8 Gy</b>	$2.54 \pm 0.15$	MOC2	Protons P5

Table 9: The mean fluorescence intensity ratio by using Eq. (29) for raw data in Table 7. Uncertainties are given as SEM.

## Appendix 3

### CRT assay for flow cytometry (no dye, control as sample)

The assay was optimized for cell line MOC1+2 and A549. Different cell lines might need higher or lower concentrations of antibodies.

<i>Compound</i>	<i>Amount/sample + control (4 dishes)</i>		<i>Storage</i>
<i>PBS</i>	150 ml	-	Fridge cell lab
<i>PBS w/BSA(1%)</i>	2 ml	-	Freezer chemical storage
<i>TrypLE</i>	8	-	Freezer chemical storage
<i>Medium</i>	16	-	Fridge cell lab
<i>DyLight</i>	-	-	Freezer instrument lab
<i>Primary antibody</i>	2,25 µl in 450 µl PBS w/BSA (5 µL/ml)	-	Freezer instrument lab
<i>Secondary antibody</i>	2,25 µl in 900 µl PBS w/BSA (2,5 µL/ml)	-	Fridge instrument lab

Primary antibody **Anti-Calreticulin antibody (ab2907), rabbit polyclonal (Freezer)**

Secondary antibody **Alexa Fluor 647 goat anti-rabbit IgG (H+L) (Fridge)**

**PBS and Medium at room temperature**

**Ice from Ice machine**

#### 1. Harvest samples (3 dish) and control (1dish)

Remove medium

Flush with 5 ml PBS

Add 2ml TrypLE, flush a few times and incubate for about 4 min

Suspend to single cells with 2 ml pipette

Add 4 ml medium and transfer to tube.

Centrifuge 200xg, 4 min

**Samples and Control:** Aspirate and resuspend in 10 ml PBS

## 2. Split samples in two (PBS cold)

Split each sample so each have a secondary antibody control.

Fill 4 tubes with 5 ml PBS first.

Add 5 ml of sample to each.

Add 5 ml PBS to original sample tubes.

You now have 8 sample, 4 shall have primary + secondary antibody, 4 will only have secondary antibody.

Centrifuge 200 x g, 4 min, put on ice and aspirate before adding primary antibody.

## 3. Primary Antibody

Mix: number of samples x (0, 5 µl primary ab/100 µl PBS w/BSA).

- 4 sample: add 2,25 µl to 450 µl **PBS w/BSA**.

Add mix to the 4 samples and add 100 µl PBS w/BSA to the secondary ab controls.

Incubate in dark for 30 min on ice.

## 4. Wash

Add 3ml PBS to each sample, centrifuge 200 xg, 4 min.

Aspirate supernatant.

Repeat once more.

## 5. Secondary Antibody

Mix: number of samples x (0,25 µl primary ab/100 µl PBS w/BSA).

- $4 \times 2 = 8$  sample: add 2,25 µl to 900 µl

Resuspend all pellets in 100 µl mix.

Incubate in dark for 30 minutes on ice.

## 6. Wash

Add 3ml PBS to each sample, centrifuge 200 xg, 4 min.

Aspirate supernatant.

Repeat once more.

Resuspend the pellets in 250 µl PBS and store at 4°C until flow cytometry analysis.

## 7. Live/dead staining, filtering, and flow analysis

Prior to flow cytometry analysis, add 0.5µl propidium iodine (PI) 1.0 mg/ml to the samples for live/dead staining, right before filtering into tubes and running flow.

Abbreviation	Name	Substance	Channel
PA	Primary Antibody	Anti-Calreticulin antibody (ab2907), rabbit polyclonal	
SA	Secondary Antibody	Alexa Fluor 647 goat anti rabbit IgG (H+L)	FL4
PI	Live/Death	Propidium iodide solution	FL2, FL3

## Appendix 4

Here we have the data for CFA experiments, MOC1 data in Table 10 and MOC2 data provided by Frida Larsen in Table 11.

CFA Experiment Date and Multiplicity	Number of colonies counted for each dose					
Experiment 07.9.2021	0 Gy (200)	1 Gy (200)	2 Gy (200)	5 Gy (500)	7.5 Gy (1500)	10 Gy (10 000)
<b><math>M = 1.416</math></b>	69	42	55	77		
	80	52	60	79		
	76	41	61	76		
	72	60	50	72		
	64					
	57					
	80					
	70					
Experiment 25.10.2021 <b><math>M = 1.468</math></b>	191	102	135	3		
	199	68	136	27		
	170	78	158	29		
	148	67	146	65		
	196					
	147					
	181					
	72					
Experiment 18.01.2022 <b><math>M = 1.288</math></b>	124	98	57	68	65	52
	119	92	91	62	42	20
	119	95	52	53	44	28
	133	100	81	66	43	17
	136					
	131					
	151					
	152					
Experiment 11.02.2022 <b><math>M = 1.341</math></b>	230	160	146	40	22	19
	223	173	122	49	23	7
	222	195	128	50	16	9
	223	193	105	62	25	13
	216					
	228					
	211					
	174					

Experiment 21.02.2022 $M = 1.331$	83	107	63	28	10	3
	112	93	74	22	13	4
	128	84	56	34	8	5
	126	76	60	32	10	4
	101					
	95					
	92					
	106					

Table 10: Overview of the results from successful colony formation assays with the MOC1 cell line.  $M$  is the multiplicity for each experiment. The numbers in the parenthesis below the doses are the ideal number of cells seeded in the flasks receiving those doses, as shown in Table 2.

CFA Experiment Date and Multiplicity	Number of colonies counted for each dose					
Experiment 02.09.2021	0 Gy (200)	1 Gy (200)	2 Gy (200)	5 Gy (500)	7.5 Gy (1500)	10 Gy (10 000)
$M = 1.43$	34	27	19	13		
	32	28	18	10		
	26	25	25	10		
	29	17	14	13		
	28					
	41					
	43					
	29					
Experiment 08.09.2021 $M = 1.29$	42	36	40	20		
	46	40	23	26		
	42	35	35	21		
	41	31	29	27		
	48					
	45					
	32					
	43					
Experiment 03.11.2021 $M = 2.17$	23	10	11	13		
	24	20	15	15		
	18	17	22	20		
	16	24	21	18		
	18					
	19					
	26					
	21					



Experiment 09.12.2021 $M = 2.33$	61	62	45	40	27	15
	44	56	52	48	26	10
	65	50	61	52	23	20
	64	57	36	57	31	17
	64					
	65					
	58					
	61					
Experiment 26.01.2022 $M = 2.43$	53	48	32	35	31	32
	66	41	45	32	25	17
	63	50	38	38	22	14
	53	56	43	54	9	15
	56					
	45					
	54					
	51					
Experiment 10.02.2022 $M = 2.84$	<del>49</del>	<del>56</del>	<del>45</del>		<del>18</del>	<del>16</del>
	<del>49</del>	<del>57</del>	<del>57</del>		<del>17</del>	<del>10</del>
	<del>38</del>	<del>57</del>	<del>39</del>		<del>21</del>	<del>16</del>
	<del>49</del>	<del>50</del>	<del>42</del>		<del>20</del>	<del>12</del>
	<del>55</del>					
	<del>42</del>					
	<del>42</del>					
	<del>52</del>					

Table 11 Overview of the results from successful colony formation assays with the MOC2 cell line, provided by Frida Larsen.  $M$  is the multiplicity for each experiment. The numbers in the parenthesis below the doses are the ideal number of cells seeded in the flasks receiving those doses, as shown in Table 2. The last experiment is marked red and strikethrough as it was not used in analysis. The main reason for this is due to the relatively high multiplicity  $M = 2.84$  which caused problems in the calculations using the equations found in section 3.4.2.

## Appendix 5

### Clonogenic Assay for MOC1 Cell Line

#### Day 1

1. Prepare and mark 8 flasks for control, 4 flasks for each intended irradiation dose and 1 flask for counting multiplicity. Fill flasks with 4 *ml* medium and place in incubator for  $CO_2$  and temperature equilibrium.
2. Harvest cells from flask by removing medium, flushing with 1.5 *ml* trypsin (or 3 *ml* PBS, adding 3 *ml* trypsin and placing flask in an incubator for 8 – 10 minutes. While waiting fill a tube with 3 *ml*.
3. After waiting suspend the cells until you get a single cell suspension and transfer trypsinized cells to the tube with medium.
4. Centrifuge for 4 minutes at 200 *x g*, aspirate supernatant. Resuspend in 5 *ml* medium
5. Find cell concentration using cell counter, transfer 13  $\mu l$  from cell suspension to cell counting fluidic chamber. Find the concentration (*cells/ml*)
6. Make dilutions based on the number of cells that are to be seeded for each flask, i.e. 200 cells for control, 1 *Gy* and 2 *Gy* samples, 500 cells for 5 *Gy*, 1500 cells for 7.5 *Gy* and 10 000 cells for 10 *Gy* and multiplicity flask.
7. Add 1 *ml* of corresponding cell dilution to each flask and incubate for 5 – 6 hours.
8. Prepare X-ray machine 20 minutes prior to irradiation. Fully seal cell flasks and irradiate cells with designated doses, keep waiting samples on LAF-bench in warm room or incubator during irradiation.
9. Fixate multiplicity flask during or after irradiation. This is done by removing medium, flush flask with 3 *ml* PBS., add 3 *ml* highly purified (around 95%) alcohol to cell flask and leave it for roughly 3 minutes, then remove the ethanol. Add 3 *ml* methylene blue and let it stain the cells for 5 minutes. Pour methylene blue back into container for reuse after staining. Wash the flasks with lukewarm water.

#### Day 3-5

10. Check the cells with a microscope after at least three days. If the cell colonies are at a good size for counting, fixate the cells (explained in point 9).
11. When the flasks have dried count the number of colonies and the multiplicity.